博　士　論　文

First-principles theoretical study of defect induced phenomena in perovskite-type dielectric oxides

(ペロブスカイト型誘電体酸化物中における
欠陥誘起現象に関する第一原理からの理論的研究)

Yoshiki Iwazaki

岩﨑　誉志紀

DISSERTATION

First-principles theoretical study of defect induced phenomena in perovskite-type dielectric oxides

Yoshiki Iwazaki

July 2014

Abstract

The perovskite-type compounds have a wide variety of physical properties that make this material favorable for various electronic-device applications. Defects and impurities govern many of these important physical properties; therefore, the knowledge of the defects is indispensable for the further understanding and development of this material group. Theoretical approaches are particularly important for the subject, because experimental approaches are compelled to observe very limited aspects of the defects and need assistance to understand the nature of the defects in solids. Calculation based on density functional theory (DFT) is one of suitable approaches for the topic. However, more accurate treatment of exchange-correlation (XC) energy functional beyond conventional local density approximation (LDA) is required for the accurate evaluation of defects in solids. In this thesis, three different beyond LDA approaches are introduced: self-interaction correction (SIC), DFT+U, and Hartree Fock (HF)-DFT hybrid functional (PBE0 and HSE), and their characteristics are discussed. We applied these improved XC functionals to the electronic structure calculation of oxygen vacancy (V_{O}) in $SrTiO_3$ and evaluated the efficiency of the XC functionals. Our conclusion is that the hybrid functional is suitable for the calculation of defects in perovskite-type oxides, and hybrid HSE functional is used in the following study. One of remarkable findings in this thesis work is the stability of hydride (H^-) at oxygen site in perovskite-type oxides. Even though the hydride in $A\mathrm{TiO}_3$ is contrary to the common brief that the hydrogen is proton (H^+) in this material group, our results clearly indicate that the H^- at V_{O}^{2+} site is a major defect species in $A\mathrm{TiO}_3$ annealed under hydrogen gas. The stable replacement of O^{2-} with H^- indicates that the experimentally observed 1+ stability of the oxygen vacancy (V_{O}^{+}) is not true but it should be explained by the formation of H_{O}^{+} defect species. We further found that up to two H^- anions have a possibility to occupy the V_{O}^{2+} site. The formation of $(2\mathrm{H})_{\mathrm{O}}$ defect complex leads to complete compensation of the carrier electrons, which explains the previous H_2 annealing experiments for $SrTiO_{3-\delta}$ single crystal. The last topic is the effect of defects on the ferroelectric property of $BaTiO_3$. Ferroelectricity is a representative physical property inhered

in several perovskite-type oxides and is known to easily disappear via various factors. We found that free-carrier electron intrinsically eliminates the ferroelectric displacement in $BaTiO_3$, and the disappearance of the ferroelectric phase is further accelerated by the lattice deformation inevitably induced by the donor-type defects. The series of theoretical calculations clarify the roles of carrier electrons and donor-type defects on the ferroelectric property in perovskite-type oxides.

Acknowledgements

I would like to express my deepest gratitude to Prof. Shinji Tsuneyuki, for his insightful suggestions and continuous support for this work. Without his helpful discussions, this work would not have been possible. I am deeply grateful to Dr. Kazuto Akagi for his helpful guidances and discussions for the theoretical calculation of solid state materials at the initial stage of my work. I also wish to express my gratitude to Dr. Yoshihide Yoshimoto for his constructive discussions and useful comments for the implementation of a new theoretical frame work into TAPP (Tokyo ab initio programming package). I also wish to thank Dr. Yoshihiro Gohda for his useful discussions and excellent collaborations on this work. I am pleased to acknowledge Dr. Keitaro Sodeyama, Dr. Taichi Kosugi and all the members of Tsuneyuki research group during my stay as a researcher. I would like to thank all persons who made my work possible at Department of Physics, Graduate School of Science, The University of Tokyo.

I am exceedingly grateful to the members in Taiyo Yuden Co., Ltd. This work was initially started under Dr. Hirokazu Chazono, and I would like to express my thank to his direction of this work. I also wish to thank Dr. Hiroshi Kishi, Dr. Youichi Mizuno, Dr. Kenji Kawano and Dr. Toshimasa Suzuki for their useful discussions and continuous encouragements.

I also wish to thank to my parents, elder sister, brother-in-law and parents-in-law for their continuous warm encouragements. Finally, I am truly grateful to my family, my wife and two children for their continuous support and patience.

Contents

Chapter 1

Introduction

1.1 Defect and impurity in solids

Improvement of physical and chemical property of material is strongly desired in its application to various electronic devices, because the advance of the material property is the most essential and powerful way for the improvement of the electronic-device performances. Invention of a new material often drastically changes the size, functionality and concept of old devices. Every solid has defects, and the material property greatly depends on the nature of the defect species and its concentration, which often determine the performance of material. Recent technological advance makes it possible to control the defects in material, which gives birth to a new technological area of "defect engineering". Precise control of the defect species often improves the material property to the satisfactory level. Furthermore, completely new and unexpected behaviors are expected in the carefully prepared defect engineering process. Therefore, more extensive study of the defects in condensed matter, such as natural vacancy and doped impurity, is of great importance not only for the material science but also for the industrial aspects.

In contrast to its importance, the atomistic level mechanism of the defect and impurity is not always clear due to technical difficulties in experimental approaches. Even though the electronic structure of a defect can be measured by electron spin resonance (ESR) or electron energy loss spectroscopy (EELS), their interpretations are not always clear, and sometimes very difficult due to the complexity of these experimental results. Furthermore, direct observation of the atomic configuration around the isolated point defect is impossible with transmission electron microscopy (TEM) or X-ray diffraction (XRD) because the point defect does not have any periodicity in a periodically arranged host crystal structure. These problems are difficult

to be solved only from experimental approaches, and theoretical study as a complemental way to clarify the experimental results is desired to fully understand the nature of the defect in solids.

First-principles calculation, which is solely based on the Schrödinger equation of quantum mechanics, has attracted much attention to study the electronic structure of defects in solid materials. Based on the Kohn-Sham equations within the framework of density functional theory (DFT), one can easily know the stability and valence state of a defect species. Furthermore, the atomic configuration around the defect species is obtained by moving atoms according to the force acting on each atom, which is very useful information to compensate the insufficiency of the experimental results. The success of the first-principles calculation for the interpretation of experimental results as well as the prediction of material performance has been widely recognized at the present time.

In this thesis, we will show theoretical calculations of defects and impurities in perovskite-type $A\mathrm{TiO_3}$ (A =Sr, Ba) oxides including the evaluation of the efficiency of currently available theoretical frameworks based on DFT. The perovskite-type compounds have a wide variety of physical properties that makes the material group favorable for various electronic-device applications. The defects and impurities govern many of these important physical properties; therefore, the knowledge of the defects is indispensable for the further understanding and developments of this material group. This introduction will provide a brief overview of basic properties of the perovskite-type oxides and the effects of defects and impurities on the material properties, which will be discussed in detail in the following chapters. Based on the summary of the problems in previous researches, the motivation and outline of the thesis work are explained.

1.2 Brief review of perovskite-type oxide

$A\mathrm{TiO_3}$ (A = Sr, Ba) that is strontium titanate ($\mathrm{SrTiO_3}$) and barium titanate ($\mathrm{BaTiO_3}$) studied in this thesis are most extensively studied and widely utilized materials among various perovskite-type oxides [1]. The basic properties including their crystal structures, phase diagrams and electronic structures are explained in this section.

1.2.1 Perovskite-type titanate

The name of "perovskite" is from the crystal structure of calcium titanate ($\mathrm{CaTiO_3}$) shown in Fig. 1.1, which was named after the Russian mineralogist

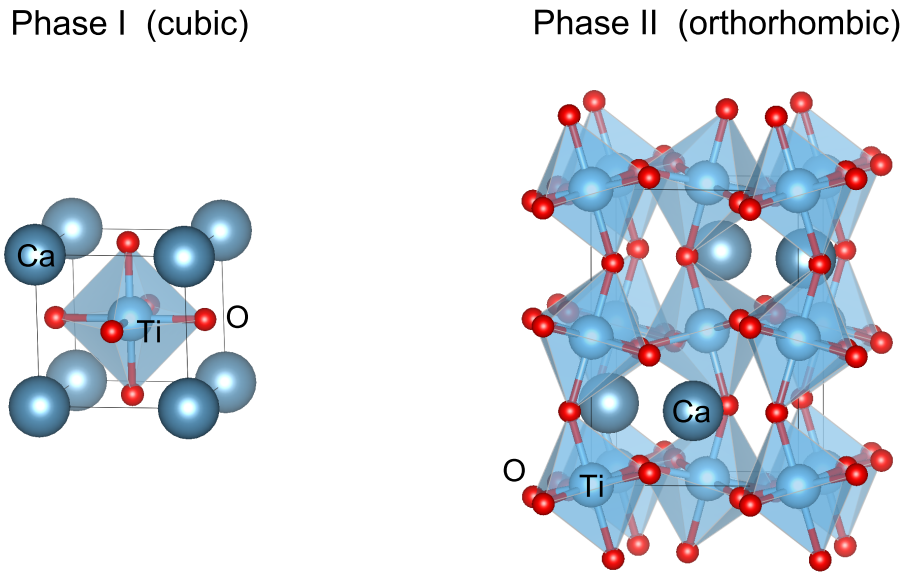

Figure 1.1: Crystal structure of $CaTiO_3$. Phase I has cubic ($Pm3m$) and phase II has orthorhombic ($Pbmm$) symmetry. Phase transition temperature T_C is about 1,260 °C.

L. A. Perovski. The name is currently used to describe a group of crystal with the similar crystal structure of $CaTiO_3$ represented by a general formula of ABO_3. The perovskite structure has long attracted much attention of geologists, because natural perovskite-type oxides, such as $MgSiO_3$ are proposed to be the most abundant mineral in Earth's mantle. The dense packing of the structure makes the perovskite ideal for the high-pressure environment. The perovskite compound has been a subject of interest for numerous researchers including solid state physics, earth science and chemistry, because of their composition and structural variety with totally different physical properties. The rich physical properties, such as ferroelectricity, piezoelectricity, pyroelectricity, optical property, as well as their applications are summarized in Table 1.1.

The basic chemical formula of perovskite structure is expressed as ABX_3, where A and B are metal cations. In many cases, X is an oxide ion, but it can also be fluorine, chlorine, nitrogen, etc. The valence of the A-site cation ranges from +1 to +3, and the B-site cation can take the valence value from +3 to +5. Typical examples of A-site atoms are alkali (Li, Na, K), alkaline earth (Ca, Sr, Ba, ...) or rare earth (La, Gd, Pr, Sm, ...), and B-site atoms are $3d$ transition metals (Mn, Fe, Co, Ti, ...). Depending on the type of elements at A and B site, the perovskite oxide changes its character from insulating to

Table 1.1: Properties and applications of perovskite-type oxides.

Properties	Compounds	Application	Refs.
Ferroelectricity, Piezoelectricity, Pyroelectrcity.	$Pb(Zr,Ti)O_3$, $Pb(Mg, Nb)O_3$, $LiNbO_3$, $LiTaO_3$.	Nonvolatile memory, Ultrasonic sensor, Speaker, IR Sensor, RF filter (SAW).	[2–5]
Dielectric property.	$(Ba,Sr)TiO_3$, $BaTiO_3$.	Multilayer ceramic cap. (MLCC), Thin film cap.	[6, 7]
Optical property.	$LiNbO_3$, $KNbO_3$, $NaNbO_3$.	E.-O. modulator, SHG, Optical switch.	[8–10]
Ionic conductivity, (proton, mixed ion)	$BaCeO_3$, $SrCeO_3$, $BaZrO_3$, $SrZrO_3$, [1]$(La,A)(Co,B)O_{3-\delta}$.	Electrode of SOFC, Hydrogen sensor.	[11–18]
Magnetic property.	$LaMnO_3$, $GdFeO_3$.	Magnetoresistance, Magnetic bubble memory.	[19, 20]
Super conductivity.	$SrTiO_3$, $Ba(Pb,Bi)O_3$, [2]$(La,Sr)_2CuO_4$, [3]$YBa_2Cu_3O_{7-x}$	Superconductor.	[21–26]
Catalytic property.	$LaFeO_3$, $La(Ce,Co)O_3$.	Catalyst.	[27, 28]

[1] A = Sr, Ba; B = Fe, Cr, Mn, Ga

[2] Layered perovskite structure

[3] Oxygen-deficient multi-layered perovskite structure

metallic state. For insulating perovskite-type oxides, charge neutrality must be always preserved, which indicate that the sum of the valence for the A- and B-site cations must be equal to the sum of the three oxide ions ($O^{2-} \times 3$). This is a robust rule that can be applied to any combination of A- and B-site atoms in perovskite-type insulators, such as $A^{2+}B^{4+}O_3^{2-}$ ($SrTiO_3$, $BaTiO_3$, $Pb(Zr, Ti)O_3$), $A^{1+}B^{5+}O_3^{2-}$ ($KNbO_3$, $NaNbO_3$) and $A^{3+}B^{3+}O_3^{2-}$ ($LaMnO_3$, $LaNiO_3$) .

Strontium titanate ($SrTiO_3$)

Strontium titanate ($SrTiO_3$) is one of the most widely investigated perovskite-type oxides that has attracted much attention because of its considerable potential for various technological applications. The simple structure of $SrTiO_3$ is regarded as a prototype for many perovskites, in which the detailed investigation of intrinsic/extrinsic defects and dopants can lay the basis of theoretical approach that can be applied to structurally and chemically more

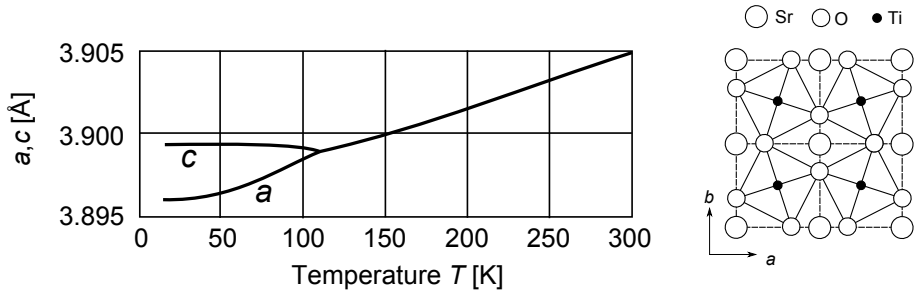

Figure 1.2: The change of a- and c-axis length at around the phase transition temperature of $SrTiO_3$ [29]. The right-hand side figure is the rotational AFD lattice distortion of $SrTiO_3$.

complex perovskite oxides. In addition to being a prototypical model of the perovskite-type structure, $SrTiO_3$ shows a wide variety of physical and chemical properties, such as insulator-to-metal transition [30–33], superconductivity [21, 26, 31], ionic conductivity [34] and visible-light emission [35]. At room temperature, $SrTiO_3$ has an ideal cubic $Pm3m$ perovskite structure with a Ti atom at the center, Sr atoms at the corner and three O atoms at the face centers. At lower temperature ($\sim$ below 105 K), $SrTiO_3$ undergoes a structural phase transition to a tetragonal phase [29, 36–38] without the emergence of ferroelectric phase as shown in Fig. 1.2. This is the so-called antiferrodistortive (AFD) phase transition that is caused by a rotation of the TiO_6 octahedra along one of the Cartesian axes (Fig. 1.2). The dielectric constant saturates at a large value of 20,000 as temperature approaches zero [39]. The absence of ferroelectric transition is suggested to be caused by quantum fluctuation, which give rise to a quantum paraelectric phase at very low temperature [30, 40].

Barium titanate ($BaTiO_3$)

Perovskite-type $BaTiO_3$ is also a typical ferroelectric material that has been extensively studied since its discovery more than 60 years ago. The discovery of ferroelectricity in a simple perovskite structure has given birth to a large number of ferroelectric ABO_3-type perovskite oxides that are currently of great technological interest due to their various excellent properties, as shown in Table 1.1. The large dielectric constant of $BaTiO_3$ at around room temperature is of great importance for the capacitor application such as a multi-layer ceramic capacitor (MLCC) [6, 41] because the large dielectric constant effectively minimize the size without spoiling the capacitance. The

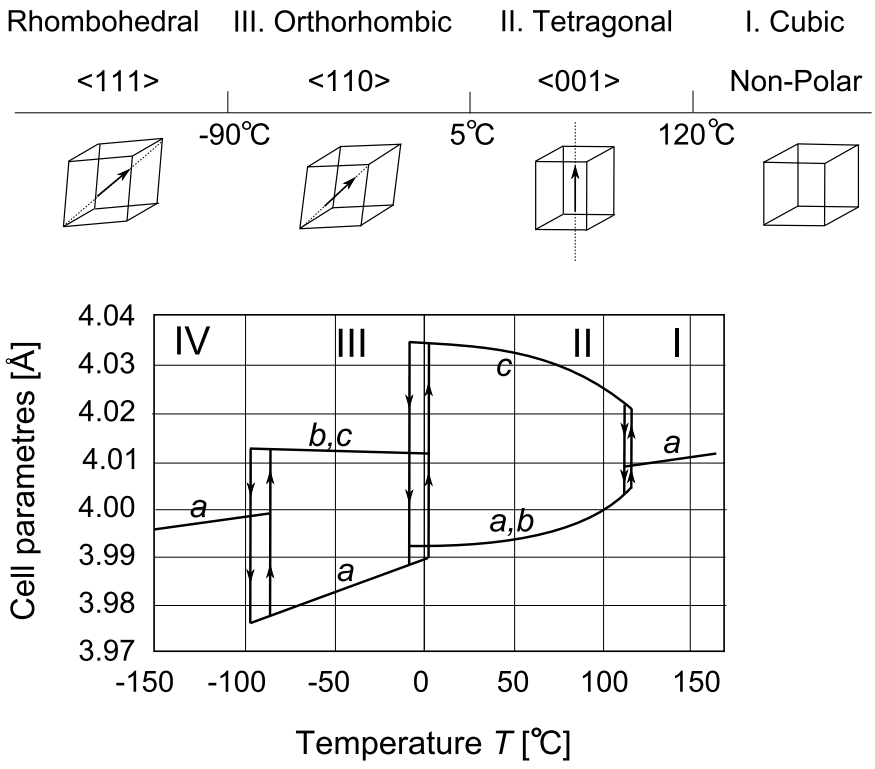

Figure 1.3: Phase transition behavior of $BaTiO_3$. The polar axis of the three ferroelectric phases, and the change of the lattice constant of all four phases are shown in the figure. Above the Curie temperature (T_C = 120°C), the $BaTiO_3$ becomes non-polar cubic phase.

small and high-energy density capacitors greatly contribute to the miniaturization of electronic devices, such as mobile phone, PC, automobile electronic system, etc.

The definition of ferroelectricity is the existence of spontaneous polarization that can be switched by external electric field. The spontaneous polarization in $BaTiO_3$ is induced by lattice instability due to the mismatch of ionic size composing $BaTiO_3$. The size of B-site Ti ion is too small to be stable in the center of TiO_6 octahedra, which makes Ti ion moving off-center in the direction of any of six oxygen ions to achieve a minimum energy configuration. The lattice instability of $BaTiO_3$ induces a series of phase transitions from paraelectric cubic (C) to ferroelectric tetragonal (T), orthorhombic (O), and rhombohedral (R) phases at 396, 278, and 183 K, respectively. The polar axes in T, O and R phases are [001], [011] and [111], respectively. The series of phase transition is summarized in Fig. 1.3. The dielectric constant of

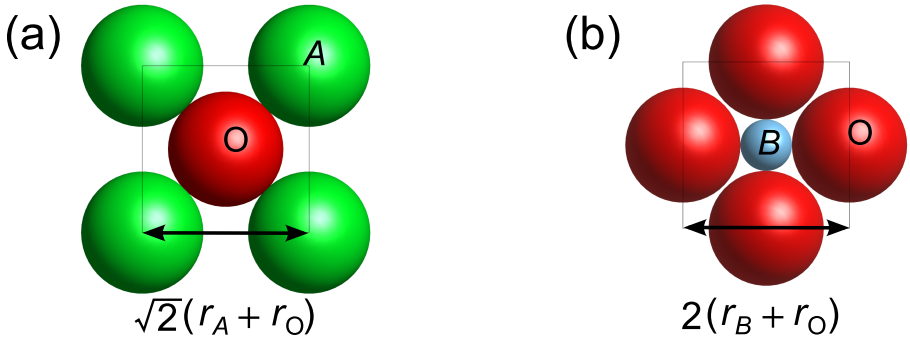

Figure 1.4: Cross sectional images of ABO_3 on (a) AO and (b) BO_2 planes in a ABO_3 perovskite structure. The figure assumes the ionic radii of $SrTiO_3$: Sr^{2+} for A- and Ti^{4+} for B-site ions.

$BaTiO_3$ is very large, especially at each phase transition temperature, where the value reaches more than $10,000$.

1.2.2 Crystallographic character of perovskite crystal

The perovskite structure ABO_3 is composed of a framework of corner-sharing BO_6 octahedra with the A cation located on an interstitial site surrounded by the eight octahedra. From the geometrical relation, the $r_A + r_O$ should be equal to $\sqrt{2}(r_B + r_O)$ in an ideal cubic perovskite structure as shown in Fig. 1.4, where r_A, r_B and r_O are the ionic radii of the A, B and oxygen ions, respectively. Based on the above consideration, V. M. Goldschmidt [42] introduced a relationship between ionic radii and lattice instability of perovskite structure, which is called tolerance factor t defined as follows:

$$t = \frac{r_A + r_O}{\sqrt{2}(r_B + r_O)}. \tag{1.1}$$

The instability of the perovskite lattice can be conveniently classified by the value of the tolerance factor [43–47]. In fact, the tolerance factor t is quite effective in predicting the global trend of lattice instabilities in perovskites, such as ferroelectric distortions [43,46] and tilts and rotations of BO_6 octahedra [43,44] including antiferrodistortive (AFD) instabilities of $SrTiO_3$ [38,48]. Experimentally, many perovskites are confirmed to take the tolerance factor values in a range $0.81 < t < 1.11$. The ideal perovskite structure has $t = 1.00$, where the ionic radii of the constituent atoms completely match. The tolerance factor of $SrTiO_3$ is $t_{SrTiO_3} = 1.009$, which indicates the stable ion packing of the $SrTiO_3$. The value $t < 1$ indicates that the A-site cation is

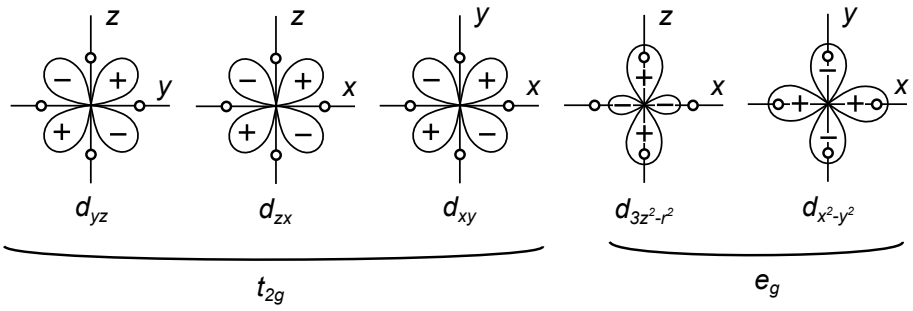

Figure 1.5: The shapes of d-orbitals of isolated transition metal, which can be classified into e_g and t_{2g} symmetry. White circles denote point charges at the oxygen anion sites.

too small (or B-site cation is too large) for the crystal structure; A–O bonds are under tension and B–O bonds are under compression, which makes the corner shared BO_6 octahedra tilt or rotate so as to accommodate the large BO_6 octahedra into the cubic lattices defined by the small A cations. The crystal structure of $CaTiO_3$ ($t = 0.973$) shown in Fig. 1.1 is a typical example for the tilting of TiO_6 octahedra. Of particular interest is the lattice instability of $BaTiO_3$ whose t is 1.062. In this case ($t > 1$), the B-site cation is too small compared to the allowed space defined by the A-O distance, which leads to off center shift of the Ti atom. The shift of the Ti atom along a polar axis is the direct cause of the spontaneous polarization in $BaTiO_3$.

The tolerance factor is very intuitive and can be widely applied to a series of lattice instabilities in perovskite-type oxides. However, some systems whose t is within the permissible range are not stable [47]. Moreover, the tolerance factor cannot explain the strong ferroelectric displacement of $PbTiO_3$ ($t = 1.019$) compared to $BaTiO_3$ ($t = 1.062$), and another explanation based on chemical bonding is required for the phenomenon; contrary to the fully ionic nature of Ba^{2+} in $BaTiO_3$ whose phase transition temperature $T_{C(BaTiO_3)} = 393$ K, Pb-6s and O-2p hybridization greatly raises the phase transition temperature of $PbTiO_3$ ($T_{C(PbTiO_3)} = 763$ K) [49]. Even though the tolerance factor can describe overall structural properties of ABO_3 perovskites, it is an insufficient classification for all the lattice instabilities in perovskite materials.

1.2.3 Electronic structure

The electronic structure of ABO_3 perovskite is basically composed of O-2p valence band and B-d conduction band. The d-band composing conduc-

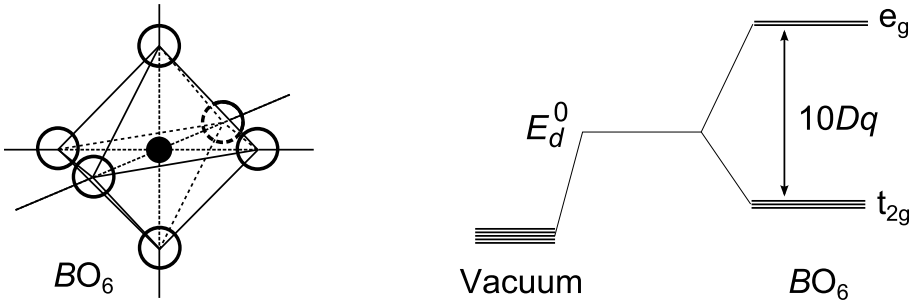

Figure 1.6: Ligand-anion configuration of a perovskite structure with cubic-symmetry, and the splitting of energy levels due to the ligand field. The five-fold degenerated d orbitals split into e_g and t_{2g} levels. E_d^0 is their average.

tion band minimum (CBM) of perovskites is of great interest, because the electronic structure of CBM determines most of the physical and chemical activities, such as electron conduction, catalytic and optical behaviors. The band structure of ABO_3 perovskite oxides can be qualitatively explained based on the symmetry and splitting of the d orbitals due to the crystal field, as explained in the following sections.

Crystal field theory

The d orbitals of isolated transition-metal atom have five-fold degeneracy with different magnetic quantum number. In perovskite ABO_3 crystal structure, the degeneracy of the d orbitals of transition-metal B cation is solved due to the Coulomb potential from surrounding O^{2-} ligand ions. The situation can be analytically explained by crystal field theory, where the effects of the ligand oxygen ions are simply replaced by point charges surrounding the B cation as shown in Fig. 1.5. The figure also includes the point charges which replaces oxygen ligand anions at the same distance in the $\pm x, \pm y, \pm z$ directions [50]. In perovskite structure, the B-site cation is coordinated by six oxygens, and the simplest example is the cubic-symmetry crystal field as shown in Fig. 1.6. According to the symmetry, the five d-orbitals are categorized into two groups: $d\varepsilon$: d_{xy}, d_{yz}, d_{zx} and $d\gamma$: $d_{x^2-y^2}$, $d_{3z^2-r^2}$, where $d\varepsilon$ and $d\gamma$ orbital groups have t_{2g} and e_g symmetry, respectively [50]. The eigenfunction of these d orbitals are summarized as follows:

$$d\varepsilon\ (\mathrm{t}_{2g}) \begin{cases} \phi_{xy} = \sqrt{\dfrac{15}{4\pi}} \dfrac{R_{32}(r)}{r^2} xy \\ \phi_{yz} = \sqrt{\dfrac{15}{4\pi}} \dfrac{R_{32}(r)}{r^2} yz \\ \phi_{zx} = \sqrt{\dfrac{15}{4\pi}} \dfrac{R_{32}(r)}{r^2} zx \end{cases} \tag{1.2}$$

$$d\gamma\ (\mathrm{e}_g) \begin{cases} \phi_{x^2-y^2} = \sqrt{\dfrac{15}{16\pi}} \dfrac{R_{32}(r)}{r^2} (x^2 - y^2) \\ \phi_{3z^2-r^2} = \sqrt{\dfrac{15}{16\pi}} \dfrac{R_{32}(r)}{r^2} (3z^2 - r^2), \end{cases} \tag{1.3}$$

where $r = \sqrt{x^2 + y^2 + z^2}$, and $R_{32}(r)$ is a radial distribution function of $3d$ orbital denoted by:

$$\begin{aligned} R_{32}(r) &= \frac{4}{81\sqrt{30}} \left(\frac{Z}{a_0}\right)^{\frac{3}{2}} \rho^2 e^{-\frac{\rho}{3}}, \\ \rho &= \frac{Z}{a_0} r, \end{aligned} \tag{1.4}$$

where a_0 is Bohr radius and Z is the atomic number.

The orbital energy of $d\varepsilon$ orbital is lower than that of dγ orbital, because they extend between the point charges so as to avoid the direct Coulomb force from the point charges as shown in Fig. 1.5. On the other hand, the dγ orbitals that are directly subject to the Coulomb force from the point charges have higher energies. The energy difference between e_g and t_{2g} can be analytically calculated [50], and the value between these two energies is expressed as:

$$E_{e_g} - E_{t_{2g}} = 10Dq = \frac{1.67Ze^2}{4\pi\varepsilon_0} \frac{1}{a^5} \int_0^\infty r^4 R_{32}^2(r) r^2 dr, \tag{1.5}$$

which are illustrated in Fig. 1.6.

Each ligand oxygen forming an $B\mathrm{O}_6$ octahedra has three p orbitals, which can be classified into similar e_g and t_{2g} symmetry as shown in Fig. 1.7. The p-d hybridization occurs only between p and d orbitals with the same symmetry. Figure 1.7 also shows energy levels expected in $B\mathrm{O}_6$ octahedra.

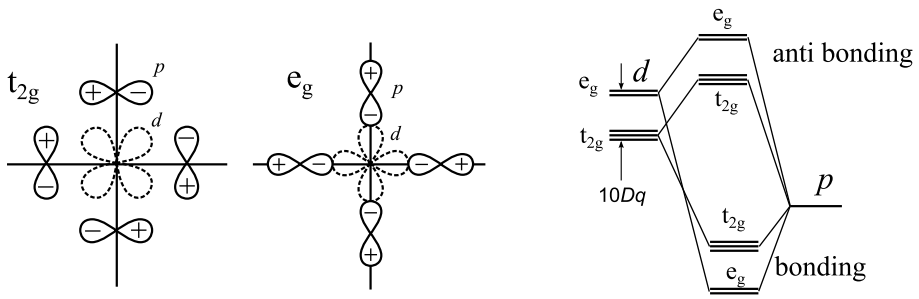

Figure 1.7: Symmetry of p orbitals forming BO_6 octahedra. The left-hand side figures indicate t_{2g} and e_g symmetry of these p orbitals. The bonding and anti-bonding states occur between p and d orbitals with the same symmetry as shown by the right-hand side figure.

The bonding and anti-bonding states are mainly composed of p and d orbitals, respectively. This is because that the O-2p energy level is usually lower than that of transition metal d level. Therefore, the conduction band minimum (CBM) is mainly characterized by the transition metal $d_{t_{2g}}$ with a small hybridization with O-2$p_{t_{2g}}$.

Band structure

Band structure of perovskite-type oxide was initially discussed by J. B. Goodenough [51] for ReO_3 that is a red color solid with a metallic conductivity. The crystal structure of ReO_3 shown in 1.8(a) is similar to the cubic perovskite except that A cation is missing. Each rhenium atom is surrounded by 6 oxygen anions that form a ReO_6 octahedra. The band structure of ReO_3 can be regarded as a prototypical electronic structure that can be a basis for more complex perovskite compounds. ReO_3 is a highly conducting d band electron conductor whose resistivity is very low comparable to metal silver [50]. The proposed energy level diagram of ReO_3 is shown in Fig 1.8(b). ReO_3 has $5d^1$ electronic configuration and there is one conducting electron on the d band of Re. The t_{2g} orbitals of Re-5d and O-2p hybridize with each other so as to form π bonding states, where the anti-bonding states form CBM (denoted by π^*) and the bonding states form VBM (π) in the energy diagram shown in Fig. 1.8 (b). The e_g states of d and p orbitals form σ-bonding states and these bonding and anti-bonding states are outside of the π bonding states. An APW calculation performed later by Mattheiss [52] slightly alters the schematic picture of the energy diagram, since the splitting of the π and σ band is not so clear as shown in Fig. 1.8(c). These slight

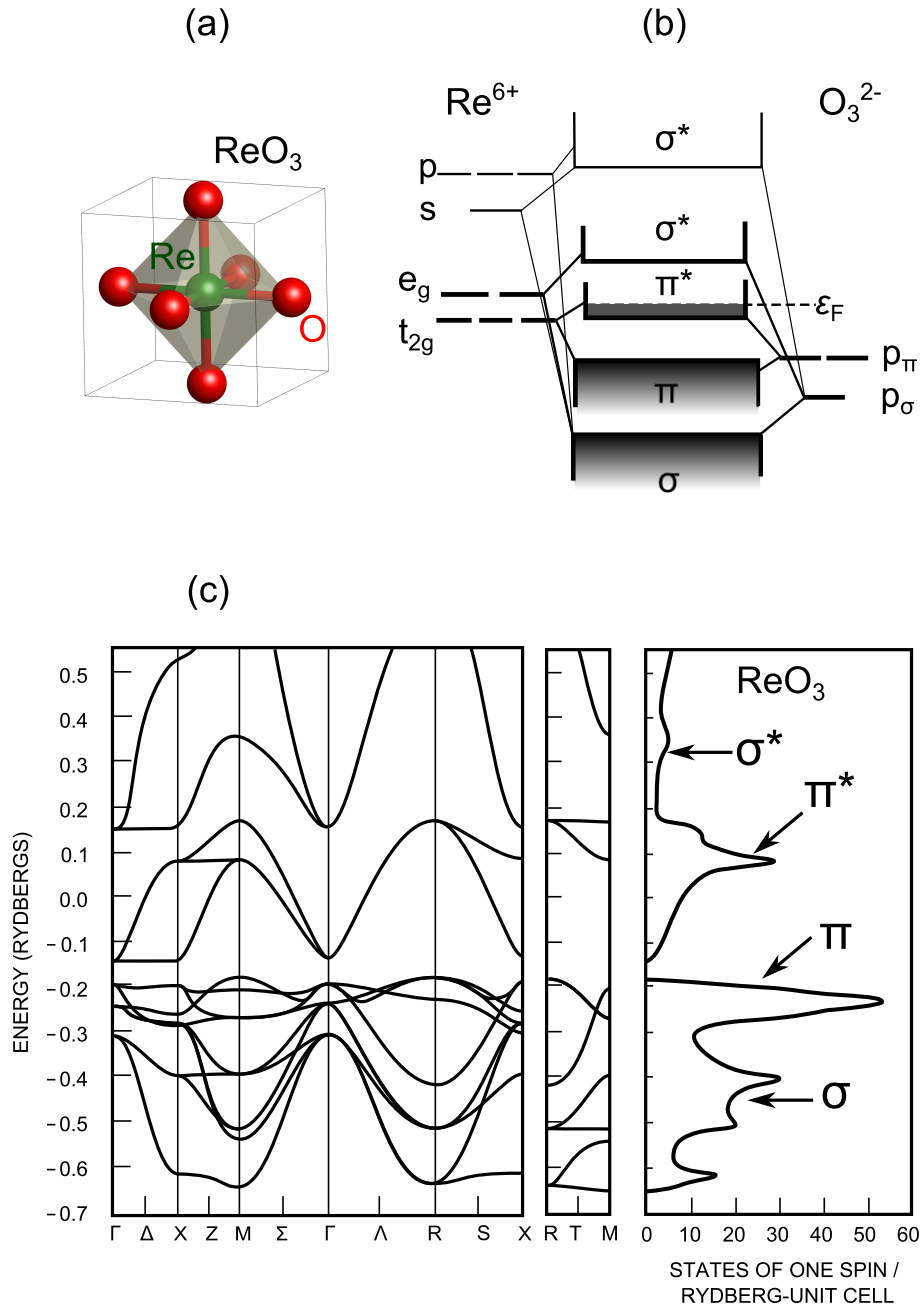

Figure 1.8: (a) Crystal structure of ReO_3 and (b) energy level diagram proposed by J. B. Goodenough [51]. (c) Band structure of ReO_3 calculated by Mattheiss [52] with APW method.

modification, however, does not spoil the essence of the *p*-*d* hybridization in the band structure of ReO_3. $ATiO_3$ (A = Sr, Ba) is a band insulator with an empty conduction band composed of d^0 character of Ti^{4+}, which is different from d^1 electronic configuration of ReO_3. Nevertheless, the basic character of the band structure of $ATiO_3$ is very similar to that of ReO_3, and almost the same interpretation is valid in $ATiO_3$.

1.3 Defect and impurity in perovskite oxides

1.3.1 Oxygen vacancy

The defect and impurity in transition-metal oxides have been an actively studied issue, because of the strong impact on the material properties. The typical intrinsic defects in $ATiO_3$ are cation (both A-site and Ti atom) and oxygen anion vacancy, and many physical properties, especially electron conductivity greatly depends on the amount of anion and cation vacancies (non-stoichiometry) [33, 53, 54]. Among these defect species, oxygen vacancy (V_O) whose general formula is $ATiO_{3-\delta}$ is of fundamental importance, because it is easily generated in the fabrication process of the perovskite oxides in various ways, such as crystal growth, ceramic firing and annealing treatment. Furthermore, the migration of V_O under electric filed has a great impact on the fatigue or degradation of electronic devices with perovskite oxide, such as ferroelectric memory with $Pb(Ti,Zr)O_3$ [55], thin-film capacitor (TFC) with (Ba, Sr)TiO_3 [53] and multi-layer ceramic capacitor (MLCC) based on $BaTiO_3$ [6, 56, 57]. It is not surprising that the nature of the oxygen vacancy in perovskites has been a subject of various theoretical and experimental studies [31–33, 53, 55–64].

The generation of defects can be written with Kröger-Vink notation that is a widely used description for defects in semiconductor and insulator. The V_O in $SrTiO_{3-\delta}$ is often regarded as doubly charged V_O^{2+}, which leads to the following Kröger-Vink formula:

$$O_O^{\times} \leftrightarrows \frac{1}{2}O_{2(gas)} + V_O^{\bullet\bullet} + 2e'. \tag{1.6}$$

In the Kröger-Vink formula, each defect state is written in the form M_S^C, where M is the atom species (vacancy is denoted by "V") and S is the position of the defect (oxygen site is denoted by "O"). C is the charge state, where "$\times$","$\bullet$" and "$\prime$" are neutral, positive and negative charges, respectively. In Eq. (1.6), $O_O^{\times}$ is an oxygen anion on the oxygen site and $V_O^{\bullet\bullet}$ is a 2+ charged oxygen vacancy on the oxygen site. The electron doping with the oxygen

vacancy induces an insulator-to-metal transition in $A\mathrm{TiO}_3$, and the behavior has been widely studied in an attempt to understand the carrier doping mechanism and the role of the oxygen vacancy itself. Stoichiometric SrTiO_3 and BaTiO_3 are band insulators with band gap values of 3.21 and 3.11 eV, respectively [1, 65]. By the doping of the oxygen vacancy, the $\mathrm{SrTiO}_{3-\delta}$ becomes either semiconductor or metallic conductor depending on the concentration of the oxygen deficiency [30], and it even becomes a superconductor at very low temperature [21]. The electron doping can be also achieved by the substitutional doping with different valence cations for both A- and Ti-site of $A\mathrm{TiO}_3$ (A =Sr, Ba), such as La^{3+} at Sr^{2+} and Nb^{5+} at Ti^{4+} [54]. The characteristic point of the electron doping in SrTiO_3 is their extremely small critical density (around 10^{18} cm^{-3}) for the insulator-metal (IM) transition, which is several orders of magnitude smaller than the typical values observed for other electron-doped transition-metal oxides [33]. Similarly, the superconductivity occurs at a relatively low carrier-electron concentration (around 10^{19} cm^{-3}) [33]. In contrast to SrTiO_3, electron doped BaTiO_3 undergoes IM transition at much higher electron-doping level around 10^{20} cm^{-3} [54]. The reason for such a high doping level in BaTiO_3 is attributed either to disorder-induced Anderson-type localization or phonon-induced localization (small-polaron model) of the carrier electron [54].

Despite the fact that a fair amount of fundamental research has been carried out for the oxygen deficiency in $A\mathrm{TiO}_{3-\delta}$, the nature of V_O has not been well clarified yet. Most puzzling experimental result is the relation between the oxygen deficiency and carrier-electron density. For example, $\mathrm{SrTiO}_{3-\delta}$ is expected to have 2δ number of electrons according to Eq. (1.6). On the other hand, several experimental results suggest that the V_O is singly ionized V_O^+ in $\mathrm{SrTiO}_{3-\delta}$ samples weakly reduced with H_2 and $\mathrm{H}_2\mathrm{O}$ gas [31, 58, 64], which are expressed by the formula:

$$\mathrm{O}_\mathrm{O}^\times \leftrightarrows \frac{1}{2}\mathrm{O}_{2(\mathrm{gas})} + \mathrm{V}_\mathrm{O}^\bullet + e', \tag{1.7}$$

In grossly oxygen deficient samples that are fabricated with Ti-gettering for oxygen or from oxygen deficient starting materials (TiO_{2-x} and SrCO_3) [32, 59], the valence state of V_O is further reduced to $\sim V_\mathrm{O}^{0.5+}$ [32]. In these grossly oxygen deficient samples, the oxygen vacancy is suggested to be no longer an isolated vacancy, and a possibility of some kind of vacancy-clustering formation has been pointed out by the transmission electron microscopy (TEM) and electron conduction measurements [33,60]. The oxygen-vacancy clustering has been theoretically studied by Shanthi *et al.* [61] who calculated various combination of clustering models and clarified that the oxygen-vacancy clustering tends to generate deep in-gap states and all the

carrier electrons from the oxygen vacancies are trapped by these in-gap states. More recent first-principles calculation with on-site Coulomb-potential corrected DFT (LDA+U) clarified that oxygen vacancies tend to order in a linear way [63], and the localized in-gap state traps all of the electrons released from the oxygen vacancies. Thus, the oxygen-vacancy clustering would be the cause of the great reduction of the carrier-electron density in the grossly oxygen deficient $SrTiO_{3-\delta}$. However, the experimentally confirmed +1 valence state of the isolated oxygen vacancy in the slightly reduced $SrTiO_{3-\delta}$ cannot be explained in terms of the oxygen-vacancy clustering. Therefore, the electronic structure of the isolated oxygen vacancy in $SrTiO_{3-\delta}$ has been a subject of extensive theoretical studies [30, 61, 62, 66, 67]. However, the electronic structure calculation of the realistically isolated oxygen vacancy is a very hard task because of several requirements which are difficult to be sufficiently satisfied, such as an appropriate approximation for exchange correlation energy and the adoption of sufficiently large atomistic models to represent the proper diluted defect concentrations. Due to these problems, there have been disputes for the electronic structure of an isolated oxygen vacancy in $SrTiO_3$. This is a problem not only for $SrTiO_3$, but also for other transition-metal oxides, such as $BaTiO_3$ [64], TiO_2 [68] and ZnO [69, 70]. Despite these difficulties, the electronic structure calculation is considered to be a powerful tool for the analysis of the complicated experimental results, and the theoretical assistances are greatly desired to fully understand the nature of the defects in transition-metal oxides.

1.3.2 Hydrogen impurity

Hydrogen is a ubiquitous element and easily contained in materials as an impurity. In particular, hydrogen annealing, which is the most frequently used technique to reduce transition-metal oxides, makes the analysis of the carrier-electron density very confused, because the roles of the hydrogen in these hydrogen-annealing process are not well clarified yet. There are two possible scenarios for the hydrogen reduction of the perovskite-type $ATiO_3$ oxides. Many previous experiments assume the removal of oxygen by hydrogen as a form of H_2O, which results in a generation of the oxygen vacancy and carrier electrons:

$$O_O^{\times} + H_{2(gas)} \leftrightarrows \frac{1}{2}H_2O_{(gas)} + V_O^{\bullet\bullet} + 2e'. \tag{1.8}$$

Another possibility is the incorporation of the hydrogen at an interstitial site of the perovskite lattice. The interstitial hydrogen (H_i) has been suggested

to act as a shallow donor in $A\mathrm{TiO_3}$.

$$\frac{1}{2}\mathrm{H_{2(gas)}} \leftrightarrows \mathrm{H_i^\bullet} + e'. \tag{1.9}$$

The existence of $\mathrm{H_i}$ in $A\mathrm{TiO_3}$ can be confirmed with infrared (IR) spectroscopy by detecting absorption peaks of the O-H vibrational motions around 3,500 $\mathrm{cm^{-1}}$ [71]. Therefore, both oxygen vacancy and hydrogen may potentially contribute to the electrical conductivity in $A\mathrm{TiO_3}$. In the semiconductor device possessing, a large increase of the leakage current is observed for $\mathrm{SrTiO_3}$ films and related materials, such as (Ba,Sr)$\mathrm{TiO_3}$ when annealed with forming gas that contains hydrogen [59]. However, the main cause of the increased carrier-electron density is unclear because of the lack of knowledge for the mutual interaction between V_O and $\mathrm{H_i}$, such as relative stability and possibility of complex defect formation with V_O and $\mathrm{H_i}$. There are similar discussions for the electron conductivity of ZnO, where the oxygen vacancy makes a deep in-gap state and all the carrier electrons from the oxygen vacancy are trapped at the defect level [69]. Hence, the oxygen vacancy cannot be a source of the carrier electron in ZnO, and the most promising candidate for the origin of the carrier electron is the hydrogen related defect species in ZnO [69].

Recent studies also suggest the importance of "hidden" hydrogen in semiconductors and insulators. First-principles calculation indicates that the typical hidden hydrogen is an anionic hydride ($\mathrm{H^-}$) which occupies the anion vacancy in ZnO [70, 72], $\mathrm{SnO_2}$ [73] and II-VI semiconductors [74]. The $\mathrm{H_2}$ molecule at the anion-vacancy site is also a promising candidate for the hidden hydrogen in ZnO [70, 75, 76]. On the other hand, the existence of $\mathrm{H^-}$ is contrary to the common belief that the perovskite-type oxides are good proton ($\mathrm{H^+}$) conductor, and the possibility of $\mathrm{H^-}$ in this material have not been well considered yet. However, these previous studies for wide variety of semiconductors and insulators imply the importance of the hidden hydrogen also in the perovskite-type oxides. In addition, some recent experiments show puzzling results that oxygen-deficient blue-black conducting $\mathrm{SrTiO_{3-\delta}}$ transforms into a transparent insulating state upon annealing under $\mathrm{H_2}$ containing atmosphere [59, 77]. These experimental results cannot be explained by the proton picture of hydrogen at interstitial sites ($\mathrm{H_i^+}$), suggesting that the role of hydrogen in the material group $A\mathrm{TiO_3}$ (A = Sr, Ba) should be reconsidered.

The hydrogen is an ubiquitous element, and is difficult to be completely eliminated from materials. Simultaneously, the detection of the hydrogen is also difficult due to their light mass and the characteristic electronic structure without core-level states. Therefore, theoretical approach with first-

principles calculation is greatly desired for the understanding of the behavior of hydrogen in perovskite-type oxides.

1.3.3 Relation between defect and ferroelectricity

Ferroelectricity that includes spontaneous polarization, piezoelectricity and pyroelectricity is an inherent property in some perovskite-type oxides, such as $BaTiO_3$ and $Pb(Zr_x, Ti_{1-x})O_3$, and the property makes the perovskites particularly useful for various electronic device applications as summarized in Table 1.1. However, the ferroelectricity is easily damaged by so many factors, such as introduction of defects and impurities [78–82], application of pressure or stress [83–85], and surface effects in thin films and fine particles [86–89]. The ferroelectricity of $BaTiO_3$ is also greatly damaged by the increase of the electron conductivity induced by donor-type defects and dopants. One would expect that the ferroelectric phases would naturally disappear in the presence of metallic conductivity due to the screening of the long-range electrostatic interactions that are partially responsible for the emergence of ferroelectricity [49, 90]. However, experiments with reduced $BaTiO_{3-\delta}$ indicate that the presence of the free electron does not immediately suppress the ferroelectric phase, but the ferroelectric deformation sustains even under the metallic conductivity [78, 79]. Under the low-resistivity condition, ferroelectric hysteresis loops cannot be measured due to the large leakage currents. Therefore, the existence of the ferroelectric phase under metallic conductivity in the reduced $BaTiO_{3-\delta}$ are experimentally confirmed by using X-ray diffraction, dc and optical conductivities [78, 79] and typical volumetric shrinkage at ferroelectric phase transition temperatures [58] instead of the direct measurement of the ferroelectric hysteresis loops. The critical carrier-electron concentration for the disappearance of the ferroelectric phases in $BaTiO_{3-\delta}$ is recently confirmed to be $n \approx 1.9 \times 10^{21}$ cm^{-3} [78], which is one order magnitude larger than the critical carrier-electron concentration of insulator-to-metal transition in electron doped $BaTiO_3$ ($\sim 10^{20}$ cm^{-3}) [54]. Although the disappearance of the ferroelectric phase by donor-type dopants has been extensively discussed [54, 58, 78–82], it has not been clear whether the transition from ferroelectric to paraelectric phases is caused by the introduction of free carrier electron or by the lattice deformation due to donor-type defects. These two effects are very difficult to separate experimentally [58, 78] because defects (or dopants) are inevitably introduced in electron doping experiments. It is highly desirable to form a theoretical basis to understand this subject, because the current understandings are based on only some indirect and restricted experiments, and obviously lack basic understandings for the relation between the carrier electron and the ferroelectricity.

1.4 First-principles calculation for defects and impurity

First principles calculation based on density-functional theory (DFT) has become a promising method for the study of electronic structure of defects in semiconductor and insulator. The theoretical study of defects in transition-metal oxides has been one of intensively studied research areas. However, many of these studies are in highly controversial states due to several problems in DFT. The most popular approach for the defect calculation is based on Kohn-Sham equation that is Schrödinger equation for a fictitious system of non-interacting particles with many body effects represented by an exchange-correlation (XC) energy functional. The accuracy of Kohn-Sham equation is governed by the XC functional, and the strictly accurate ground state is obtained if one can know the exact form of the XC energy functional. The most popular XC energy functional is local-density approximation (LDA), where the XC potential depends solely upon the value of the charge density at each position. In spite of its very simple formulation derived from homogeneous electron gas model, LDA has been successfully applied to a wide variety of solids and has been greatly contributed to the advance of the electronic structure calculation of solid state materials.

However, LDA has several serious problems that should be corrected for the calculation of defects in solids. The underestimation of band gap values in semiconductors and insulators is a well-known drawback of LDA, and the inaccuracy of the gap is hardly improved by generalized gradient approximation (GGA) that includes gradient term of density into LDA. The nature of a defect, such as relative position of defect level within the gap and the stability of charged state, greatly depends on the band gap value. Therefore, the band gap error of LDA should be corrected by improved XC functionals so as to obtain satisfactory results. In addition, self-interaction error (SIE) due to the insufficient exchange of LDA should be completely eliminated for a system with a localized electron nature, because LDA becomes completely useless especially for a system with strongly correlated electron. Many defect states in solids have intermediate nature between the localized and delocalized limits of electron systems, which makes the limitation of LDA very unclear. Although it would be very difficult to discuss the validity of the XC functional for these problems, many of previous studies employing LDA or GGA suggest an empty defect state of oxygen vacancy (V_{O}^{2+}) in $SrTiO_3$ [30, 61], whereas improved functionals such as the GGA+U and the Hartree-Fock (HF)-DFT hybrid functional show total (V_{O}^{0}) localization of electrons at the vacancy site [62, 66, 67]. The upward shift of the localized state is a clear sign of the

SIE due to the insufficient exchange. Therefore, there must be not a small error in the picture of oxygen vacancy level of $SrTiO_3$ calculated with LDA. Thus, both band gap and SIE should be appropriately corrected by improved XC functionals over LDA [62, 64].

1.5 Motivation and outline of the thesis

1.5.1 Motivation

As described in previous sections, the improvement of material property of perovskite-type oxides greatly depends on the understanding of the defects and impurities. It is also noted that the improvement of the XC functional is necessary for these studies, because the electron localization around the defect species is difficult to be treated with conventional LDA and GGA. For this reason, we have studied defects and impurities in perovskite-type $ATiO_3$ (A=Sr, Ba) oxides based on the first-principles calculation with improved XC functional in the framework of DFT. The main purpose of our study is the clarification of various experimental results observed in $ATiO_3$ samples reduced with hydrogen gas, where the defect species and its valence states are closely related to the experimental results. Due to the complexity of the defect natures, many of these experimental results have not been clarified yet. In this thesis, we employed several theoretical frameworks of the improved XC functional, and studied their feasibility for the defect calculations in perovskite-type oxides. By using the improved XC functional, we will discuss the oxygen vacancy and hydrogen-related defects in $ATiO_3$, and the effects of these defect species on the physical properties, such as carrier-electron density and ferroelectricity are discussed. The clarification of the diversity of the hydrogen in transition-metal oxides is also an important issue in this thesis.

1.5.2 Outline of the thesis

The thesis is composed of the following chapters. In this Introduction chapter, we have explained the basic properties of the perovskite-type oxides and overview of the effects of defects and impurities on material properties [41,91]. We have also discussed the failure of LDA and necessity of their improvement. In Chapter 2, the basic formalism of DFT including the derivation of Kohn-Sham (KS) equations are explained. As a standard XC functional, concept and actual form of LDA and GGA are explained. We also explain the treatment of the core electron with ultra-soft pseudo potential (USPP)

and projector augmented wave (PAW) method, which are thoroughly used in this thesis. This chapter also includes the theoretical backgrounds of three improved XC functionals. The first one is the self-interaction correction (SIC) that is a direct subtraction of self-interaction (SI) energy from the KS equations. We implemented "pseudo SIC" scheme into *Tokyo ab-initio programming package* (TAPP). The second functional is DFT+U that is a widely adapted method for the correction of LDA and GGA due to their simple and steady formalism. We employed the rotationally invariant formalism of DFT+U and discussed the detail of the formalism and the effect of +U potential. The last one is hybrid functional that is a XC functional composed of the mixture of DFT XC and exact exchange (EXX) of Hartree-Fock method. We will explain PBE0 and HSE hybrid functionals, which is a very simple but has physically clear foundation. The effects of these three improved XC functionals on the band gap values of several transition-metal oxides and semiconductors are explained, and the reasons for the improvements by these functionals are discussed. In Chapter 3, theoretical calculations for oxygen vacancy (V_{O}) in $SrTiO_3$ are performed [91]. The main aim of this chapter is the evaluation of the effectiveness of these improved XC functionals on the defect calculations, as well as the clarification of the nature of isolated V_{O} in $SrTiO_3$. Our results clearly show that the electronic structure of V_{O} in $SrTiO_3$ greatly depends not only on the XC functional, but also on the lattice relaxation around the defect species. By summarizing these results, we will discuss the suitable approach for the problems of the defects and impurities in perovskite-type oxide.

In Chapter 4, the role of the hydrogen (H) in $ATiO_3$ is discussed [92–95]. Even though the oxygen vacancy (V_{O}) and interstitial hydrogen ($\mathrm{H_i}$) have been considered to be generated under the hydrogen annealing, the relative stability between V_{O} and $\mathrm{H_i}$ has not been clarified yet in previous studies. We calculated the relative stability between V_{O} and $\mathrm{H_i}$, and the results are discussed. We will also show that various form of the hydrogen configurations are possible in $ATiO_3$, such as the replacement of an oxygen atom by one or two hydrogen atoms. An important finding in this chapter is that the hydrogen is not always a positively charged proton ($\mathrm{H^+}$), but they change their character from $\mathrm{H^+}$ (interstitial $\mathrm{H_i^+}$) to $\mathrm{H^-}$ (negatively charged hydride ion at oxygen vacancy site: $\mathrm{H_O^+}$) depending on their environments [93, 95]. We also calculated infrared (IR) absorption spectrum to predict experimental results for these hydrogen related defect species, such as $\mathrm{H_O}$ and $(\mathrm{2H})_{\mathrm{O}}$, which is a proposal for the future experiments to confirm the existence of these defect complexes. The diversity of hydrogen configuration and its role in $ATiO_3$ are discussed in this chapter.

In Chapter 5, relation between ferroelectricity in $BaTiO_3$ and donor-type

defects is discussed [96]. The disappearance of ferroelectricity in $BaTiO_3$ by various donor-type dopants is experimentally confirmed, but the origin of this phenomena has not been well understood yet. We separated the effects of experimental electron-doping into the effect of the carrier electron and the dopant induced lattice deformation, and separately evaluated each contribution to the elimination of the ferroelectricity. The series of analyses also offer a new viewpoint of the origin of ferroelectricity in $BaTiO_3$, where the counterbalance of short-range Pauli repulsive force and long-range Coulomb force determines the ferroelectric deformation potential. We also found that the elimination of the ferroelectric phase of $BaTiO_3$ is an intrinsic effect of carrier-electron doping and the lattice deformation accelerates the disappearance of the ferroelectricity in $BaTiO_3$.

Chapter 6 is devoted to concluding remarks based on the results obtained throughout the thesis work.

Chapter 2

Density functional theory

Density functional theory (DFT) has proven to be a very powerful tool for the prediction of material properties. The currently used formulation of DFT is based on a concept proposed by P. Hoenberg and W. Kohn in 1964 [97, 98]. They formulated DFT as an exact theory of many-body particle systems, where any property of a system of interacting many body electrons can be treated as a functional of the grand state charge density $n(\mathbf{r})$. However, DFT itself does not provide an actual way to construct such a functional of many body interacting particle system. The *ansatz* made by Kohn and Sham replaces the interacting problem with an auxiliary independent-particle problem, which provides a way to make approximated ground state functional [98,99]. This approach enables us to calculate properties of many-body systems using an independent-particle method with all many-body effects included in an exchange-correlation (XC) functional. The approach is the basis of most modern calculations called "first-principles" or "*ab initio*" for wide variety of materials including solids and molecules. The present chapter is devoted to the explanation of the basic formulation of the KS approach and the XC energy functional.

2.1 Formalism

2.1.1 Kohn-Sham energy functional

The Kohn-Sham (KS) approach [99] replaces the complicated interaction of many-body particle system with an independent and non-interacting particles of an auxiliary system that can be handled with actual numerical calculations. In the independent-particle equations for the non-interacting system, the concept of exchange-correlation (XC) is naturally introduced to make all

the difficulty in many-body effects to be incorporated into an XC functional of the grand state charge density. The KS approach writes the ground state energy functional in the form [98]:

$$E_{\mathrm{KS}} = T_s[n] + \int d\mathbf{r} V_{\mathrm{ext}}(\mathbf{r}) n(\mathbf{r}) + E_{\mathrm{Hartree}} + E_{\mathrm{XC}} + E_{\mathrm{Ewald}}, \tag{2.1}$$

where $V_{\mathrm{ext}}(\mathbf{r})$ is the external potential due to the nuclei and E_{Ewald} is the interaction between the nuclei. $n(\mathbf{r})$ is the charge density given by a sum of squares of the orbitals:

$$n(\mathbf{r}) = \sum_{\sigma} n(\mathbf{r}, \sigma) = \sum_{\sigma} \sum_{i=1}^{N^\sigma} |\psi_i^\sigma(\mathbf{r})|^2. \tag{2.2}$$

T_s is the kinetic energy given by

$$T_s = -\frac{1}{2} \sum_{\sigma} \sum_{i=1}^{N^\sigma} \langle \psi_i^\sigma | \nabla^2 | \psi_i^\sigma \rangle = -\frac{1}{2} \sum_{\sigma} \sum_{i=1}^{N^\sigma} \int d\mathbf{r} |\nabla \psi_i^\sigma(\mathbf{r})|^2, \tag{2.3}$$

and E_{Hartree} is the Hartree energy defined by the Coulomb interaction energy of the electron density interacting with itself:

$$E_{\mathrm{Hartree}} = \frac{1}{2} \int d\mathbf{r} d\mathbf{r}' \frac{n(\mathbf{r}) n(\mathbf{r}')}{|\mathbf{r} - \mathbf{r}'|}. \tag{2.4}$$

The term E_{XC} includes all many-body effects of exchange and correlation:

$$E_{\mathrm{xc}} = \sum_{\sigma} \int d\mathbf{r} n(\mathbf{r}, \sigma) \epsilon_{\mathrm{xc}}^\sigma([n], \mathbf{r}), \tag{2.5}$$

where $\epsilon_{\mathrm{xc}}^\sigma([n], \mathbf{r})$ is the exchange-correlation energy density that solely depends on the electron density $n(\mathbf{r}, \sigma)$. If the correct E_{XC} functional were known, then the ground state energy (and density) of the many-body electron system can be obtained correctly by solving the KS equations.

2.1.2 Kohn-Sham equations

The approach solving the Kohn-Sham energy equation in Eq. (2.1) can be viewed as a problem of minimization with respect to the electron density n($\mathbf{r}$). Since the terms in Eq. (2.1) are considered to be functionals of the density, variational principle can be applied to minimize $\Omega[\psi_i]$ with respect to ψ_i^*:

$$\Omega[\psi_i] = E_{\mathrm{KS}} - \sum_{\sigma} \sum_{i,j=1}^{N} \varepsilon_{ij}^\sigma \int d\mathbf{r} \psi_i^{\sigma *}(\mathbf{r}) \psi_j(\mathbf{r})^\sigma, \tag{2.6}$$

where ε_{ij} are Lagrange multipliers for the orthonormal condition of the wave functions:

$$\langle \psi_i^\sigma | \psi_j^{\sigma'} \rangle = \delta_{i,j}\delta_{\sigma,\sigma'}. \tag{2.7}$$

By using the chain rule, the variation of E_{KS} with respect to ψ_i^* is

$$\begin{aligned} \frac{\delta E_{\mathrm{KS}}}{\delta \psi_i^{\sigma *}} &= \frac{\delta T}{\delta \psi_i^{\sigma *}(\mathbf{r})} + \left[\frac{\delta E_{\mathrm{ext}}}{\delta n(\mathbf{r},\sigma)} + \frac{\delta E_{\mathrm{Hartree}}}{\delta n(\mathbf{r},\sigma)} + \frac{\delta E_{\mathrm{xc}}}{\delta n(\mathbf{r},\sigma)} \right] \frac{\delta n(\mathbf{r},\sigma)}{\delta \psi_i^{\sigma *}(\mathbf{r})} \\ &= \left[-\frac{1}{2}\nabla^2 + V_{\mathrm{ext}}(\mathbf{r}) + V_{\mathrm{Hartree}} + V_{\mathrm{xc}}^\sigma \right] \psi_i^\sigma(\mathbf{r}), \end{aligned} \tag{2.8}$$

where $V_{\mathrm{ext}}(\mathbf{r})$ is external potential due to nuclei, and V_{Hartree} is Hartree potential expressed by

$$V_{\mathrm{Hartree}} = \int d\mathbf{r}' \frac{n(\mathbf{r}')}{|\mathbf{r} - \mathbf{r}'|}. \tag{2.9}$$

V_{xc}^σ is exchange-correlation potential, and the actual form of the potential is explained in Sec. 2.1.3. The minimization of $\Omega[\psi_i]$ with respect to ψ_i^* leads to the following equations:

$$H_{\mathrm{KS}}^\sigma \psi_i^\sigma - \sum_{j=1}^{N} \varepsilon_{ij}^\sigma \psi_j^\sigma = 0, \tag{2.10}$$

where H_{KS}^σ is the Kohn-Sham effective hamiltonian:

$$H_{\mathrm{KS}}^\sigma = -\frac{1}{2}\nabla^2 + V_{\mathrm{ext}}(\mathbf{r}) + V_{\mathrm{Hartree}} + V_{\mathrm{xc}}^\sigma. \tag{2.11}$$

Since the H_{KS}^σ is a Hermitian operator, ε_{ij}^σ is a Hermitian matrix that can be diagonalized by a unitary transformation, which leaves the physical observables invariant. Thus, the Kohn-Sham Schrödinger-like equations are obtained as follows:

$$H_{\mathrm{KS}}^\sigma \psi_i^\sigma = \varepsilon_i^\sigma \psi_i^\sigma. \tag{2.12}$$

The total energy can be alternatively expressed in terms of the eigenvalues of the Kohn-Sham equations. The actual form is as follows:

$$E_{\mathrm{total}} = \sum_{\sigma,i} \varepsilon_i^\sigma + E_{\mathrm{xc}} - \sum_\sigma \int d\mathbf{r} n(\mathbf{r},\sigma) V_{xc}^\sigma(\mathbf{r}) - E_{\mathrm{Hartree}} + E_{\mathrm{Ewald}}. \tag{2.13}$$

2.1.3 Exchange correlation energy functional

The accuracy of DFT is limited by the approximation for the exchange-correlation (XC) functional. The XC term is composed of exchange and correlation terms.

$$E_{\mathrm{xc}} = E_{\mathrm{x}} + E_{\mathrm{c}}. \tag{2.14}$$

Local density approximation (LDA)

DFT has been very successful with local density approximation (LDA) that has been most commonly applied to the electronic structure calculation of solids. In LDA, the exchange-correlation term is a simple integral of the exchange-correlation energy density all over the space:

$$\begin{aligned} E_{\mathrm{XC}}^{\mathrm{LDA}} &= \int d\mathbf{r} n(\mathbf{r}) \epsilon_{\mathrm{XC}}^{\mathrm{hom}}([n], \mathbf{r}) \\ &= \int d\mathbf{r} n(\mathbf{r}) \left\{ \epsilon_{\mathrm{X}}^{\mathrm{hom}}([n], \mathbf{r}) + \epsilon_{\mathrm{C}}^{\mathrm{hom}}([n], \mathbf{r}) \right\}. \end{aligned} \tag{2.15}$$

The exchange-correlation potential V_{XC}^{σ} is obtained by the functional derivative of (2.15).

$$V_{\mathrm{XC}}^{\mathrm{LDA}} = \frac{\delta E_{\mathrm{XC}}^{\mathrm{LDA}}}{\delta n} = \left[\epsilon_{\mathrm{XC}}^{\mathrm{hom}} + n \frac{\partial \epsilon_{\mathrm{XC}}^{\mathrm{hom}}}{\partial n} \right]_{\mathbf{r},\sigma}. \tag{2.16}$$

The exchange term of the LDA is based on the exact expression for the Hartree-Fock exchange of the homogeneous gas that is exactly obtained. The expression of the exchange energy density is:

$$\epsilon_{\mathrm{X}}^{\mathrm{hom}}([n], \mathbf{r}) = -\frac{3}{4\pi} k_F = -\frac{3}{4\pi} (3\pi^2 n)^{\frac{1}{3}}, \tag{2.17}$$

where $k_F = (3\pi^2 n)^{\frac{1}{3}}$ is the Fermi wave vector corresponding to the density n of homogeneous electron gas. The form of exchange potential in LDA is very simple:

$$V_{\mathrm{X}}^{\mathrm{LDA}} = \frac{\delta E_{\mathrm{X}}^{\mathrm{LDA}}}{\delta n} = \frac{4}{3} \epsilon_{\mathrm{X}}^{\mathrm{hom}}([n], \mathbf{r}). \tag{2.18}$$

On the other hand, the form of the correlation term is not known exactly, because the correlation energy of a homogeneous electron is already a many-body problem of itself. Various approximations and fitting to numerical calculations has been proposed for the correlation energies for the homogeneous gas. The widely used functional made by Perdew and Zunger (PZ) is based on quantum Monte Carlo (QMC) calculations by Ceperley and

Alder (CA) [98, 100]. The correlation ϵ_c is fitted by polynomial. For example the form of PZ is:

$$\begin{aligned} \epsilon_c^{home} &\equiv \epsilon_c^{\mathrm{PZ}} \\ &= \begin{cases} -0.0480/(1 + 1.0529 r_s^{1/2} + 0.3334 r_s) & r_s \geq 1 \\ 0.031 \ln r_s - 0.0480 + 0.0020 r_s \ln r_s - 0.0116 & r_s < 1 \end{cases} \end{aligned} \tag{2.19}$$

The correlation potential is given by [98, 100]

$$V_{\mathrm{C}}^{\mathrm{LDA}} = \epsilon_{\mathrm{C}}(r_s) - \frac{r_s}{3} \frac{d\epsilon_{\mathrm{C}}(r_s)}{dr_s}. \tag{2.20}$$

where r_s is defined as the radius of a sphere containing one electron on average $(4\pi/3) r_s^3 = \Omega / N_{\mathrm{e}}$, namely:

$$r_s = \left(\frac{3}{4\pi n} \right)^{\frac{1}{3}}, \tag{2.21}$$

where n is density defined as $n = N_{\mathrm{e}}/\Omega$.

Gneralized-gradient approximation (GGA)

For the construction of various generalized-gradient approximations (GGAs), the magnitude of the gradient of the density $|\nabla n^\sigma|$ is required in addition to the value of n at each point. The addition of the gradient correction for the density n improves some of the drawbacks of the LDA, such as molecular binding energies, and some aspects of structural properties of solids. The form of the GGA exchange functional is:

$$E_{\mathrm{X}}^{\mathrm{GGA}} = \int d\mathbf{r} n(\mathbf{r}) \epsilon_{\mathrm{X}}^{\mathrm{hom}}([n], \mathbf{r}) F_{\mathrm{X}}(s), \tag{2.22}$$

where $F_{\mathrm{X}}(s)$ is a dimensionless function of enhancement factor including gradient of the density, and s denotes m-th order dimensionless reduced-density gradients that is defined by

$$s_m = \frac{|\nabla^m n|}{(2k_F)^m n}. \tag{2.23}$$

For exchange term, various forms for $F_{\mathrm{X}}(s)$ have been proposed, such as Becke(B88), Perdew-Wang (PW91), and Perdew–Burke–Ernzerhof (PBE)

functionals, which denote a variety of ways for the gradient corrections [98]. For example, $F_{\mathrm{X}}(s)$ of widely used PBE [101] has a form:

$$F_{\mathrm{X}}(s) = 1 + \kappa - \kappa/(1 + \mu s^2/\kappa), \tag{2.24}$$

where s is the 1st order of the density gradients $s \equiv s_1 = |\nabla n|/(2k_F n)$. κ and μ are parameters ($\kappa = 0.804, \mu = 0.21951$). The form in Eq. (2.24) recovers LDA with $F_X(s = 0) = 1$.

The form for GGA correlation is also expressed with local density plus gradient term.

$$E_{\mathrm{C}}^{\mathrm{PBE}} = \int d\mathbf{r} \left[\epsilon_{\mathrm{C}}^{hom} + H(r_s, \zeta, t)\right], \tag{2.25}$$

where $\zeta = (n \uparrow - n \downarrow)/n$ denotes spin polarization, r_s is the local Seitz radius ($n = 3/4\pi r_s^3 = k_F^3/3\pi^2$) , and $t = |\nabla n|/2\phi k_s n$ is a dimensionless density gradient. Here, $\phi(\zeta) = \left[(1+\zeta)^{2/3} + (1-\zeta)^{2/3}\right]/2$ is a spin-scaling factor, and $k_s = \sqrt{4k_F/\pi a_0}$ is the Thomas-Fermi screening wave number ($a_0 = \hbar^2/me^2$). H is written with ($e^2 = a_0 = 1$) as follows:

$$H^{\mathrm{PBE}} = \gamma\phi^3 \ln\left\{1 + \frac{\beta}{\gamma} t^2 \left[\frac{1 + At^2}{1 + At^2 + A^2t^4}\right]\right\}, \tag{2.26}$$

where $\beta = 0.066725, \gamma = 0.031091$ and $A = \frac{\beta}{\gamma}\left[\exp\{-\epsilon_c^{unif}/\gamma\phi^3\} - 1\right]^{-1}$.

2.1.4 Ultrasoft pseudopotentials and PAW

The concept of pseudopotential is the replacement of the bare Coulomb potential of the nuclei and the core electrons by an effective Coulomb potential acting only on the valence electrons. Pseudopotentials are generated on the basis of atomic calculation, and the core states are unchanged in the calculation of molecules or solids. The scheme is called "frozen core", which relies on the fact that the properties of materials are mainly characterized by valence orbital around the Fermi level. The idea of pseudopotential is also applied in the new formalism of self-interaction correction (SIC) method described in the sequential section.

Ultrasoft pseudopotentials

The cost of the plane-wave calculation depends on the number of Fourier components needed in the calculation, therefore the pseudo wave functions created with the pseudopotentials are desired to be as smooth as possible, and yet accurate. The approach of ultrasoft pseudopotential (USPP) proposed by D. Vanderbilt [102] involves a smooth function of pseudo wave function

$\tilde{\phi}$. The augmentation charge that is a difference in the norm from norm-conserving wave function (or true all electron wave function) is given by

$$Q_{ij}^{\tau} = \int_0^{R_c} Q_{ij}^{\tau}(\mathbf{r}) d\mathbf{r}, \tag{2.27}$$

where $Q_{ij}^{\tau}(\mathbf{r})$ are augmentation functions for atom τ:

$$Q_{ij}^{\tau}(\mathbf{r}) = \phi_i^{\tau *}(\mathbf{r})\phi_j^{\tau}(\mathbf{r}) - \tilde{\phi}_i^{\tau *}(\mathbf{r})\tilde{\phi}_j^{\tau}(\mathbf{r}). \tag{2.28}$$

Here, ϕ_i^{τ} are true all electron (AE) atomic orbital, and $\tilde{\phi}_j^{\tau}$ are pseudo-wave function inside a core radius. The advantage of ultrasoft pseudopotentials, which does not satisfy the norm conserving condition ($Q_{ij}^{\tau} = 0$), is that each smooth pseudo-wave function $\tilde{\phi}_j^{\tau}$ can be formulated with only the matching constraint of the functions $\tilde{\phi}_i^{\tau}(R_c) = \phi_i^{\tau}(R_c)$ at the core radius R_c. The flexibility of the pseudo-wave function makes the generation of extremely soft pseudopotentials possible in the USPP formalism.

The generalized eigenvalue equation for the ultrasoft pseudopotential is:

$$H^{\sigma} \left|\psi_{\sigma n \mathbf{k}}\right\rangle = \left[-\frac{1}{2}\nabla^2 + V_{\mathrm{loc}}^{\sigma} + V_{\mathrm{NL}}^{\sigma}\right] \left|\psi_{\sigma n \mathbf{k}}\right\rangle = \varepsilon_{\sigma n \mathbf{k}} S \left|\psi_{\sigma n \mathbf{k}}\right\rangle, \tag{2.29}$$

where S is the overlap operator,

$$S = 1 + \sum_{\tau,i,j} \left|\beta_i^{\tau}\right\rangle Q_{ij}^{\tau} \left\langle\beta_j^{\tau}\right|, \tag{2.30}$$

which is different from 1 only inside the core radius. In the calculation with ultrasoft pseudopotentials, the obtained pseudo wave function ψ_i are orthonormalized according to

$$\langle\psi_i|S|\psi_j\rangle = \delta_{i,j}. \tag{2.31}$$

$|\beta_i^{\tau}\rangle$ are projectors that satisfy the relation $\langle\beta_i^{\tau}|\tilde{\phi}_j^{\tau}\rangle = \delta_{ij}$,

$$\left|\beta_i^{\tau}\right\rangle = \sum_j (B^{-1})_{ij}^{\tau} \left|\chi_j^{\tau}\right\rangle, \tag{2.32}$$

where $B_{ij}^{\tau} = \langle\tilde{\phi}_i^{\tau}|\chi_j^{\tau}\rangle$, and $|\chi_i^{\tau}\rangle$ is a fanction vanishing for $r > r_{c,i}$:

$$\left|\chi_i^{\tau}\right\rangle = (\varepsilon_i - T - V_{\mathrm{loc}}) \left|\tilde{\phi}_i^{\tau}\right\rangle. \tag{2.33}$$

The non-local part V_{NL} is written as:

$$V_{\mathrm{NL}} = \sum_{\tau} \sum_{i,j} \left|\beta_i^{\tau}\right\rangle D_{ij}^{\tau} \left\langle\beta_j^{\tau}\right|, \tag{2.34}$$

where the definition of D_{ij}^{τ} is

$$D_{ij}^{\tau} = B_{ij}^{\tau} + \varepsilon_j Q_{ij}^{\tau}. \tag{2.35}$$

$V_{\rm loc}^{\sigma}$ is defined by

$$V_{\rm loc}^{\sigma} = V_{\rm loc}^{\rm ion} + V_{\rm H} + v_{\rm xc}^{\sigma}, \tag{2.36}$$

where $V_{\rm loc}^{\rm ion}$ is the local part of the pseudopotential located at atom-center position.

The valence charge density with USPP is defined to be

$$n(\mathbf{r}) = \sum_{n,\mathbf{k}}^{\rm occu.} \langle \psi_{\sigma n\mathbf{k}} | K(\mathbf{r}) | \psi_{\sigma n\mathbf{k}} \rangle^2 , \tag{2.37}$$

$$K(\mathbf{r}) = |\mathbf{r}\rangle \langle \mathbf{r}| + \sum_{\tau,i,j} |\beta_i^{\tau}\rangle \, Q_{ij}^{\tau} \, \langle \beta_j^{\tau}| . \tag{2.38}$$

The form of the total energy with USPP is

$$\begin{aligned} E_{\rm total} = & \sum_{\sigma n\mathbf{k}} \langle \psi_{\sigma n\mathbf{k}} | -\frac{1}{2}\nabla^2 + V_{\rm NL}^{(0)} | \psi_{\sigma n\mathbf{k}} \rangle + \int d\mathbf{r} n(\mathbf{r}) V_{\rm ion}^{\rm loc}(\mathbf{r}) \\ & + E_{\rm Hartree}[n] + E_{\rm xc}[n^{\uparrow}, n^{\downarrow}] + E_{\rm Ewald}. \end{aligned} \tag{2.39}$$

Here, $V_{\rm NL}^{(0)}$ is defined by

$$V_{\rm NL}^{(0)} = \sum_{\tau} \sum_{i,j} |\beta_i^{\tau}\rangle \, D_{ij}^{(0),\tau} \, \langle \beta_j^{\tau}| , \tag{2.40}$$

where $D_{i,j}^{(0),\tau}$ is

$$D_{ij}^{(0),\tau} = D_{ij}^{\tau} - \int d\mathbf{r} Q_{ij}^{\tau}(\mathbf{r}) V_{\rm loc}^{\sigma}(\mathbf{r}). \tag{2.41}$$

PAW method

The projector augmented wave (PAW) method is a general approach similar to the ultrasoft pseudopotential method at the point that it introduces projectors and auxiliary localized functions. Here, we only briefly explain the basic ideas of the definition of PAW method [103]. In the PAW method, the all electron (AE) wave function ψ_n is derived from the pseudo (PS) wave function $\tilde{\psi}_n$ with a linear transformation:

$$|\psi_n\rangle = |\tilde{\psi}_n\rangle + \sum_i (|\phi_i\rangle - |\tilde{\phi}_i\rangle) \, \langle \tilde{p}_i | \tilde{\psi}_n \rangle , \tag{2.42}$$

where the index i denote the atomic site $\mathbf{R}$ and angular momentum numbers $L = l, m$. ϕ_i are the AE wave function of isolated reference atom, and their PS waves functions are denoted by $\tilde{\phi}_i$ The projector functions $\tilde{p}_i$ that are dual to the partial waves fulfill the following relation:

$$\langle \tilde{p}_i | \tilde{\phi}_j \rangle = \delta_{ij}. \tag{2.43}$$

Starting from Eq. (2.42), the AE charge density in the PAW formalism is given by:

$$n(\mathbf{r}) = \tilde{n}(\mathbf{r}) + n^1(\mathbf{r}) - \tilde{n}^1(\mathbf{r}), \tag{2.44}$$

where $\tilde{n}(\mathbf{r})$ is soft pseudo-charge density expressed as follows:

$$\tilde{n}(\mathbf{r}) = \sum_n f_n \langle \tilde{\psi}_n | \mathbf{r} \rangle \langle \mathbf{r} | \tilde{\psi}_n \rangle . \tag{2.45}$$

$n^1(\mathbf{r})$ and $\tilde{n}^1(\mathbf{r})$ are onsite charge densities:

$$n^1(\mathbf{r}) = \sum_{ij} \rho_{ij} \langle \phi_i | \mathbf{r} \rangle \langle \mathbf{r} | \phi_j \rangle , \tag{2.46}$$

$$\tilde{n}^1(\mathbf{r}) = \sum_{ij} \rho_{ij} \langle \tilde{\phi}_i | \mathbf{r} \rangle \langle \mathbf{r} | \tilde{\phi}_j \rangle , \tag{2.47}$$

where ρ_{ij} are the occupation matrix of each augmentation channel (i, j) that are expressed by

$$\rho_{ij} = \sum_n f_n \langle \tilde{\psi}_n | \tilde{p}_i \rangle \langle \tilde{p}_i | \tilde{\psi}_n \rangle . \tag{2.48}$$

Due to the expression of the full wave function, the final expression of the total energy is composed of the sum of three terms similar to the expression of density as shown in Eq. (2.44). The form of the total energy in PAW method becomes: [1]

$$E = \tilde{E} + E^1 - \tilde{E}^1, \tag{2.49}$$

where $\tilde{E}$ denotes the energy due to the smooth functions calculated in Fourier space or on a regular grid that extends throughout space, whereas E^1 and

[1] The actual form of $\tilde{E}$ is $\tilde{E} = \sum_n f_n \langle \tilde{\psi}_n | - \frac{1}{2}\nabla^2 | \tilde{\psi}_n \rangle + E_{\mathrm{XC}}[\tilde{n} + \hat{n} + \tilde{n}_c] + E_{\mathrm{H}}[\tilde{n} + \hat{n}] + \int v_{\mathrm{H}}[\tilde{n}_{Z_c}](\tilde{n}(\mathbf{r}) + \hat{n}(\mathbf{r}))d\mathbf{r} + U_{\mathrm{Ewald}}(\mathbf{R}, Z_{\mathrm{ion}})$, where $\hat{n}$ is compensation charge, and $\tilde{n}_c$ is component of core charge. The expressions of E^1 and $\tilde{E}^1$ are similar to this expression, expect for the selection of corresponding wave function and charge components. See ref. [103] for more detailed explanation.

$\tilde{E}^1$ are calculated individually on a radial sphere grid. The basic Kohn-Sham equations are obtained from the variational principles on the energy functional shown in Eq. (2.49) [103].

The main difference between the USPP and the PAW is that the PAW method keeps the full all-electron wave function in a form shown by Eq. (2.42). It is especially noted that the expressions for the total energy of PAW are closely related to that in the ultrasoft formalism, where only difference is the choice of auxiliary functions and mathematical deformation aspects. Thus, other derived properties, such as force and stress, are essentially the same.

2.1.5 Density of states (DOS)

Density of states (DOS) for a given band n is defined as:

$$D(E) = \int \frac{d\mathbf{k}}{4\pi^3} \delta(E - E_n(\mathbf{k})), \tag{2.50}$$

where $E_n(\mathbf{k})$ is the dispersion of the band, and the integral is performed over Brillouin zone. The total density of states $D(E)$ is obtained by summation over all bands. For the calculation of the DOS, the simplest method is based on the sampling for energy levels of each band with Gaussian smearing. Even though the Gaussian smearing does not reproduce the detail of electronic structure, such as the broad metallic conduction bands, it satisfactorily reproduce the general shape of the electronic structure, especially with dense k-point sampling. More accurate methods are based on linear interpolations of band energies between two points in the Brillouin zone, and the most popular technique is the tetrahedron interpolation. However, the tetrahedron method is unfortunately not well suited to the Monkhorst-Pack k-point special sampling.

Partial density of states (PDOS) is useful for qualitative analysis of the electronic structure. The PDOS calculations are based on Mulliken population analysis, which allows evaluation for the contribution from each energy band to a given atomic orbital. PDOS can qualify the DOS results by resolving the contributions according to the angular momentum (s, p, or d characters) of specified atomic orbitals. By using DOS and PDOS, we can analyze qualitative nature of the electronic structure, such as the orbital hybridization in the system.

2.2 Improved exchange-correlation functional

The accuracy of the local density approximation (LDA) or various generalized-gradient approximations (GGAs) is extremely degraded for strongly correlated cases. For example, transition metal mono oxides NiO and CuO are antiferromagnetic insulators, whereas LDA or GGA functionals find them to be metals. The difficulty of the correct calculation for the band gap has been discussed as a serious problem inhered in LDA.

The Kohn-Sham eigenvalues have no physical meaning in the extended system of solids. The only exception is the highest eigenvalue in a finite system, where the highest-occupied eigenvalue is minus the value of the ionization energy $-I$, which are known as Slater-Janak theorem.

$$\varepsilon_i = \frac{dE_{\text{total}}}{dn_i} = \int d\mathbf{r} \frac{dE_{\text{total}}}{dn(\mathbf{r})} \frac{dn(\mathbf{r})}{dn_i}, \tag{2.51}$$

where the eigenvalue is the derivative of the total energy with respect to the occupation of a state. As shown in Eq. (2.16), the effective potential $V_{\text{XC}}(\mathbf{r})$ in the derivative in Eq. (2.51) has a form:

$$V_{\text{XC}} = \epsilon_{\text{XC}}([n], \mathbf{r}) + n(\mathbf{r}) \frac{\delta \epsilon_{\text{XC}}([n], \mathbf{r})}{\delta n(\mathbf{r})}, \tag{2.52}$$

where $V_{\text{XC}}(\mathbf{r})$ contains a "response part" that is the derivative of ϵ with respect to $n(\mathbf{r})$. The important point is the discontinuity of this part between states. J. P. Perdew and M. Levy pointed out that the Kohn-Sham band structure underestimates the gap width by an amount equal to the derivative discontinuity C [104]:

$$C = \left. \frac{\delta E_{\text{XC}}}{\delta n(\mathbf{r})} \right|_{N+\delta} - \left. \frac{\delta E_{\text{XC}}}{\delta n(\mathbf{r})} \right|_{N-\delta}, \tag{2.53}$$

where N is the total number of electrons. Accordingly, in principle, the ground state Kohn-Sham potential should not be the correct gap. This is a critical problem of the gap in insulator calculated with Kohn-Sham equations.

The expression of the kinetic energy as a function of the independent-particle orbital ψ_i is of essential importance in the improvement of the Kohn-Sham approach. The derivative of kinetic energy (dT_s/dn) are discontinues at filled state in insulator. Suggested by the discontinuous properties of the kinetic energy, the improvement of E_{XC} functional that explicitly depends on the independent-particle orbital ψ_i has been discussed. These approaches are known as optimized effective potential method (OEP), where the key

point is the definition of the OEP energy functional E_{OEP} (and potential V_{OEP}) that includes orbitals ψ_i determined by the potential from the usual independent-particle Schrödinger equation [98]:

$$E_{\mathrm{OEP}}[V] = E[\{\psi_i[V]\}]. \tag{2.54}$$

The Hartee-Fock exchange functional is straightforward to be written in terms of the orbitals, and it has been applied to the OEP method. The method is called exact exchange (EXX). In this chapter, we introduce a fixed amount of the (screened) Hartree-Fock exchange into GGA, which is so-called hybrid functionals. By applying the hybrid functionals, a significant improvement over the GGA description of electronic structure is expected. We also introduce other types of orbital-dependent functionals through the introduction of occupancy n_i, which are the SIC and the LDA+U explained in the following subsections.

2.2.1 Self-Interaction Correction (SIC)

The SIC-LDA (or SIC-LSDA) that is originally proposed by Perdew and Zunger [100] is based on a direct subtraction of self-interaction (SI) contribution from the LDA (or LSDA) KS potential (PZ-SIC):

$$V_{\mathrm{HXC}}[n, m] \rightarrow V_{\mathrm{HXC}}[n, m] - V_{\mathrm{HXC}}[n_i], \tag{2.55}$$

where n and m are the total charge and magnetization densities. n_i is charge density of the i-th orbital. Despite the simplicity of its formalism, the SIC-LDA gives a much better agreement between modified KS eigenvalues and experimental ionization potentials (IP) and electron affinities (EA), and successfully applied to the calculation of atomic properties [100]. On the other hand, in the crystal where the eigenvectors of the KS equation are Bloch states, the SI of the Bloch state becomes an ill-defined quantity that depends on the normalization of the wave function, and the SI vanishes in the thermodynamic (delocalized) limit of a Bloch state [100]. Moreover, the wave functions obtained from Eq. (2.55) are no longer orthogonal because of the introduction of orbital-dependent spatially-localized SIC potential. Therefore, the direct application of SIC-LSDA in Eq. (2.55) has some difficulties in actual calculation in crystal system.

An efficient way to avoid the difficulty is the utilization of SIC operator with a form of nonlocal projector generated from free atom. The idea is initially suggested by Vogel *et al.* as SIC-PP [105], where atomic SIC are incorporated within the nonlocal projectors in pseudopotential. The scheme

is further improved by Filippetti *et al.* as pseudo SIC [106]. Within pseudo-SIC, the SIC term incorporated in the pseudopotential is separated into to an isolated SIC potential operator, which is composed of a nonlocal projector resembling the nonlocal part of the pseudopotential. Then, SIC-KS potential in Eq. (2.55) becomes:

$$V_{\mathrm{HXC}}[n,m] \rightarrow V_{\mathrm{HXC}}[n,m] - \sum_i |P_i\rangle\, V_{\mathrm{HXC}}[n_i]\, \langle P_i|\,, \tag{2.56}$$

where n and m are total charge and magnetization densities of crystal. The i is cumulative index written in terms of atomic quantities ($i = [(l_i, m_i), \mathbf{R}_i]$) $V_{\mathrm{HXC}}[n_i]$ is atomic SIC potential composed of Hartree, exchange and correlation of isolated atom. P_i are projector functions, such as spherical harmonics. n_i are the charge densities of the i-th atomic orbital ϕ_i,

$$n_i(\mathbf{r}) = p_i |\phi_i(\mathbf{r})|^2, \tag{2.57}$$

where p_i are fractional occupation numbers calculated from the projection of atomic orbital at each atomic site onto the occupied wave functions,

$$p_i = \sum_{n,\mathbf{k}} f_{n,\mathbf{k}}\, \langle \psi_{n,\mathbf{k}}|\phi_i\rangle\, \langle \phi_i|\psi_{n,\mathbf{k}}\rangle\,. \tag{2.58}$$

In the construction of pseudo SIC potentials, a linear dependence of the SI potential on the occupation numbers are assumed:

$$V_{\mathrm{HXC}}[n_i] = p_i V_{\mathrm{HXC}}[n_i; p_i = 1]. \tag{2.59}$$

Once $V_{\mathrm{HXC}}[n_i; p_i = 1]$ is calculated from atomic orbitals, the value is kept constant and only the p_i is updated during the self-consistent calculations. The procedure greatly reduces computational costs, which makes the SIC possible for the actual calculations of solid state materials [106]. The SIC potential in Eq. (2.56) recovers its original formula of PZ-SIC in atomic limit shown in Eq. (2.55) without introducing dependence of the KS Hamiltonian on the wave function in solids.

The pseudo SIC operator is a modification of SIC potential in Eq. (2.56) into a fully nonlocal, Kleinman-Bylander projector:

$$\hat{V}_{\mathrm{SIC}} = \alpha \sum_i \frac{|V_{\mathrm{HXC}}[n_i]\phi_i\rangle\, p_i\, \langle V_{\mathrm{HXC}}[n_i]\phi_i|}{\langle \phi_i|V_{\mathrm{HXC}}|\phi_i\rangle}, \tag{2.60}$$

where α is a screening factor. The selection of $\alpha = 1$ correctly reproduces the proper atomic limit of the SIC potential. In particular for molecules, both

ionization potential (IP) and electron affinity (EA) can be obtained with good accuracy from HOMO and LUMO eigenvalues of the SIC-KS equations [107]. On the other hand, the band gaps of solids are greatly overestimated with $\alpha = 1$. Filippetti *et. al* [106] suggested $\alpha = 1/2$ from the consideration of eigenvalue relaxation, which corrects the band gaps of III-V and II-VI semiconductors surprisingly well. We will refer the SIC implementation with $\alpha = 1/2$ to pseudo SIC here after. Finally, the Pseudo-SIC KS equation that should be solved is a slight modification of original KS equation as follows:

$$[\hat{H}_{\mathrm{LDA}} - \hat{V}_{\mathrm{SIC}}] \, |\psi_{n,\mathbf{k}}\rangle = \varepsilon_{n,\mathbf{k}} \, |\psi_{n,\mathbf{k}}\rangle \, . \tag{2.61}$$

In SIC-LSDA, the general energy functional is:

$$E_{\mathrm{SIC}}[n,m] = E[n,m] - \sum_{i,\sigma} E_{\mathrm{HXC}}[n_i^\sigma], \tag{2.62}$$

where $E[n,m]$ is the LSDA energy functional and $E_{\mathrm{HXC}}[n_i^\sigma]$ is Hartree exchange-correlation energy for i-th orbital charge.

$$E_{\mathrm{HXC}}[n_i^\sigma] = \int d\mathbf{r} \left(\frac{1}{2} V_{\mathrm{H}}[n_i^\sigma(\mathbf{r})] + E_{\mathrm{XC}}[n_i^\sigma(\mathbf{r})] \right). \tag{2.63}$$

A serious drawback for the SIC-KS equation is that a physically meaningful energy functional by a variational principle is not available, which means, in principle, the total energy cannot be obtained within the theoretical framework of SIC approach. [2] It is a general failure for SIC-LSDA approaches [106]. Within the first-order perturbation, the shift of pseudo SIC eigenvalues from LDA is:

$$\begin{aligned} \Delta\varepsilon_i &= -\langle\psi_i| \, \hat{V}_{\mathrm{SIC}} \, |\psi_i\rangle \\ &= -\frac{p_i}{2} \langle\psi_i| \, V_{\mathrm{HXC}}[n_i] \, |\psi_i\rangle \, . \end{aligned} \tag{2.65}$$

[2] However, in the pseudo-SIC formalism, auxiliary form of the total-energy functional has been proposed based on the Eq. (2.61) [106]. In terms of eigenvalues, the SIC-KS energy can be written as follows:

$$\begin{aligned} E_{\mathrm{SIC}}[n,m] &= \sum_{i,\sigma} f_{n,\mathbf{k}}^\sigma \varepsilon_{n\mathbf{k}}\sigma - \sum_\sigma \int d\mathbf{r} n^\sigma(\mathbf{r}) V_{\mathrm{HXC}}^\sigma[n(\mathbf{r}), m(\mathbf{r})] \\ &+ E_{\mathrm{HXC}}[n,m] + E_{\mathrm{ion}} \\ &+ \sum_{n,\mathbf{k},\sigma} f_{n,\mathbf{k}}^\sigma \langle\psi_{n,\mathbf{k}}^\sigma|\hat{V}_{\mathrm{SIC}^\sigma}|\psi_{\mathrm{n},\mathbf{k}}^\sigma\rangle - \sum_{i,\sigma} E_{\mathrm{HXC}}[n_i^\sigma], \end{aligned} \tag{2.64}$$

where the first three terms are expressions of the total energy in DFT, and the last two terms are corrections based on pseudo SIC theoretical framework.

The $V_{\rm HXC}[n_i]$ is always positive because the Hartree potential (positive) is always stronger than exchange correlation potential (positive or negative). Therefore the shift of SIC eigenvalues from LDA eigenvalues always has a negative sign.

We implemented the pseudo SIC method in *Tokyo ab inito programming package* (TAPP) that is an electronic-structure calculation code based on DFT. The actual implementation is slightly different from the above explanation, because our implementation and calculation of materials are based on ultrasoft pseudopotential (USPP). The formulation of the pseudo SIC for the USPP is explained in Appendix section.

2.2.2 DFT+U

The expression of DFT+U energy functional is derived from model Hamiltonian, originally Hubbard model [108]. The inclusion of a natural representation of strongly correlated materials has allowed to study a large variety of strongly correlated materials with considerable improvement over L(S)DA or GGA results. The successes of the method have led to further developments of DFT+U theoretical framework, which have produced sophisticated and efficient numerical formula. In DFT+U, some localized orbitals that represent the localization of electrons are selected, and they are used to treat the electronic correlation in a special way. In its original definition, the +U functional was not invariant under rotation of the localized orbitals that are used to calculate the occupancies n_i. The problem was solved by rotationally invariant formalisms proposed later [109–111]. In this subsection, we explain the rotationally invariant LDA+U formalism [111], which are used in our calculations. [3]

The LDA+U energy functional is:

$$E_{\rm LDA+U} = E_{\rm LDA} + E_U, \tag{2.66}$$

where E_U is the rotational invariant on-site correction:

$$\begin{aligned} E_U[\{n^{\tau\sigma}_{mm'}\}] &= \frac{U_{\rm eff}}{2}\sum_{\tau}\sum_{m\sigma}\left(n^{\tau\sigma}_{mm} - \sum_{m'} n^{\tau\sigma}_{mm'}n^{\tau\sigma}_{m'm}\right) \\ &= \frac{U_{\rm eff}}{2}\sum_{\tau\sigma} Tr[\mathbf{n}^{\tau\sigma}\,(1-\mathbf{n}^{\tau\sigma})]. \end{aligned} \tag{2.67}$$

[3] We implemented the rotationally invariant LDA+U in TAPP according to the implementation explained in Ref. [111].

$\mathbf{n}^{\tau\sigma}$ is occupation matrix (on-site density matrix) defined as: [4]

$$n^{\tau\sigma}_{mm'} = \sum_{n,\mathbf{k}} f_{n,\mathbf{k}} \left\langle \psi^{\sigma}_{n,\mathbf{k}} | \Phi^{\tau}_{m} \right\rangle \left\langle \Phi^{\tau}_{m'} | \psi^{\sigma}_{n,\mathbf{k}} \right\rangle , \tag{2.68}$$

where Φ^{τ}_{m} is localized (atomic) orbitals. $\psi_{n,\mathbf{k}}$ are the pseudo-wave functions and $f_{n,\mathbf{k}}$ are the occupation numbers.

The $+U$ operator is obtained by derivative of E_U by $\psi^{\sigma *}_{n,\mathbf{k}}$:

$$\begin{aligned} \frac{\partial E_U}{\partial \psi^{\sigma *}_{n,\mathbf{k}}} &= \frac{U_{eff}}{2} \frac{\partial}{\psi^{\sigma}_{n,\mathbf{k}} *} \sum_{\tau} \sum_{m\sigma} \left(n^{\tau\sigma}_{mm} - \sum_{m'} n^{\tau\sigma}_{mm'} n^{\tau\sigma}_{m'm} \right) \\ &= \frac{U_{eff}}{2} \sum_{\tau m} \left(\frac{\partial n^{\tau\sigma}_{mm}}{\psi^{\sigma *}_{n,\mathbf{k}}} - \frac{\partial}{\psi^{\sigma *}_{n,\mathbf{k}}} \sum_{m'} n^{\tau\sigma}_{mm'} n^{\tau\sigma}_{m'm} \right) . \end{aligned} \tag{2.69}$$

The first and second terms in Eq.(2.69) becomes

$$\begin{aligned} \sum_{\tau,m} \frac{\partial n^{\tau\sigma}_{mm}}{\psi^{\sigma *}_{n,\mathbf{k}}} &= \sum_{\tau,m} \frac{\partial}{\psi^{\sigma *}_{n,\mathbf{k}}} \sum_{n,\mathbf{k}} f_{n,\mathbf{k}} \left\langle \psi^{\sigma}_{n,\mathbf{k}} | \Phi^{\tau}_{m} \right\rangle \left\langle \Phi^{\tau}_{m} | \psi^{\sigma}_{n,\mathbf{k}} \right\rangle \\ &= \sum_{\tau,m} | \Phi^{\tau}_{m} \rangle \left\langle \Phi^{\tau}_{m} | \psi^{\sigma}_{n,\mathbf{k}} \right\rangle , \end{aligned} \tag{2.70}$$

and

$$\begin{aligned} \sum_{\tau,m} \frac{\partial}{\partial \psi^{\sigma *}_{n,\mathbf{k}}} \sum_{m'} n^{\tau\sigma}_{mm'} n^{\tau\sigma}_{m'm} &= \sum_{\tau,m} \sum_{m'} \left(\frac{\partial n^{\tau\sigma}_{mm'}}{\partial \psi^{\sigma *}_{n,\mathbf{k}}} n^{\tau\sigma}_{m'm} + n^{\tau\sigma}_{mm'} \frac{\partial n^{\tau\sigma}_{m'm}}{\partial \psi^{\sigma *}_{n,\mathbf{k}}} \right) \\ &= 2 \sum_{\tau,m} \sum_{m'} n^{\tau\sigma}_{mm'} \frac{\partial n^{\tau\sigma}_{m'm}}{\partial \psi^{\sigma *}_{n,\mathbf{k}}} \\ &= 2 \sum_{\tau,m} \sum_{m'} | \Phi^{\tau}_{m'} \rangle \, n^{\tau\sigma}_{mm'} \left\langle \Phi^{\tau}_{m} | \psi^{\sigma}_{n,\mathbf{k}} \right\rangle . \end{aligned} \tag{2.71}$$

Hence, Eq.(2.69) becomes

$$\frac{\partial E_U}{\partial \psi^{\sigma *}_{n,\mathbf{k}}} = \frac{U_{\text{eff}}}{2} \sum_{\tau,m} \left(| \Phi^{\tau}_{m} \rangle \left\langle \Phi^{\tau}_{m} | - 2 \sum_{m'} | \Phi^{\tau}_{m'} \rangle \, n^{\tau\sigma}_{mm'} \left\langle \Phi^{\tau}_{m} | \right. \right) | \psi^{\sigma}_{n,\mathbf{k}} \rangle . \tag{2.72}$$

[4] This is a representation with norm conserving pseudopotential (NCPP), whereas actual calculations are performed with ultrasoft pseudopotential (USPP). The formulation of LDA+U under USPP is explained in Appendix.

Therefore, the potential $\hat{V}_U^\sigma$ acting on KS equations is

$$\hat{V}_U^\sigma = \frac{U_{eff}}{2} \sum_\tau \left(\sum_m |\Phi_m^\tau\rangle \langle \Phi_m^\tau| - 2 \sum_{mm'} |\Phi_{m'}^\tau\rangle \, n_{mm'}^{\tau\sigma} \, \langle \Phi_m^\tau| \right). \tag{2.73}$$

In the atomic limit for atom τ, where $n_{mm}^{\tau\sigma} \equiv n_m^\sigma$, the +U term can be simplified as

$$E_{U_{\mathrm{atom}\tau}} = \frac{U_{\mathrm{eff}}}{2} \sum_{m\sigma} \left(n_m^\sigma - \sum_m (n_m^\sigma)^2 \right). \tag{2.74}$$

The one-electron potential is given by the derivative of Eq. (2.74)

$$\begin{aligned} v_l^\sigma &= \frac{\partial E_{U_{\mathrm{atom}\tau}}}{\partial n_l^\sigma} = \frac{\partial}{\partial n_l^\sigma} \frac{U_{\mathrm{eff}}}{2} \sum_{m\sigma} \left(n_m^\sigma - \sum_m (n_m^\sigma)^2 \right) \\ &= -U_{\mathrm{eff}} \left(n_l^\sigma - \frac{1}{2} \right). \end{aligned} \tag{2.75}$$

The relation shown in Eq. (2.75) denotes the general effect of DFT+U on the expected shift of eigenvalues as a result of $+U$ potential. The shifts of the eigenvalues are determined by the occupation n_l^σ, where $n_l^\sigma > 1/2$ (generally occupied states) bring about the downward shift, and the upward shift with $n_l^\sigma < 1/2$ (generally unoccupied states). When $n_l^\sigma = 1/2$, the one-electron potential vanishes and no changes are induced. The behavior of the $+U$ potential for occupied and unoccupied states bring about the improvement of calculated gaps. However, the improvement is restricted to the material which satisfy the special condition of the occupation, therefore great care is needed for the selection of the localized orbital Φ^τ and U_{eff} value in the actual calculations.

2.2.3 Hybrid Functional

Hybrid functionals are explicit orbital-dependent functionals in which fractional portion of Fock exchange (exact exchange, EXX) is introduced into DFT exchange-correlation (XC) functional. While the hybrid functionals have rapidly grown as a standard tool in quantum chemistry, their application to the electronic-structure calculation of solid is much more recent due to the high-computational cost required for the calculation of nonlocal EXX term with plane-wave basis set. Even though the way for the mixture of these two different XC terms is a nontrivial issue, non-empirical calculations can

be performed under the defined mixture of the hybridization ratio. A simple model for the hybrid of DFT and HF has been proposed as follows [112]:

$$E_{\mathrm{XC}}^{\mathrm{hybrid}} = E_{\mathrm{XC}}^{\mathrm{DFT}} + \frac{1}{n}(E_{\mathrm{X}}^{\mathrm{HF}} - E_{\mathrm{X}}^{\mathrm{DFT}}), \tag{2.76}$$

where $E_{\mathrm{X}}^{\mathrm{DFT}}$ and $E_{\mathrm{XC}}^{\mathrm{DFT}}$ are the exchange and the exchange-correlation of DFT (XC of GGA-PBE) and n is an integer number. In the above expression, $n = 1$ incorporates 100% exact exchange with PBE correlation, $n = 4$ corresponds to PBE0, and $n \to \infty$ results in GGA-PBE. In PBE0, the exchange term of the functional is constructed by a mixing of 25% Fock exchange and 75% PBE exchange in PBE0, where the electron correlation is treated within the PBE formalism. The resulting expression for the exchange-correlation energy for "parameter-free" PBE0 takes the following form:

$$E_{\mathrm{XC}}^{\mathrm{PBE0}} = \frac{1}{4}E_{\mathrm{X}}^{\mathrm{HF}} + \frac{3}{4}E_{\mathrm{X}}^{\mathrm{PBE}} + E_{\mathrm{C}}^{\mathrm{PBE}}. \tag{2.77}$$

The Fock exchange energy $E_{\mathrm{X}}^{\mathrm{HF}}$ is written as

$$\begin{aligned} E_{\mathrm{X}}^{\mathrm{HF}} = & - \frac{1}{2}\sum_{\mathbf{k}n,\mathbf{q}m} 2w_{\mathbf{k}} f_{\mathbf{k}n} \times 2w_{\mathbf{q}} f_{\mathbf{q}m} \\ & \times \iint d^3\mathbf{r} d^3\mathbf{r}' \frac{\psi_{\mathbf{k}n}^*(\mathbf{r})\psi_{\mathbf{k}n}(\mathbf{r}')\psi_{\mathbf{q}m}(\mathbf{r})\psi_{\mathbf{q}m}^*(\mathbf{r}')}{|\mathbf{r}-\mathbf{r}'|}, \end{aligned} \tag{2.78}$$

where the terms are calculated in terms of the set of one-electron Bloch state $\{\psi_{\mathbf{k}n}(\mathbf{r})\}$, and corresponding set of occupation numbers $\{f_{\mathbf{k}n}\}$. The sums over $\mathbf{k}$ and $\mathbf{q}$ must be performed over all k points sampled in the Brillouin zone (BZ) with weights $w_{\mathbf{k}}$ specified by Monkhorst-Pack scheme. The factors 2 account for the spin multiplicity of the system with doubly occupied one-electron states. The nonlocal HF exchange potential obtained by the derivative of E_{X} by $\psi_{\mathbf{k}n}^*(\mathbf{r})$ is:

$$V_{\mathrm{X}}(\mathbf{r},\mathbf{r}') = -2\sum_{\mathbf{q}m} w_{\mathbf{q}} f_{\mathbf{q}m} \frac{\psi_{\mathbf{q}m}^*(\mathbf{r}')\psi_{\mathbf{q}m}(\mathbf{r})}{|\mathbf{r}-\mathbf{r}'|}. \tag{2.79}$$

One of the difficulties in evaluating the Fock exchange arises from the slow decay of the exchange interaction with distance. Heyd *etal.* [113] addresses the problem by separating the exchange interaction into a short- and a long-range part, and only the short-range Fock exchange are mixed with DFT exchange, leaving the DFT correlation unchanged, which are called Heyd–Scuseria–Ernzerhof (HSE) screened Coulomb hybrid DFT [113, 114]. Since

the computational cost for Fock exchange scales quadratically with the number of k mesh, the HSE functional considerably reduces the computational costs. The starting point of the HSE hybrid functional is the PBE0 hybrid functional. In the formalism of HSE, the HF exchange are divided into short-range (sr) and long-range (lr) parts to avoid the slow convergence of the HF exchange interaction with distance, and the slowly decaying long-rage part of the HF exchange are neglected:

$$E_{\mathrm{XC}}^{\mathrm{HSE}} = \frac{1}{4}E_{\mathrm{X}}^{\mathrm{sr,\ HF}} + \frac{3}{4}E_{\mathrm{X}}^{\mathrm{sr,\ PBE}} + E_{\mathrm{X}}^{\mathrm{lr,\ PBE}} + E_{\mathrm{C}}^{\mathrm{PBE}}, \tag{2.80}$$

and the separation is accomplished through a decomposition of the Coulomb kernel:

$$\frac{1}{r} = S_\mu(r) + L_\mu(r) = \frac{\mathrm{erfc}(\mu r)}{r} + \frac{\mathrm{erf}(\mu r)}{r}, \tag{2.81}$$

where $\mathrm{erfc}(\mu r)$ is complementary error function: $\mathrm{erfc}(\mu r) = 1 - \mathrm{erf}(\mu r)$. It has been empirically established that the optimum range-separation parameter is 0.207 $\mathrm{\AA}^{-1}$.

Now, it is useful for us to consider the effects of the Fock exchange on the shift of the eigenvalues. Within the first-order perturbation, the shift of eigenvalues by the Fock exchange potential is:

$$\begin{aligned} & \langle\psi(\mathbf{r})_l|\, V_{\mathrm{X}}(\mathbf{r},\mathbf{r}')\, |\psi(\mathbf{r})_l\rangle \\ = \ & -2 \sum_{m:\mathrm{occupied}} \iint d^3\mathbf{r} d^3\mathbf{r}' \frac{\psi_l(\mathbf{r})\psi_m^*(\mathbf{r}')\psi_m(\mathbf{r})\psi_l^*(\mathbf{r})}{|\mathbf{r}-\mathbf{r}'|}. \end{aligned} \tag{2.82}$$

In Eq. (2.82), the component of the occupied state has a larger value than the unoccupied state, because the summation over m is performed only for the occupied states, which indicate large downward shift of the eigenvalues of the occupied states. Thus, the introduction of fractional portion of Fock exchange into XC of GGA is expected to improve the gap that is originally underestimated by GGA.

2.3 Effects of improved XC functionals

By applying the improved XC functionals that we have already introduced, the improvement of the overall electronic structures is expected compared to the ones calculated with LDA or GGA. The improvement of the basic electronic structure is of great importance as a first step for the calculation of defect in solid, because the stability of the defect states strongly depends on the basic electronic structure, such as band gap value, of the host crystal. This section is devoted to the explanation how these beyond LDA functionals, such as LDA+U, SIC, and hybrid functionals modify the eigenvalues of the KS equations, which lead to the improvement of calculated band structures. Calculations are performed mainly for the $SrTiO_3$ unitcell, and the improvements of the band gap values are discussed. For the deep understanding, some reference materials are also calculated and the effects of XC functional on the electronic structures are discussed.

2.3.1 Band structures of $SrTiO_3$

Figure 2.1 shows the band structure of $SrTiO_3$ calculated with various XC functionals described in the above section. In all the band structures, conduction band minimum (CBM) is at Γ point, whereas X point is very close in energy. The valence band maximum (VBM) is located at R point. The overall natures of the band structures are not so much different from each other. The large difference is the calculated gap values; LDA shows the underestimated band gap value of 1.75 eV, whereas the experimental value is 3.2 eV. This is the well-known drawback of the LDA (and also GGA whose gap value is 1.86 eV), which can be corrected by improved XC functionals.

LDA+U

The partial density of states (PDOS) for each orbital, that is the projection of the total density of states (total DOS) on the isolated atomic orbitals, are the key to understand the behavior of LDA+U (and pseudo SIC) whose theoretical framework is based on the occupation n_i for i-th atomic orbital. Figure 2.2 shows the PDOS of Ti-3d in $SrTiO_3$ calculated with LDA, which indicates that the conduction band minim (CBM) of $SrTiO_3$ is mainly composed of Ti-3d t_{2g} orbitals with widely spreading e_g orbitals at higher energy region. The valence band (VB) is mainly composed of O-2p, and there is a small hybridization between O-2p and Ti-3d. Even though the nominal valence charge is Ti-3d^0, the occupation $n_{\mathrm{Ti},3d}$ has non zero value due to the

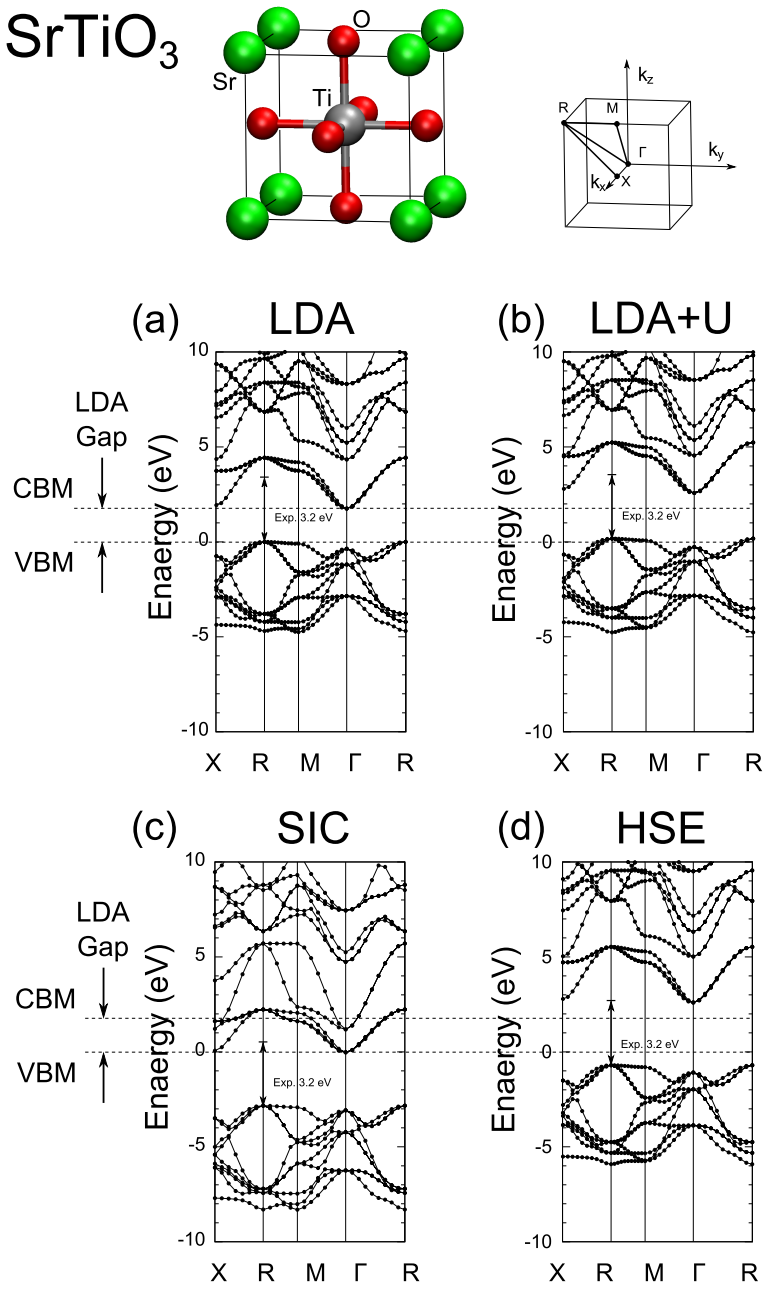

Figure 2.1: Crystal structure of $SrTiO_3$ and the series of band structures calculated with (a) LDA, (b) LDA+U, (c) pseudo SIC and (d) hybrid functional HSE along k-point path shown in the figure. In each figure, the vertical axis is the shift of eigenvalues from LDA result.

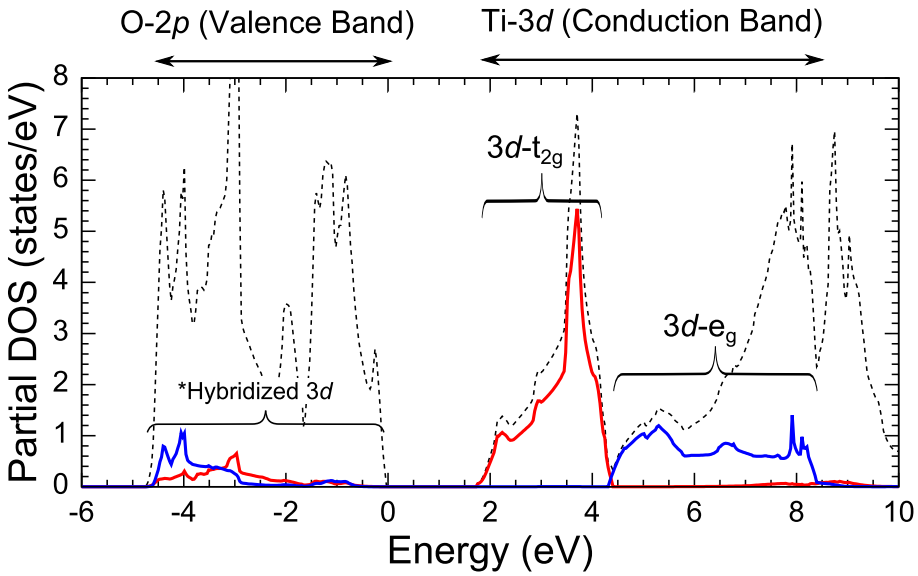

Figure 2.2: Partial density of states (PDOS) of $SrTiO_3$ calculated with LDA. Red and blue lines indicate two components of Ti-3d orbitals: t_{2g} and e_g, respectively. The Fermi level position is at $E_{\rm F} = 0$.

hybridization with occupied O-2p band. The occupation is important because it determine the improvement of the gap value in LDA+U as shown in Eq. (2.75).

Figure 2.1(b) shows the band structure of $SrTiO_3$ calculated with LDA+U. The vertical axis is the difference of the eigenvalues from LDA calculation. On-sight $+U$ correction is imposed only on Ti-3d state with $U_{\rm eff}^{{\rm Ti},d} = 5.0$ eV, which leads to the upward shift of the three bands (Ti-3d t_{2g} state) composing CBM . The change of O-2p band is very small, because no explicit correction is applied for these states. As a result, $+U$ correction brings about slight improvement of the band gap value (2.4 eV), which are still smaller than the experimental value (3.2 eV). Figure 2.3 shows the change of band gap and occupation on the Ti-3d states as a function of applied $U_{\rm eff}^{{\rm Ti},d}$, where the occupation slightly decreases ($0.08 < n_{3d,{\rm t}_{2g}}^{\rm Ti} < 0.13$, $0.24 < n_{3d,{\rm e}_g}^{\rm Ti} < 0.26$) as the increase of $U_{\rm eff}^{{\rm Ti},d}$ value. The figure also indicates that the further improvement of the band gap is difficult to be achieved with an appropriate range of $U_{\rm eff}^{{\rm Ti},d}$ that is reported to be $U_{\rm eff}^{{\rm Ti},d} = 4.0$-$5.0$ eV.

One of the serious drawbacks of the $+U$ method is the determination of the $U_{\rm eff}$ value. Theoretical approaches to obtain the $U_{\rm eff}$ value in the frameworks of DFT+U has been proposed based on several concepts, such as linear

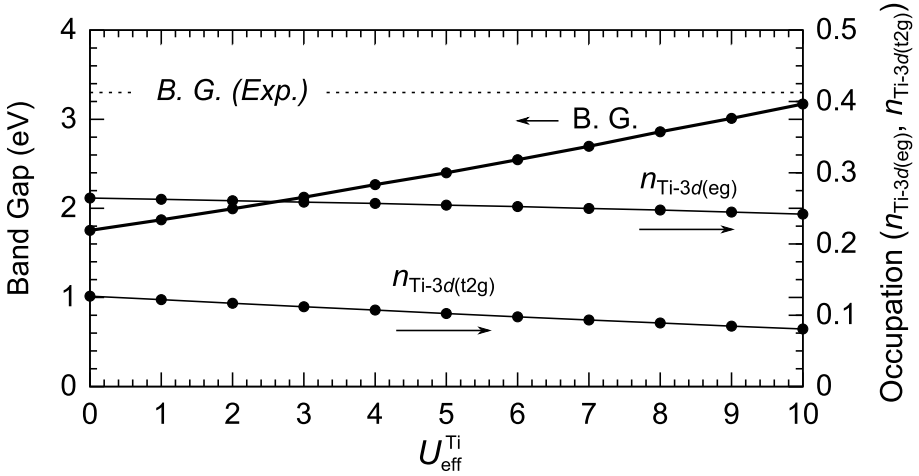

Figure 2.3: Relation between band gap of $SrTiO_3$ and occupation for Ti-3d e_g and t_{2g} states in LDA+U calculation. Dotted line shows the experimental band gap value (3.2 eV).

change of total energy for fractional occupation of a state i ($d^2E/dn_i^2 = 0$) [111, 115] or total energy difference between addition/removal of an electron into/from the atomic orbital [116]. However, manually adjusted U_{eff} value is often suitable for the calculation of actual materials compared to the theoretically obtained U_{eff} value. Moreover, there is a large dependence of U_{eff} value on the choice of the local orbital that are used for the occupancy calculation (See Eq. (2.68)); this is the local orbital dependence of LDA+U [117, 118]. For instance, the evaluated U values with neutral Fe^0 and positively ionized Fe^{2+} atomic orbitals result in 4.6 and 7.8 eV to obtain identical results [118]. In the pseudopotential framework, the un-screening procedure of the potential (removal of the valence electron from one-electron potential) leads to small dependence of the obtained band structures on the atomic valence state used for the construction of the pseudopotential. On the other hand, the atomic orbitals are directly used in LDA+U, which unavoidably introduces the strong dependence on the valence state of the isolated atomic calculations. Even though the DFT+U is a successful approach for the correction of DFT, these drawbacks hinder the application of DFT+U for more wide variety of materials.

SIC (self interaction correction)

Figure 2.1(c) shows the band structure of $SrTiO_3$ calculated with pseudo SIC [106]. The SIC band-gap value is 2.81 eV that is closer to the experi-

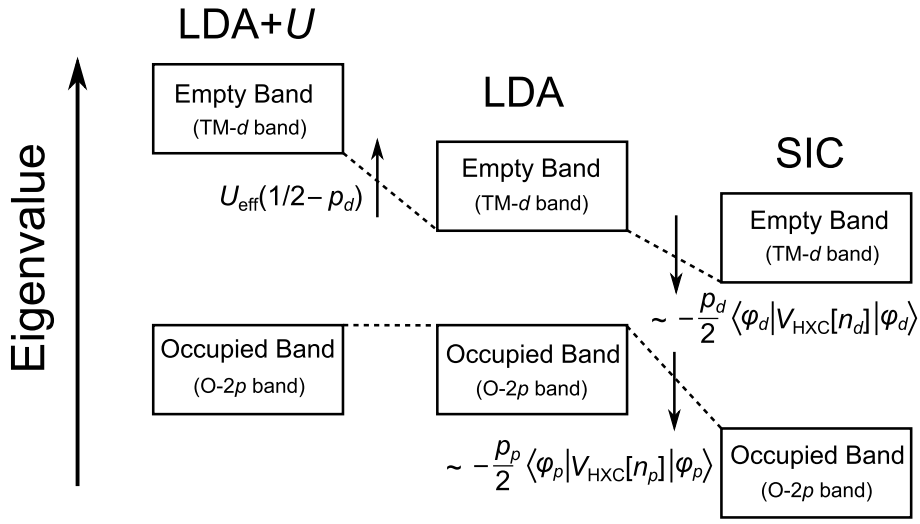

Figure 2.4: Schematic diagram of the effect of $+U$ and pseudo SIC operators on the eigenvalues of LDA band structure of $SrTiO_3$. In LDA+U, on-sight coulomb potential is applied only for the d band. The p_d and p_p is the occupations for d and p orbitals, respectively.

mental gap than the LDA+U gap. As shown in Eq. (2.59), the SIC potential is constructed based on the occupation n_i. Therefore, the pseudo SIC and $+U$ operators are similar to the point that both methods are based on the occupation, whereas their behaviors are completely different from each other. In DFT+U, i-th eigenvalue increases ($n_i < 1/2$) or decreases ($n_i > 1/2$) depending on the occupation n_i, whereas the eigenvalues in pseudo SIC always decreases as explained in Eq. (2.65). In pseudo SIC, the shift of the eigenvalue has linear dependence on the occupation (p_i) within first-order perturbation as shown in Eq. (2.65); therefore the eigenvalues of the occupied bands tend to shift more rapidly compared to the empty bands. As a result, the band gap is improved as shown in Fig. 2.1(c). Figure 2.4 summarizes the effect of $+U$ and pseudo SIC operators on the eigenvalues of LDA band structure. [5]

As stated for LDA+U, there is a similar localized orbital dependence in the pseudo SIC formalism, because both methods are basically based on the same occupation. In addition, the atomic orbital of an isolated atom that is used for the subtraction of SI in solid in pseudo SIC framework is

[5]Note that the change of the eigenvalue does not directly related to the shift of electron affinity (EA) and work functions (WF). For these physical quantities, the VBM and CBM must be evaluated from the vacuum level.

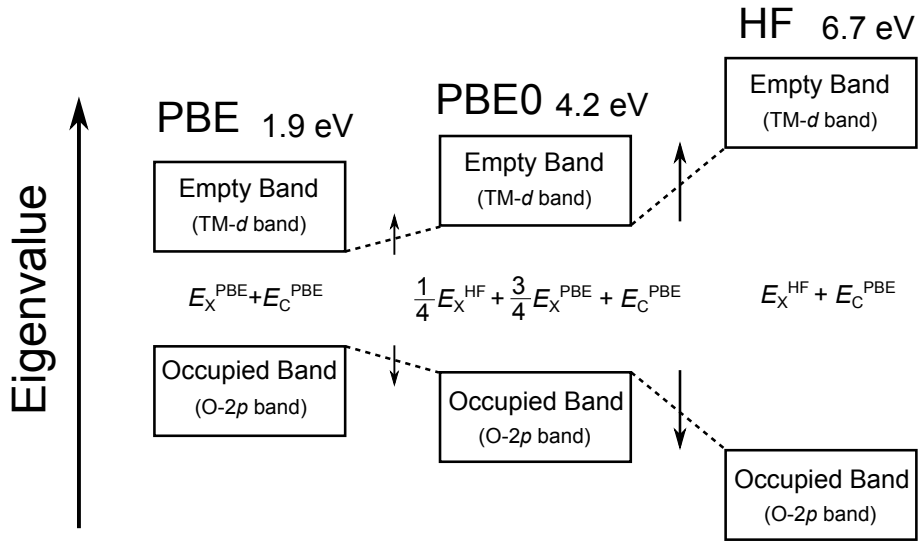

Figure 2.5: Shift of the eigenvalues and change of the band gap values calculated with GGA-PBE, PBE0 and HF for $SrTiO_3$.

an approximation for the wave function in solid and NOT the true charge distribution of itself included in the total change density. The definition of SI in solids is an important issue for the general SIC procedure, and some extension with other local orbitals such as Wanner functions [119] has been proposed. However, some problems are reported in these approaches, such as a great overestimation of the band gap probably due to the lack of proper treatment of dielectric screening [119]. The problems of the localized orbitals, as well as the definition of the SI in the solid remain as a critical issue in the SIC approaches.

Hybrid functional (HSE)

Band structure calculated with hybrid functional HSE is shown in Fig. 2.1(d). The obtained band gap value is 3.3 eV, which is very close to the experimental gap. The improvement of the band gap in the hybrid functional calculation is due to the fractional portion of the EXX (E_X^{HF}). The effects of the EXX ratio n in Eq. (2.76) are shown in Fig. 2.5, where the series of band structures and gaps calculated with different value of n (PBE, PBE0 and HF with PBE correlation) are schematically shown. In the figure, the increase of the band gap value is confirmed as the increase of EXX ratio n. Figure 2.5 (and also Fig. 2.1(d)) clearly indicates that the increase of the band gap value is brought about by the downward shift of the occupied states (valence band) and up-

ward shift of the empty states (conduction band). A general explanation for the improvement of gap value in the hybrid functional is the correction of self-interaction error (SIE) due to insufficient GGA exchange by adding a fractional portion of EXX. The downward shift of the occupied-state eigenvalues is well explained by the explanation. However, the upward shift of the empty-state eigenvalues would be difficult to be explained in terms of this explanation, because the first-order perturbation of Fock exchange potential shown in Eq. (2.82) always induces the downward shift of the eigenvalues.

For the explanation of the situation, we define three Hamiltonians. First one is an independent electron system without many-body effects, which is defined by:

$$H_{\rm KS}^0 = H_{\rm KS}^{\rm GGA} - V_{\rm XC}^{\rm GGA}, \tag{2.83}$$

where $H_{\rm KS}^0$ includes kinetic, external and Hartree potentials (without XC potential). Second and third Hamiltonians are defined by adding exchange terms of PBE and HF into $H_{\rm KS}^0$:

$$H_{\rm KS}^{\rm X,\,GGA} = H_{\rm KS}^0 + V_{\rm X}^{\rm GGA}, \tag{2.84}$$

$$H_{\rm KS}^{\rm X,\,HF} = H_{\rm KS}^{\rm EXX} = H_{\rm KS}^0 + V_{\rm X}^{\rm HF}. \tag{2.85}$$

$H_{\rm KS}^{\rm X,\,HF}$ corresponds to exact exchange (EXX) approach, where full exchange of Hartree-Fock is included. The eigenvalues calculated with these three Hamiltonians are shown in Fig. 2.6. The eigenvalues of $H_{\rm KS}^0$ show very high value compared to the original PBE-KS equations because of the strong self-interaction in Hartree term which cannot be compensated by any exchange terms. On the other hand, the GGA exchange induces almost monotonous downward shift of eigenvalues irrespective of the occupation of the states. The exchange of GGA (and LDA) does not make no distinction for the occupation, [6] which would be the cause of the monotonous shift of the eigenvalues. On the other hand, the Hartree-Fock exact exchange term explicitly considers the occupancy of states as shown in Eqs. (2.79) and (2.82), which selectively and greatly lowers the eigenvalue of the occupied state. Therefore, the upward shift of unoccupied states in the hybrid functional calculations is the simultaneous effects related to the decrease of GGA exchange and the increase of Hartree-Fock exchange rather than the direct effect of the Hartree-Fock exchange term. The contribution of GGA correlation to the gap value is about 0.3 eV, which indicate that the general tendency is governed by the ratio of the exchange terms.

[6] In LDA exchange, the monotonous shift of the eigenvalues is easily understood from the form of exchange potential in Eq. (2.18). Event though the form of GGA exchange is slightly complicated, the situation is the same because there are no explicit consideration for the occupation.

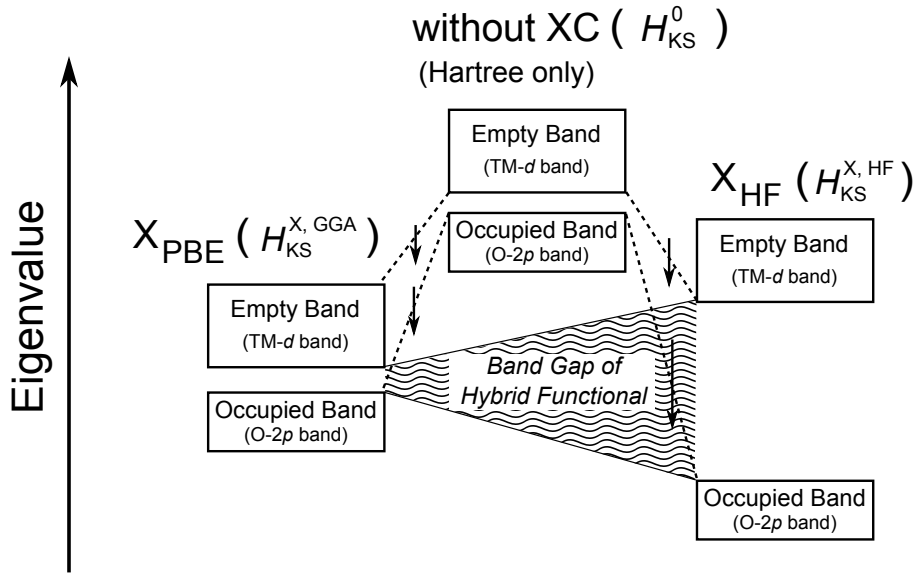

Figure 2.6: Changes in the eigenvalues of three Hamiltonians: $H^0_{\rm KS}$, $H^{\rm X,\,GGA}_{\rm KS}$ and $H^{\rm X,\,HF}_{\rm KS}$, which are defined by Eqs. (2.83)–(2.85). The shift of eigenvalues for these Hamiltonians reflect the characteristics of GGA and HF exchange terms.

2.3.2 Other band structure examples

From the discussions for the band structures of $SrTiO_3$ calculated with LDA+U, pseudo SIC and hybrid functional (PBE0), we can understand the general behavior of these three different beyond LDA functionals. In this subsection, band structures of other oxides (ZnO, TiO_2, SiO_2) and semiconductor Si are calculated to check the applicability of these improved XC functional as well as to obtain further insights on their behavior.

Band structure of ZnO

ZnO is a famous II-VI wide-gap semiconductor whose crystal structure is shown in Fig. 2.7. The behavior of oxygen vacancy and hydrogen impurity in ZnO has been widely discussed as a possible source of carrier electron which bring about the n-type conductivity. The band gap of ZnO is 3.4 eV with CBM and VBM characterized by Zn-4s and O-2p, respectively. The characteristic of the ZnO band structure is the occupied $3d^{10}$ band, whose position is below the O-2p valence band with an explicit gap between them.

The band structure calculated with LDA, LDA+U, pseudo SIC and hybrid HSE are shown in Fig. 2.7. In the LDA band structure, the band gap

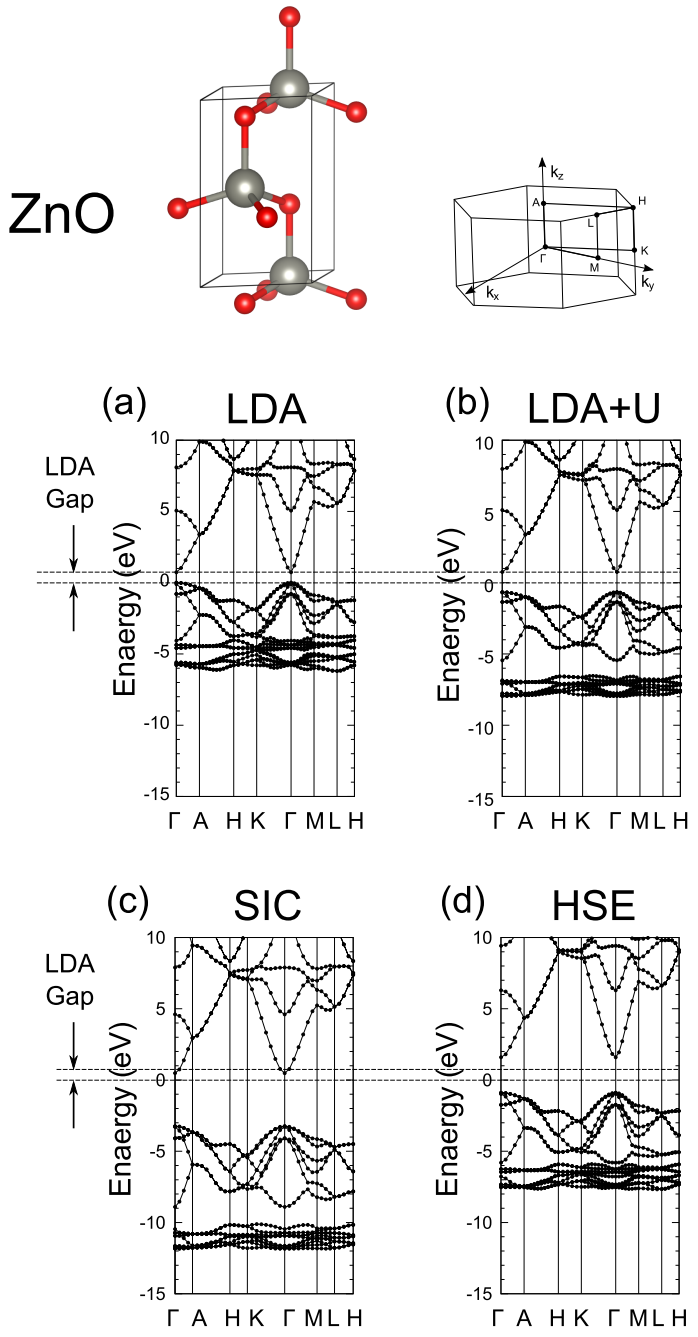

Figure 2.7: Series of band structures of ZnO calculated with (a) LDA, (b) LDA+U, (c) pseudo SIC and (d) hybrid functional HSE along k-point path shown in the figure. In LDA+U calculation, only $U_{\mathrm{eff}}^{\mathrm{Zn},3d}$ are imposed. In each figure, the vertical axis is the shift of eigenvalues from LDA result.

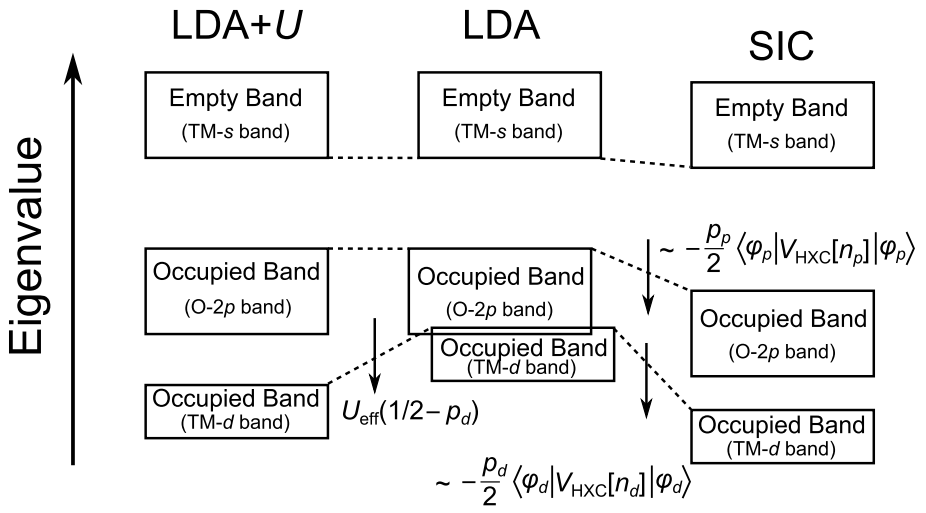

Figure 2.8: Shift of the eigenvalues and change of the band gap values of ZnO calculated with LDA, LDA+U and pseudo SIC.

(0.9 eV) is smaller than experimental value, and the Zn-3d band is within the O-2p band. On the other hand, in LDA+U with $U_{\mathrm{eff}}^{\mathrm{Zn},3d}$, the band gap is hardly improved (1.4 eV) due to the Zn-4s character of CBM, but the localized Zn-3d band shows great downward shift due to the effects of $U_{\mathrm{eff}}^{\mathrm{Zn},3d}$. In the band structure of pseudo SIC, strong downward shift of the occupied band is calculated, which leads to almost the same band gap value (3.4 eV) compared to the experimental values. On the other hand, the hybrid functional HSE gives a slightly small band gap (2.6 eV), and there are almost no gap between Zn-3d and O-2p bands. The band structure of ZnO with HSE suggests that a much more portion of EXX would be necessary to obtain consistent results with the experiment. The impact of the hybrid ratio in HSE functional on the band structure of ZnO has already been discussed by Oba *et al.* [69], where they pointed out about 37.5% instead of original 25% EXX ratio is required to obtain the consistent band gap value compared to experimental value.

Figure 2.8 schematically shows the shifts of the eigenvalues of ZnO calculated with LDA, LDA+U and pseudo SIC. The general effects of these functionals on the ZnO band structure can be explained in terms of the occupation as already explained in the band structure of $SrTiO_3$. Figure 2.9 indicates the ZnO eigenvalues calculated with GGA-PE and hybrid HSE functional, which can be understood from the already discussed general behavior of the fractional portion of EXX incorporated into GGA exchange.

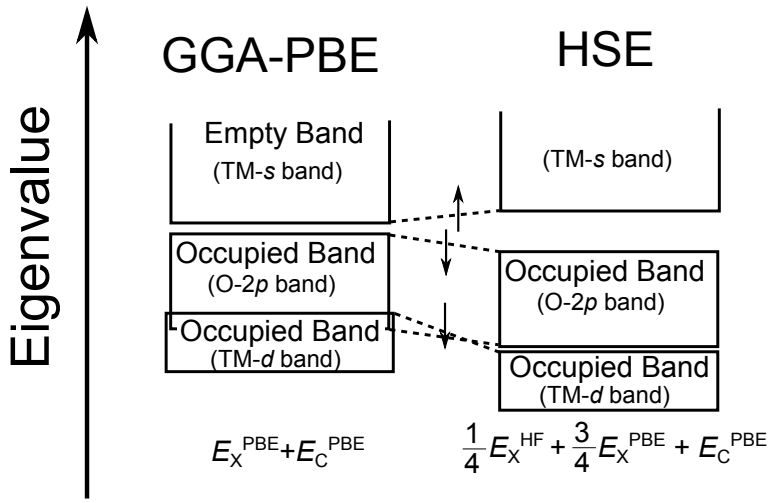

Figure 2.9: Shift of eigenvalues in the band structure of ZnO calculated with GGA-PBE and hybrid HSE functionals.

Band structure of TiO_2 rutile

TiO_2 is also an important transition metal oxide that attracts much attention for various applications due to their characteristic physical properties, such as high-k property, catalytic property and electron conductivity. Rutile TiO_2 is a wide-gap semiconductor whose band gap is 3.1 eV, and their n-type conductivity is extensively studied both from experimentally and theoretically [68]. Figure 2.10 shows the band structures calculated with LDA, LDA+U, pseudo SIC and hybrid HSE functional. The band gap value calculated with LDA (1.9 eV) is smaller than the experimental value reflecting a typical error of LDA. The band structure of TiO_2 and $SrTiO_3$ is very similar; the main character of CBM and VBM are Ti-3d and O-2p, respectively. Therefore, the effects of the improved functionals on the TiO_2 band structure are also similar to that of $SrTiO_3$ as shown in Figs. 2.4 and 2.5. In LDA+U band structure, the application of $U_{\rm eff}^{\rm Ti,3d}$ lifts up the empty Ti-3d conduction band, but the improvement of the gap value (2.4 eV) is insufficient compared to the experimental value. In pseudo SIC, large downward shifts of the occupied states bring about the improved band gap, and the value is 2.5 eV. The pseudo SIC gives a slightly better band gap than LDA+U, but the gap is still underestimated. On the other hand in hybrid functional HSE, the band gap value (3.3 eV) is slightly over estimated, but the value is closer to the

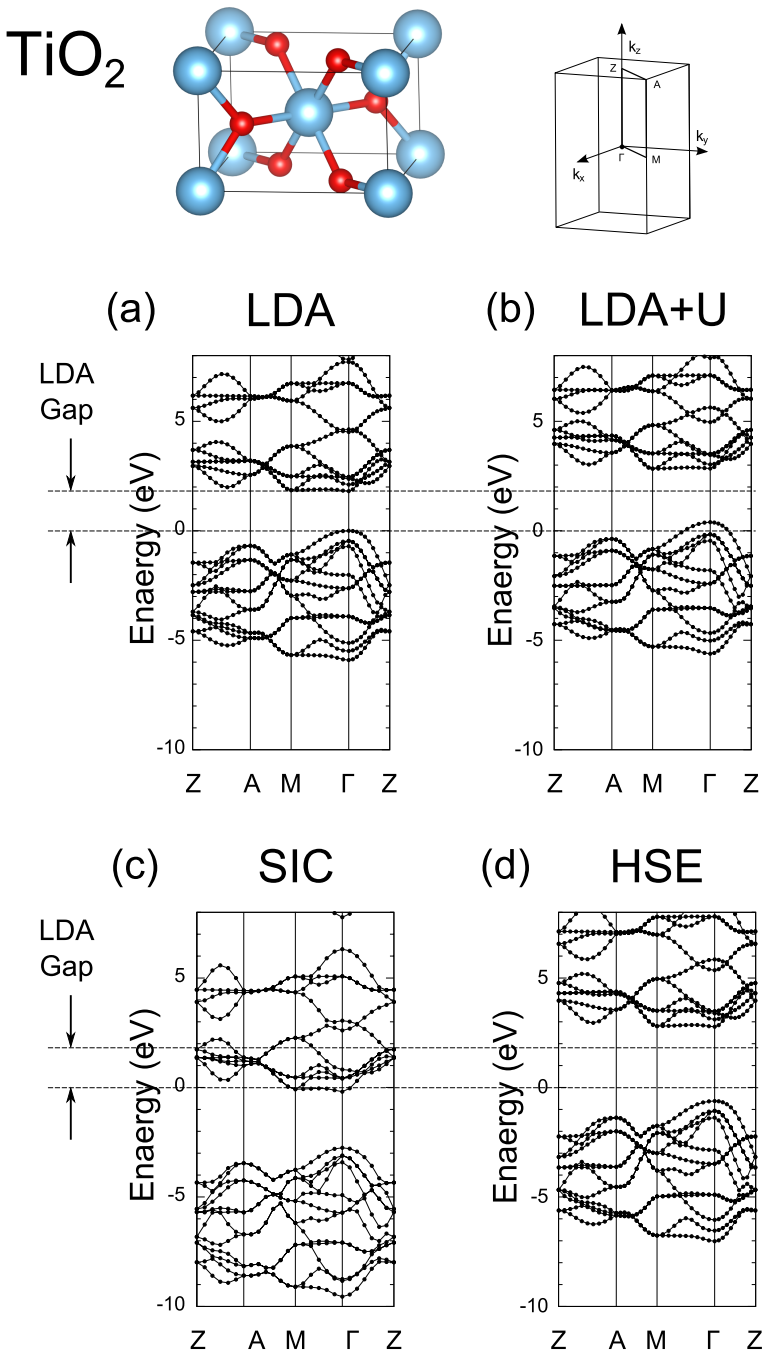

Figure 2.10: Series of band structures of TiO_2 rutile calculated with (a) LDA, (b) LDA+U, (c) pseudo SIC and (d) hybrid functional HSE along k-point path shown in the figure. In each figure, the vertical axis is the shift of eigenvalues from LDA result.

experimental value compared to other functionals.

Band structure of Si and SiO_2

The last examples are the band structures of SiO_2 alpha quartz and Si, both of which have a large impact on the modern economy as most frequently used insulator/semiconductor materials. Unlike the previous examples of transition metal oxides, the Si and SiO_2 have much more strong covalent bonding character. In these cases, the LDA+U method is not preferable for the improvement of electronic structure because this method is basically a correction for a specified band with localized atomic characters. Although the pseudo SIC is based on the occupancy of the localized orbitals, unlike the LDA+U method, all of the electronic states are corrected by the pseudo SIC operator without considering the determination of atom species and angular momentum that should be corrected; it is hence interesting to see what kind of change is induced by the pseudo-SIC method. We calculated the band structure with LDA, pseudo SIC and hybrid HSE functional, and the calculated band structures of SiO_2 alpha quartz are shown in Fig. 2.11 (a). The experimental band gap of SiO_2 quartz is 8.8 eV, whereas the LDA gap is 5.7eV. The band gap values calculated with pseudo SIC and hybrid HSE are 8.8 and 8.0 eV, respectively, which are sufficiently close to the experimental value.

The band structures of Si calculated with different functionals are shown in Fig. 2.11 (b). The experimental band gap of Si is about 1.2 eV, whereas the calculated gap with LDA is 0.5eV, which is about one half the experimental value. We found that both calculated band gap with pseudo SIC and hybrid HSE is 1.2 eV, which is just the experimental value. However, as for the band width of valence band of Si, LDA gives sufficiently close band width (12.0 eV) to the experimental value (12.5 eV), whereas pseudo SIC greatly overestimate the band width of Si (15.2 eV). Hybrid HSE also slightly overestimate the band width (13.2 eV), but the value is slightly better than the result of pseudo SIC. Considering the overall improvements for the band gap value and band width, the hybrid functional HSE would be better selection for the improvement of the band structure of Si and SiO_2.

2.3.3 Summary of the improved functionals

We have explained several band structures calculated with different XC functional: LDA (GGA), LDA+U, pseudo SIC and hybrid HSE. The obtained band gaps are summarized in Fig. 2.12. The LDA always underestimates the band gap value in wide range materials. Although the LDA+U, which is a

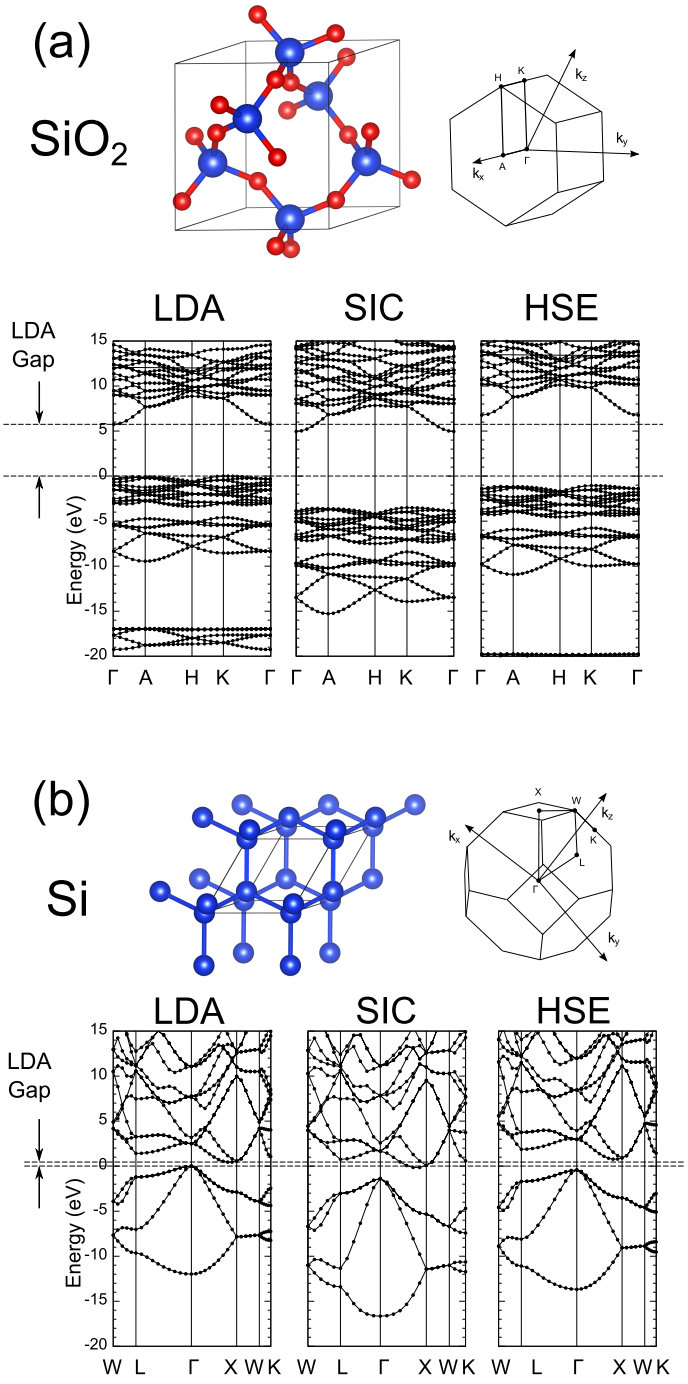

Figure 2.11: Series of band structures of (a) SiO_2 and (b) Si calculated with LDA, pseudo SIC and hybrid functional HSE along k-point path shown in the figure. In each figure, the vertical axis is the shift of eigenvalues from LDA result.

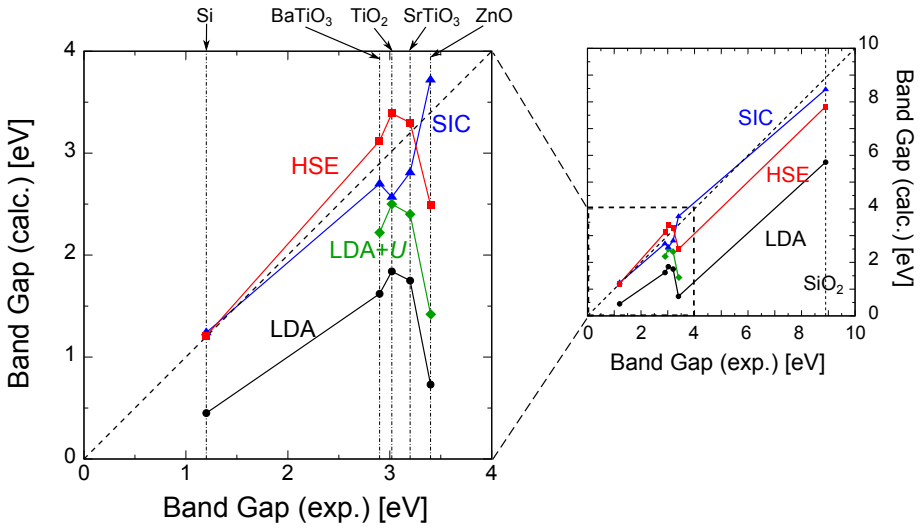

Figure 2.12: Experimental and calculated band gaps of several insulators. Calculations are performed with LDA, LDA+U, pseudo SIC and hybrid HSE. The good agreement of band gap values are achieved with SIC and HSE functionals.

frequently used beyond LDA functional, improves the LDA band structure, the improvement of the band gap values is very limited. The improvement of the LDA+U gap greatly depends on the nature of electronic structure of target material, and the appropriate choice of atom species, angular momentum and $+U_{\mathrm{eff}}$ value is particularly important. On the other hand, both pseudo SIC and hybrid HSE give greatly improved band gap values. Pseudo SIC has almost negligible increase of computational load from LDA, which makes the pseudo SIC method especially attracting for calculations with large supercell model that is necessary for the defect calculation in solid. However, the SIC-KS equation does not satisfy the variational principles, which indicate that the SIC approach in principle cannot calculate the total energy and force. This is a crucial fault of SIC method to apply the calculations of defect and impurity in perovskite-type oxides, because the relaxation around the defect species are of fundamental importance in these materials; the large effects of geometry optimization on the electronic structure of defects in perovskite-type oxides are explained in the following chapter. Therefore, we concluded that the best theoretical framework for the calculation of defects in perovskite-type oxides is hybrid (HSE) functional. Especially, the calculation of the defect and impurity in solids inevitably treat large scale supercell models, hence the HSE functional that has a more speedy conver-

gence against the k-mesh sampling number compared to PBE0 (and other hybrid approaches with non-screened EXX) is suitable to reduce the high computational cost of EXX term under plane-wave basis set. Even though the increase of the computational cost for the EXX term under plane wave basis is still a serious problem especially for a large scale calculations, the problems are gradually reducing by the recent development of the computational hardware power.

2.4 Evaluation of defect in solid

In this thesis work, we will discuss the stability of defect species in perovskite-type oxides based on formation energies. In this section, we will explain the basic procedure of the evaluation of the defect formation energy in insulators, which is necessary for the discussion in the following chapters.

2.4.1 Formation energy

Defect formation energy is basically defined by total energy difference between reactants and products, where a certain number of atoms and electrons are exchanged between host crystal and atomic and electronic reservoirs. The formation energy for a defect of atom α in charge state q can be represented by using the expression [93, 120]:

$$E^f(D^q) = \left\{E_t(D^q) - E_t(\text{perfect}^0)\right\} + \sum_i \Delta n_i \mu_i + q(\mu_{\text{VBM}} + E_{\text{F}}). \quad (2.86)$$

For the calculation with $q \neq 0$, a homogeneous background charge is introduced to prevent the divergence of coulomb energy term in a periodically-arranged charged system. In the first term of Eq. (2.86), $E_t(D^q)$ and $E_t(\text{perfect}^0)$ are the total energies of a supercell with and without defect D, respectively. The second term in Eq. (2.86) represents the exchange of atoms with the chemical reservoirs, where the notation Δn_i denotes the difference in the number of constituent atom i, and μ_i is chemical potential for the atom. For example, when we evaluate the formation energy of oxygen vacancy in an oxide material, the removal of an oxygen atom is represented by $\Delta n_1 = +1$ and an appropriate chemical potential $\mu_1 = \mu_{\text{O}}$. Under oxidizing atmosphere, a selection for the chemical potential is $\mu_{\text{O}} = \mu_{\text{O}_2(\text{molecule})}/2$. Under reducing atmosphere, such as H_2 gas, an appropriate selection is $\mu_{\text{O}} = \mu_{\text{H}_2\text{O(molecule)}} - \mu_{\text{H}_2(\text{molecule})}$. In the latter condition, the formation energy is reduced by the amount of heat of formation for water, which represents the experimental trends that the generation of the oxygen vacancy

is promoted in the reduced atmosphere. The third term in Eq. (2.86) represents the energy for the exchange of electrons (and holes) with the carrier reservoir. In defect-free perfect insulators, the Fermi energy lies within the band-gap energy region. It is, therefore, convenient to treat the Fermi energy as a parameter $0 \leq E_{\mathrm{F}} \leq E_{\mathrm{g}}$. The Fermi energy is measured from μ_{VBM} that represents the energy of electron reservoir defined at the VBM of defect-free host crystal.

An important point in Eq. (2.86) is the way of the determination of μ_{VBM} [93, 120]. The energy per electron required to remove some amount of electron from the pure host crystal is defined as:

$$\Delta E = \frac{E_H(0) - E_H(q)}{q}, \tag{2.87}$$

where q is the number of removed electrons. In insulators and semiconductors, where the highest-occupied state is at VBM, the removal of an electron leaves a hole at VBM. The energy of the VBM corresponds to that of a dilute limit for the hole, therefore one has to take:

$$\mu_{\mathrm{VBM}} = \lim_{q \to 0} \Delta E. \tag{2.88}$$

The operation equivalently correspond to increasing the supercell size to infinity with $q = 1$. The Eq. (2.88) is just the Slater-Janak theorem shown in Eq. (2.51), which indicates that the μ_{VBM} corresponds to the highest-occupied eigenvalue. Thus, in the diluted limit of Eq. (2.88), ΔE converges into the eigenvalue at VBM ($\varepsilon_{\mathrm{VBM}}$), and we can adopt $\varepsilon_{\mathrm{VBM}}$ as μ_{VBM}. [7] Figure 2.13 shows the relation between ΔE and the amount of removed electron from band-insulator $SrTiO_3$, where the asymptotic behavior of ΔE to $\varepsilon_{\mathrm{VBM}}$ is confirmed.

2.4.2 Electronic transition energy

The transition energy $\varepsilon(D, q/q')$ is defined as the Fermi energy at which the charge state of defect D transforms from q into q'. $\varepsilon(D, q/q')$ can be obtained from the relation $E^f(D^q) = E^f(D^{q'})$, which leads to the following formula:

$$\varepsilon(D, q/q') = \frac{E_t(D^q) - E_t(D^{q'})}{q' - q} - \mu_{\mathrm{VBM}}. \tag{2.89}$$

[7] It is especially noted that "NOT" all DFT program codes satisfy the Janak theorem. Therefore, the check of the converged value in Fig. 2.13 is strongly recommended before using $\varepsilon_{\mathrm{VBM}}$ as μ_{VBM}.

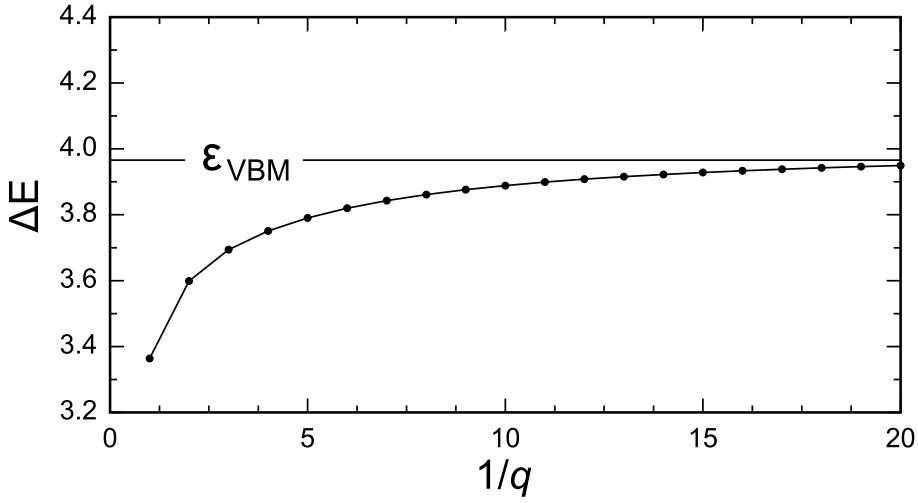

Figure 2.13: Total energy difference per hole between charge neutral- and hole (q)-contained $SrTiO_3$ unit cell. $\varepsilon_{\mathrm{VBM}}$ is the eigenvalue of VBM in $SrTiO_3$. The calculations are performed with VASP code [103].

The transition energy defined by Eq. (2.89) is closely related to the position of defect level within the band gap, where the electrons are released or captured at the in-gap states. Usually, these transition energies are consistent with the in-gap state in band structure or density of states (DOS), namely relative eigenvalues of Kohn-Sham Hamiltonian. The transition energy is based on total energy of the system; therefore the transition energy enables us the specification of the defect levels only with the total energy information.

2.4.3 Potential alignment

The charged supercell calculation violates the charge neutrality condition, which leads to the divergence of the Coulomb potential term in KS equation. Usually, the problems are solved by setting the electrostatic potential at $\mathbf{G} = 0$ component $V_{\mathrm{H}}(\mathbf{G}) = 0$ [120]. As a consequence, all eigenvalues of the KS equation have constant arbitrariness. Generally, the value of the offset constant depends on pseudopotentials and is not known [120]. The total energy that is originally derived for a charge neutral system is also subject to the same arbitrariness. Accordingly, the total energies (and the eigenvalues) obtained under charged state calculations need to be corrected to obtain consistency between neutral and charged systems for the evaluation of formation energy in Eq. (2.86). Furthermore, point defects and impurities in solids can take multiple charge states, and their stability depend on Fermi level (E_{F}),

as shown in Eqs. (2.86) and (2.89). The long-range nature of the Coulomb potential inherent in these charged defects gives rise to a constant shift in the electrostatic potentials, which affects the total energy and the band structure of the supercell. The shift cannot be evaluated supercell calculations alone since there is no absolute reference in the defect incorporated supercells.

The practical way of the correction for these arbitrariness is the potential alignment [120, 121], where electrostatic potentials are aligned between perfect neutral supercell and supercell with charged defect incorporation. The correction for the total energy of a charged defect is [120]:

$$\Delta E(D^q) = q \cdot \Delta V_{\mathbf{R}}^q = q \cdot \left[V_{\mathbf{R}}(D^q) - V_{\mathbf{R}}(\text{Perfect}) \right], \tag{2.90}$$

where $\Delta V_{\mathbf{R}}^q = [V_{\mathbf{R}}(D^q) - V_{\mathbf{R}}(\text{Perfect})]$ is the difference of the electrostatic potential at reference point $\mathbf{R}$ in the defect-incorporated and perfect supercells. The reference point $\mathbf{R}$ should be preferably selected at the point far from the defect species in supercell. Hence, the actual form of μ_{VBM} in Eq. (2.86) used for the evaluation of the formation energy is:

$$\mu_{\text{VBM}} = \mu_{\text{VBM}}^{\text{Uncorrected}} + \Delta V, \tag{2.91}$$

where $\mu_{\text{VBM}}^{\text{Uncorrected}}$ is the chemical potential of VBM without the potential alignment.

Chapter 3

Calculation of oxygen vacancy in $SrTiO_3$

As already explained in the Introduction chapter, the oxygen vacancy (V_O) in perovskite-type titanate, whose general formula is $ATiO_{3-\delta}$ is of fundamental importance, because it is easily generated in the fabrication process and gives significant impact on material properties. Previous theoretical studies indicate the significant XC functional dependence of the electronic structure of V_O in $ATiO_{3-\delta}$. However, the explanation for the reason of the great XC functional dependence is very little in these previous studies. The purpose of this chapter is the clarification of the nature of V_O in $SrTiO_{3-\delta}$ based on the results of first-principles calculation with various XC functionals. We will discuss the reason of the significant XC-functional dependence of the calculated electronic structure of V_O in $SrTiO_3$, and the possible explanation for the experimentally confirmed V_O^+ stability of the oxygen vacancy. We will also discuss the suitable XC functionals for the calculation of defects and impurities in perovskite-type oxides.

3.1 Introduction

The electronic structure calculation of defects in solids, especially shallow donor states are very challenging topic in current DFT calculation, because both band-gap value and defect levels must be properly calculated. Furthermore, the defect calculation in solids usually requires a large supercell model that contain more than ∼100 atoms depending on the concentration of the defect species, which hinders the application of high-cost and high-accuracy theoretical framework. The oxygen vacancy (V_O) in $BaTiO_3$ and $SrTiO_3$ is a typical example of a shallow donor in transition metal oxide.

As already mentioned in Introduction chapter, the V_O is of fundamental importance among the defect species in $ATiO_3$, because it is easily generated and give a great impact on various physical properties of the perovskite-type oxides. The DFT calculation with LDA- or GGA-XC functional contains several problems such as small band gap value and self-interaction error (SIE), which must be solved by more sophisticated XC functional to obtain accurate electronic structure of an isolated V_O in perovskite-type oxides. In this section, we will explain the results of DFT calculation for V_O in $SrTiO_3$ with several improved XC functional and discuss the suitable XC functional for the calculation of defects in perovskite-type oxides.

3.2 Nature of the oxygen vacancy

The nature of the oxygen vacancy (V_O) in $SrTiO_3$ can be understood from the ligand field theory for TiO_6 octahedra. As denoted in the introduction chapter, the 5-fold degenerate states of the Ti-d orbitals split into e_g and t_{2g} states due to the six ligand oxide ions as shown in Fig. 1.6. The e_g states have higher energy levels than the t_{2g} states, because the e_g states receive strong Coulomb potential from the ligand ions. Figure 3.1 shows the effect of oxygen anion removal from TiO_6 octahedra on the ligand-field splitting of Ti-3d orbitals in $SrTiO_3$. The calculations are performed with GGA-PBE exchange-correlation functional for an isolated $Sr_8TiO_6H_6$ (perfect TiO_6) and $Sr_8TiO_5H_5$ (oxygen deficient TiO_5) cluster models in a large supercell (16 Å). In the cluster models, Ti ion is surrounded by six ligand ions (OH) with Ti-O distances fixed at experimental value of cubic phase $SrTiO_3$ ($a_{\mathrm{cubic}}/2 = 3.904/2 = 1.952$ Å). Several numbers of electrons are removed from the cluster models to achieve the electron occupation similar to the bulk $SrTiO_3$; 14 electrons for $Sr_8TiO_6H_6$ and 15 electrons for $Sr_8TiO_6H_6$ are removed. Any lattice relaxations are not included in these calculations except for the O-H distance (1.001 Å).

Figure 3.1 shows the calculated Ti-3d levels, where one of the energy levels of the doubly degenerated e_g states (denoted by e'_g in Fig. 3.1) greatly decreases by the formation of V_O because of the disappearance of the strong Coulomb potential that pushes up the e_g orbital energy. The three fold degeneracy of the t_{2g} states are solved by the formation of oxygen vacancy, and two of three states (denoted t'_{2g}) show lower energy shift as shown in Fig. 3.1. However, the influence of V_O on the t_{2g} states is smaller than that on e_g states, because the t_{2g} orbitals extend avoiding the oxide anions. Consequently, the defect levels of the oxygen vacancy can be considered to be the bonding and anti-bonding states between these e'_g and t'_{2g} states, which

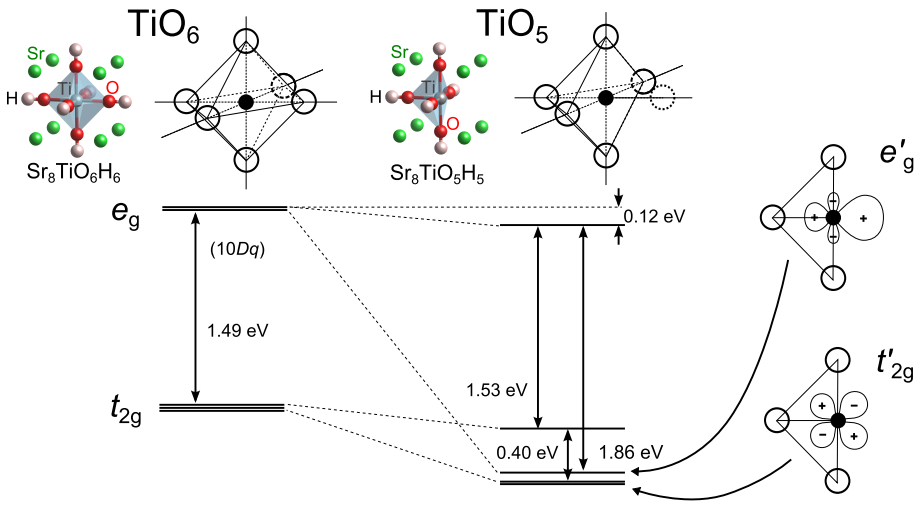

Figure 3.1: The effect of oxygen anion removal from TiO_6 octahedra on the ligand-field splitting of Ti-3d orbitals. The calculations are performed with small cluster models: $Sr_8TiO_6H_6$ and $Sr_8TiO_5H_5$. These calculations are performed with GGA-PBE exchange-correlation functional.

is schematically shown by Fig. 3.2. The figure implies that there are six isolated defect levels formed by the oxygen vacancy. The lowest defect level is the σ bonding state between two e'_g orbitals, and their anti-bonding state is the highest energy level. Four defect states are formed between the highest and lowest defect levels, which has a nature of bonding and anti-bonding of t'_{2g} states. Among these defect levels, the lowest defect level has a possibility to appear within the gap. When the lowest defect state appears within the gap, the two electrons released from the missing of O^{2-} anion are trapped at the defect state, which leads to the formation of the neutral oxygen vacancy (V_O^0). On the other hand, when the lowest defect state is very shallow or above the CBM, the oxygen vacancy becomes a donor with empty defect level (V_O^{2+}), which lead to the generation of two carrier electrons. This is a discussion for the nature of the oxygen vacancy in perovskite-type $SrTiO_3$ based on simple cluster models, and the positions of the defect states in bulk $SrTiO_3$ depend on the band width of the conduction band, band gap, etc. Furthermore, the σ bonding nature of the defects states imply strong atomic configuration dependence of the position of defect levels. In the next section, we will discuss actual V_O levels in bulk $SrTiO_3$ based on the calculations with different XC functionals.

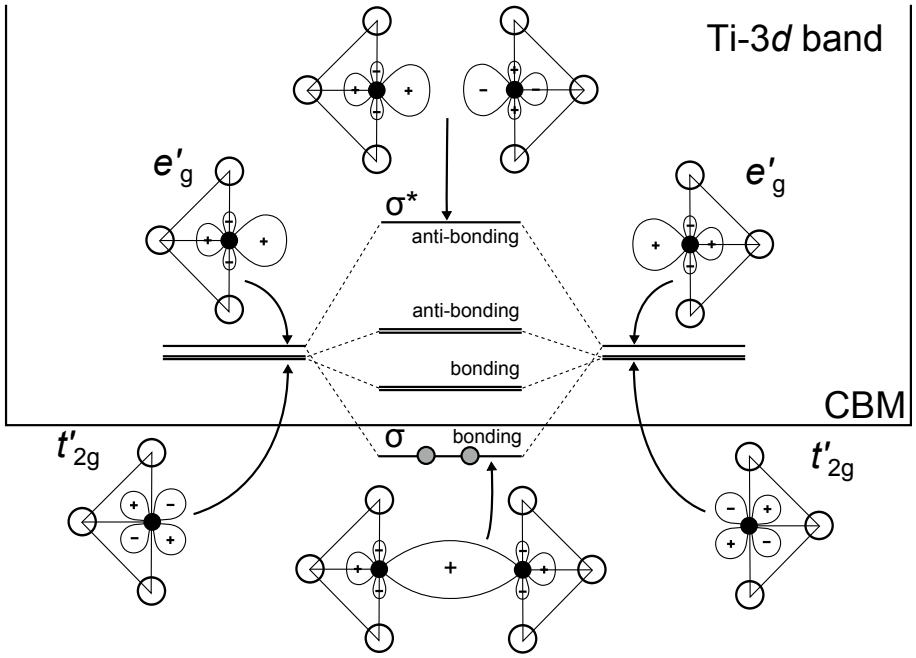

Figure 3.2: Schematic diagram of the formation of oxygen vacancy levels in $SrTiO_3$. Gray circles on the σ bonding state is trapped electrons at the defect state.

3.3 XC functional dependence of defect level

We calculated V_O levels in $SrTiO_3$ with different XC functionals. Defect calculations are performed with a supercell composed of $4 \times 4 \times 4$ $SrTiO_3$ unit cells, where two oxygen vacancies are introduced at the body center position of the supercell (318 atoms). The actual calculations are performed with the primitive cell of the defect-incorporated supercell (79 atoms). We also confirmed the effect of the lattice relaxation on the defect state of V_O in $SrTiO_3$ by using fixed-lattice supercell (any lattice relaxation does not performed) and relaxed lattice supercell (inner atomic coordinates are fully relaxed). The calculations are performed with several different XC functionals: GGA, GGA+$U_{\rm eff}^{{\rm Ti},3d}$, HSE and Hartree-Fock (HF or EXX), where the pseudo SIC calculations are not performed because the force (and the total energy) cannot be obtained with the functional as explained in Sec. 2.2.1. In HSE calculations, we employed exchange mixing ratio of 25 % HF and 75 % GGA with the value of range separation parameter $\mu = 0.207$ Å^{-1} as suggested for HSE06 functional. Calculations are performed by using projector

augmented-wave (PAW) method [1] as explained in Sec. 2.1.4. The atomic reference configuration of PAW potentials are $3s^2 3p^6 3d^2 4s^2$ for Ti, $2s^2 2p^4$ for O, $4s^2 4p^6 5s^2$ for Sr. The cutoff energy for the plane-wave basis is 500 eV.

The lowest defect levels of the oxygen vacancy calculated with various XC functionals are summarized in Fig. 3.3. The defect levels are calculated with different charge state of the supercells; neutral (with two black circles), +1 charged (with a black and white circles) and +2 charged (with two white circles) states. The spin polarization is explicitly included for +1 charged supercell with odd number of valence electron. Calculations are performed with/without the lattice relaxation. In the fixed-lattice calculations shown in Fig. 3.3, the defect states appear in all XC functionals and all carrier electrons are trapped by the in-gap states (neutral oxygen vacancy $V_{\rm O}^0$), which shows that the natures of the oxygen vacancy ($V_{\rm O}^0$) calculated with different XC functionals are almost identical in the fixed-lattice calculations. On the other hand, when the lattice relaxations are included, the defect states show upward shifts, which induces the change of the valence state of the vacancy. In GGA, GGA+U ($U_{\rm eff}^{{\rm Ti},3d} = 3$eV) and HSE, the defect level is always above the CBM, thus the two carrier electrons are generated due to the doubly charged oxygen vacancy ($V_{\rm O}^{2+}$). On the other hand, GGA+U with ($U_{\rm eff}^{{\rm Ti},3d}$ =4-5eV) and HF calculations show partial and total localization of electron at the in-gap defect state, which indicate the oxygen vacancy has a possibility to take $V_{\rm O}^{1+}$ and $V_{\rm O}^0$ states.

The large effects of the lattice relaxation around $V_{\rm O}$ on the defect level can be understood from the nature of oxygen vacancy in $SrTiO_{3-\delta}$. As shown in Fig. 3.2, the lowest defect level is the σ-bonding state between two e'_g states that extend toward the direction of the vacancy site; therefore, the distance between two Ti ions adjacent to $V_{\rm O}$ greatly modifies the overlapping of e'_g states. As a result, the energy level of the bonding state moves down when the distance between these two Ti ions decreases and moves up when the distance increases as shown in Fig. 3.4.

It would be very difficult to conclude which valence state is the true picture of the isolated $V_{\rm O}$ in $SrTiO_3$. The essential cause of the controversy is the large dependence of the defect level on the XC functional and the lattice relaxation around the vacancy. One of the measures of the validities for the calculation would be the calculated band gap value, which is very important for the evaluation of the defect-formation energy defined by Eq. (2.86). Among the XC functionals used in the present calculations, only the hybrid HSE gives the gap value sufficiently close to the experimental value. We calculated some basic properties of $SrTiO_3$, such as band gap, lattice

[1] The calculations are performed with VASP code. [103]

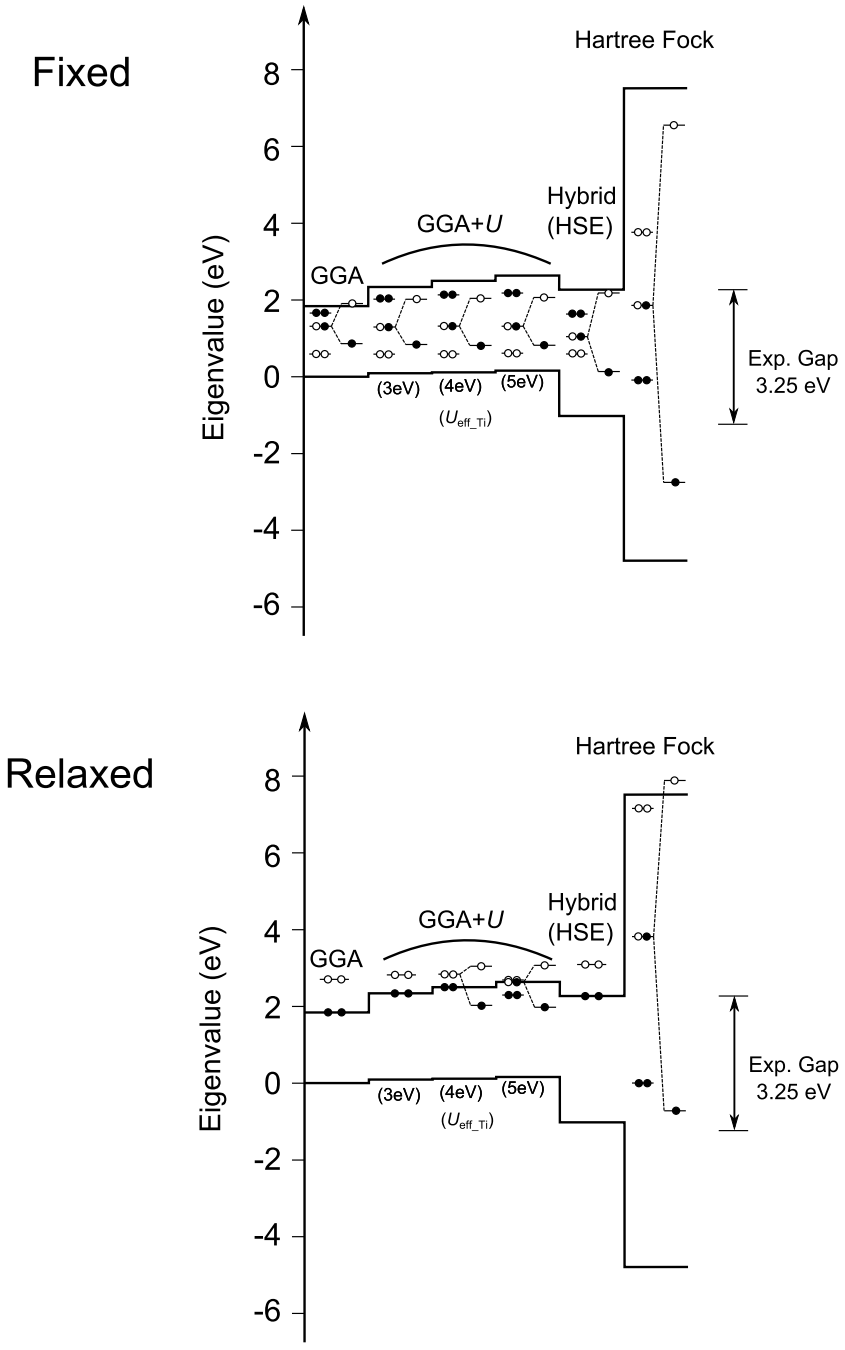

Figure 3.3: V_O levels in $SrTiO_3$ calculated with different XC functionals: GGA, GGA+U, HSE and HF. The calculations are performed with fixed (upper) and relaxed (lower) conditions. Number of electrons are changed (neutral, +1 and +2 charged states) by changing the number of electron in the supercell. Open and filled circles indicate empty and filled states, respectively.

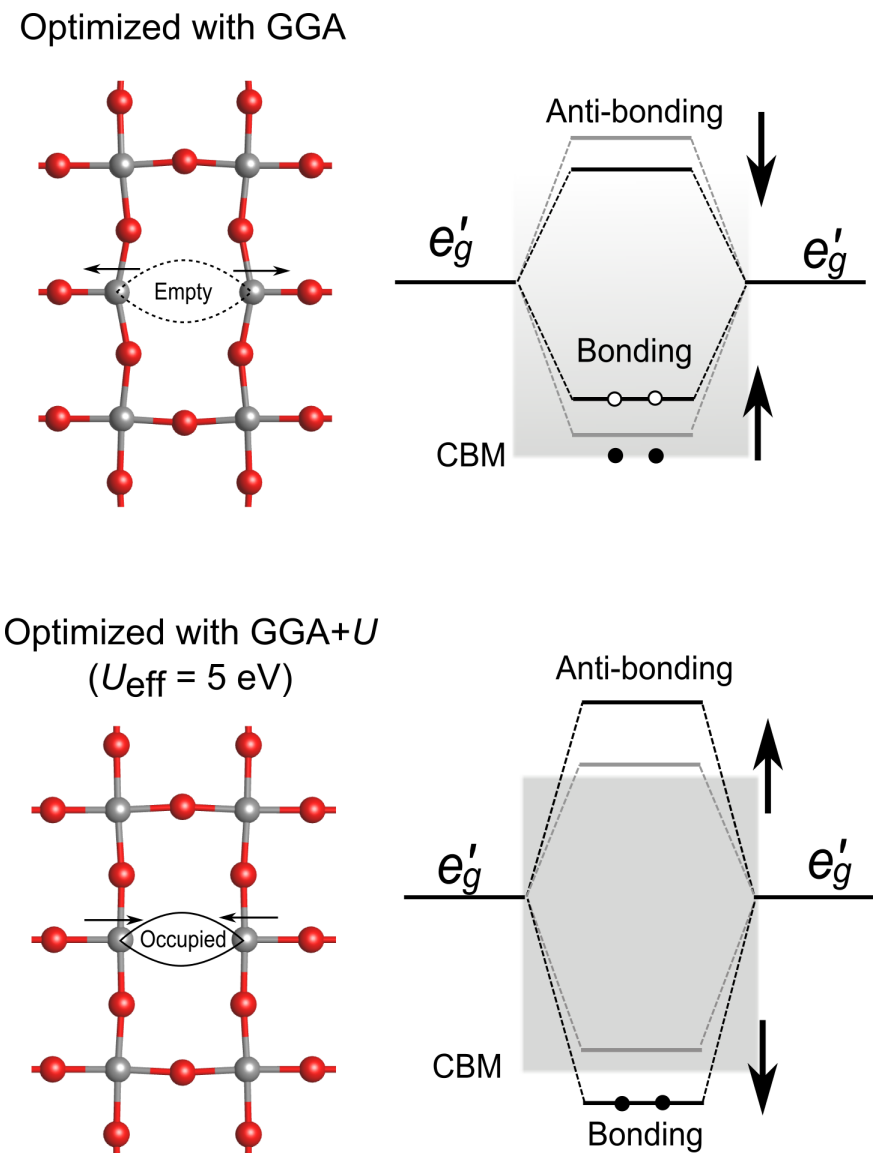

Figure 3.4: Schematic figures of the effects of neighboring Ti-Ti distance adjacent to V_{O} on the position of defect levels. The lowest defect level shows upward and downward shifts depending on the occupation of the state. These results are due to the nature of the defect level that is a bonding state of two e'_g.

constant and bulk modulus of $SrTiO_3$ unit cell with PBE and HSE, and the results are summarized in Table 3.1. The HSE functional improves not only the band gap but also the lattice constant of $SrTiO_3$ compared with PBE as shown in Table 3.1. Eventually, the HSE functional is on the verge of becoming suitable method for the calculation of defects and impurities in solids within the framework of first-principles calculation [64, 68, 69]. Hence, the results of HSE that is V_O^{2+} would be a promising candidate as a valence state of the oxygen vacancy in $SrTiO_3$. The stability of V_O^{2+} calculated with HSE is also reported for $BaTiO_3$ [64] and for TiO_2 [68]; therefore, the V_O^{2+} nature of the oxygen vacancy in $SrTiO_3$ agrees with these previous HSE calculations for the other titanates.

3.4 Formation energy

The formation energy of the V_O in $SrTiO_3$ is evaluated with GGA-PBE and HSE. Defect calculations are performed based on supercells composed of $3 \times 3 \times 3$ $SrTiO_3$ unit cells (135 atoms), and the k-point mesh is scaled down to $2 \times 2 \times 2$ according to the dimension of the supercell size. The lattice constant of the supercell is fixed at the optimized lattice of the perfect $SrTiO_3$ crystal, and the inner atomic coordinates are relaxed. The chemical potential of oxygen used for the evaluation of formation energy is $\mu_O = \mu_{H_2O(\text{molecule})} - \mu_{H_2(\text{molecule})}$, which corresponds to the hydrogen annealing condition.

Figure 3.5 shows the formation energy of V_O calculated with GGA-PBE and HSE functionals. The defect-formation energy greatly depends on the width of the band gap, because the formation energy of a charged defect linearly depends on the Fermi energy (E_F) in Eq. (2.86). Therefore, the accurate band gap value is indispensable for the proper evaluation of defect formation energy. In Fig. 3.5, the oxygen vacancy calculated with PBE and HSE always takes 2+ valence stability at any E_F region within the band gap, as indicated by the defect level shown in Fig. 3.3. The Fig. 3.5

Table 3.1: Optimized lattice constant a_0, band gap E_g and bulk modulus B for bulk $SrTiO_3$ calculated with GGA-PBE and HSE.

Functional	a_0 (Å)	E_g (eV)	B (GPa)
PBE	3.943	1.80	168
HSE	3.901	3.31	192
Experimental	3.905	3.25	179

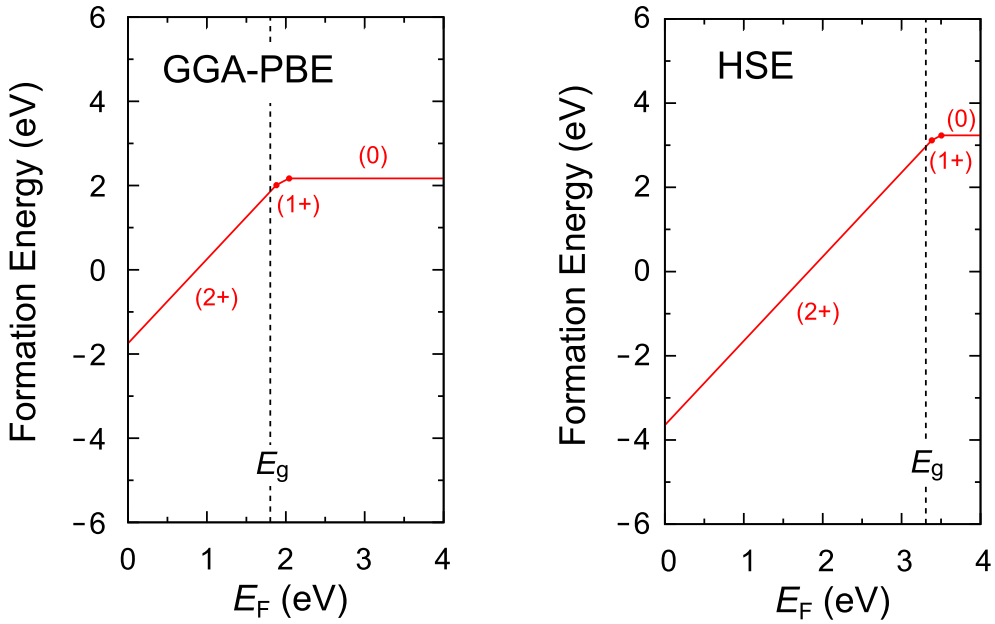

Figure 3.5: Defect formation energies of the oxygen vacancy in $SrTiO_3$ evaluated with GGA-PBE and HSE functionals. The supercell used for the calculations are composed of $3 \times 3 \times 3$ unit cells. The chemical potential of oxygen used for the calculations are $\mu_O = \mu_{H_2O(\text{molecule})} - \mu_{H_2(\text{molecule})}$, which reflects the H_2 annealing condition.

also indicates the spontaneous generation of V_O^{2+} defect species at around $E_F \sim 0$, which is suggested by the negative value of the formation energy. The results indicates the stable formation of V_O^{2+} defect species in $SrTiO_3$ under H_2 annealing experiments. The main difference between the PBE and HSE calculations is the width of the formation energies reflecting values of the calculated gaps; apparently, only the result of HSE with correct gap can be directly compared to experiments.

The formation energy indicates that the stable charge state of the oxygen vacancy is V_O^{2+}, and V_O^{+} never appears within possible E_F range. However, the result is inconsistent with previous experimental results that indicate V_O^{+} stability of isolated oxygen vacancy in $SrTiO_3$ [31,58]. This is a inconsistency already reported for the isolated oxygen vacancy in $BaTiO_3$, where the calculated V_O^{2+} stability with HSE cannot explain the experimentally confirmed V_O^{+} stability [64]. In the next chapter, we will explain that the hydrogen (H) is closely related to the apparent V_O^{+} stability of the oxygen vacancy in $ATiO_3$.

3.5 Summary

From the calculation of the oxygen vacancy in $SrTiO_3$, we have pointed out some important features that must be satisfied in the theoretical framework for the calculation of defects and impurities in perovskite-type oxides.
i) Correct band-gap value is necessary to obtain appropriate formation energy for charged-defect species.
ii) Lattice relaxation must be performed, which indicates that the force acting on each atom must be derived in the theoretical framework.
iii) Self-interaction error must be appropriately removed.
Considering these requirements, we concluded that the hybrid HSE functional would be the most preferable approach for the clarification of defects and impurities in the perovskite-type oxides. Our results of HSE calculation indicate that the V_O^{2+} is stable in $SrTiO_3$ for a wide range of Fermi level (E_F) within the gap. However, the V_O^{2+} stability is inconsistent with previous experimental results, where the valence state of the isolated oxygen vacancy are reported to be V_O^{+}. Our results indicates that the experimentally confirmed V_O^{+} stability of the oxygen vacancy is difficult to be explained by a simple picture of an isolated oxygen vacancy in $SrTiO_3$.

Chapter 4

Roles of hydrogen in perovskite-type oxides

The hydrogen in perovskite-type oxides is usually considered as proton (H^+) at an interstitial site of TiO_6 network, whereas we found that the hydrogen stably occupies oxygen-vacancy (V_O) site in $ATiO_3$ (A = Ba, Sr) [92–94]. Our remarkable finding is that the hydrogen replacing oxygen is a negatively charged hydride (H^-) [92, 93]. The hydride in $ATiO_3$ is contrary to the common belief that the hydrogen is proton (H^+) in this material group, and the existence of the H^- has not been discussed in detail so far. However, our results clearly indicate that the hydride at the oxygen site is a major defect species in $ATiO_3$ annealed under hydrogen gas [95], which can clearly explain the apparent 1+ stability of the oxygen vacancy V_O^{2+} by the stable formation of H_O^+ defect species. Our study further clarified that up to two hydride ions are weakly trapped at the oxygen-vacancy site [95], where a deep in-gap state due to the formation of $(2H)_O$ traps all free-carrier electrons and the system becomes an insulating state. Based on the results of first-principles calculation, we will discuss the diversity of hydrogen configurations and its roles in perovskite-type $ATiO_3$ oxides.

4.1 Introduction

Perovskite-type oxides are potential candidates for applications in wide variety of electrochemical applications [13]. Acceptor-doped perovskites-type oxides (ABO_3) show good proton conductivity as well as sufficient chemical and thermal stability over a wide range of chemical conditions, which are suitable for the application for solid oxide fuel cell (SOFC) [13]. The hydrogen in perovskites has been regarded as proton forming O-H bond at the inter-

stitial site of BO_6 octahedral network (H_i^+). Experimental evidence for the existence of the O-H bond is O-H stretching vibrational mode that is clearly observed at around 3,500 cm^{-1} in Raman scattering or infrared (IR) absorption spectrum experiments in $BaTiO_3$ thin films [122] and ceramics [123], and broad spectrum range of the stretching mode frequency ($2,500$-$3,500$ cm^{-1}) is observed in indium (In) doped $BaTiO_3$ ceramics ($BaIn_xZr_{1-x}O_{3-x/2}$) [124]. The first-principles calculation well describes these experimental O-H vibrational peaks [124–127], and the O-H vibrational frequencies in acceptor doped perovskites, such as $SrTiO_3$ with Sc^{3+} dopant at Ti^{4+} site [125] and $BaZrO_3$ with In^{3+} at Zr^{4+} site [124], have been extensively studied. Furthermore, the effect of Sr vacancy on the O-H vibrations has been studied from experimentally [126] and theoretically [127]. However, the interaction between the oxygen vacancy (V_O) and H has hardly been discussed, even though both V_O and H impurities are major defect species generated under H_2 annealing.

The existence of the hydrogen as proton (H_i^+) indicates that the hydrogen acts as a donor impurity that gives an electron (e^-) to the host crystal. However, several recent experimental results suggest another form of hydrogen; for example, oxygen deficient blue-black colored $SrTiO_{3-\delta}$ with metallic conductivity is transformed into transparent insulating state by annealing under H_2 containing atmosphere [59, 77]. These experimental results indicate that the hydrogen acts as an acceptor dopant that reduces the carrier electron concentration, which cannot be explained by the picture of H_i^+. Therefore, reconsideration for the role of the hydrogen in this material group is necessary to understand these experimental results.

The main purpose of this chapter is the clarification of the nature of H in $ATiO_3$ based on the results of first-principles calculation, where fundamental property of H_i and interaction between H and V_O are discussed. In section 4.2, the general property of H_i, such as electronic structure, migration barrier and vibrational property in $ATiO_3$ are explained. In section 4.3, the possibility of the replacement of O by H in perovskite-type $ATiO_3$ is explained based on the results of first-principles calculation. Contrary to the well-known picture of the H_i, we found that H is stabilized at V_O site in $ATiO_3$ [92–94]. Remarkable point in this phenomenon is that the hydrogen replacing oxygen is a negatively charged hydride (H^-), which can account for the apparent 1+ stability of the oxygen vacancy (V_O^+) by the formation of 1+ charged H_O^+ defect species. Electronic structure and stability of H_O^+ are discussed in this section. In section 4.4, the stability of multiple H at V_O site is discussed. Our calculations indicate that additional H atom can be weakly trapped by the H_O in $SrTiO_3$ [95]. The two H atoms trapped by V_O form a deep in-gap state [95] that traps all of the free carrier electrons. This phenomenon indicates that H can change the metallic $SrTiO_{3-\delta}$ single crys-

tal into completely insulating state by forming $(2H)_O$ defect complex, which can account for the previous experimental results of forming gas annealing for oxygen deficient $SrTiO_{3-\delta}$ [59,77]. We already discussed the possible way to improve the exchange-correlation functionals in Chap. 2 and explained the problems in the calculation of defects in perovskite-type oxide in Chap.3. Our conclusion is that the hybrid functional is suitable for the calculation of V_O in $SrTiO_3$; therefore the results of GGA-PBE are checked with hybrid HSE functional when the validity of GGA calculations is unclear.

4.2 Interstitial hydrogen

The hydrogen in the perovskite-type oxides is usually referred as proton at interstitial site of perovskite lattice (H_i^+); therefore, we will begin discussing the interstitial hydrogen (H_i) in $ATiO_3$. Figure 4.1 shows optimized structure of H_i in $SrTiO_3$ calculated with GGA-PBE, where the internal atomic positions are fully optimized except for the outermost fixed ions to prevent the transformation into anti ferrodistorttive (AFD) tetragonal phase shown in Fig. 1.2. The H atom is stabilized in the vicinity of an O atom in TiO_6 network, where the calculated O-H distance between H and nearest O is 1.00 Å, which is very close to the value of O-H distance of H_2O molecule (Exp. 0.957 Å, Our calc. 0.977 Å). These geometric configuration of hydrogen suggests the formation of O-H bond at the interstitial site of $SrTiO_3$.

4.2.1 Electronic structure of H_i

There are so many theoretical studies for H_i in perovskite-type oxides in terms of vibrational [124, 127] and transport [125, 128–131] property. However, detailed analysis for the electronic structure of H_i is hardly found in these previous studies. Therefore, we calculated density of states (DOS) and partial density of states (PDOS) of H_i in $SrTiO_3$ to understand the nature of the O-H bond in perovskite-type oxides. Figure 4.2 shows total DOS and PDOS calculated with the supercell model composed of $Sr_8Ti_8O_{24}H$ shown in Fig. 4.1. The PDOS of Sr, Ti, and O in Fig. 4.2 are the sum of all atomic contributions over the supercell. The valence band is composed of O-2p with small hybridization with Ti-3d. The calculated band gap value (1.85 eV) is smaller than the experimental value (3.25 eV [132]), reflecting the well-known drawback of GGA. There are two characteristic peaks around -7.2 eV (peak I) and -19.6 eV (peak II) as indicated by allows in Fig. 4.2. The PDOS of O and H indicate that these peaks are due to hybridization between H-1s and O-2s, 2p.

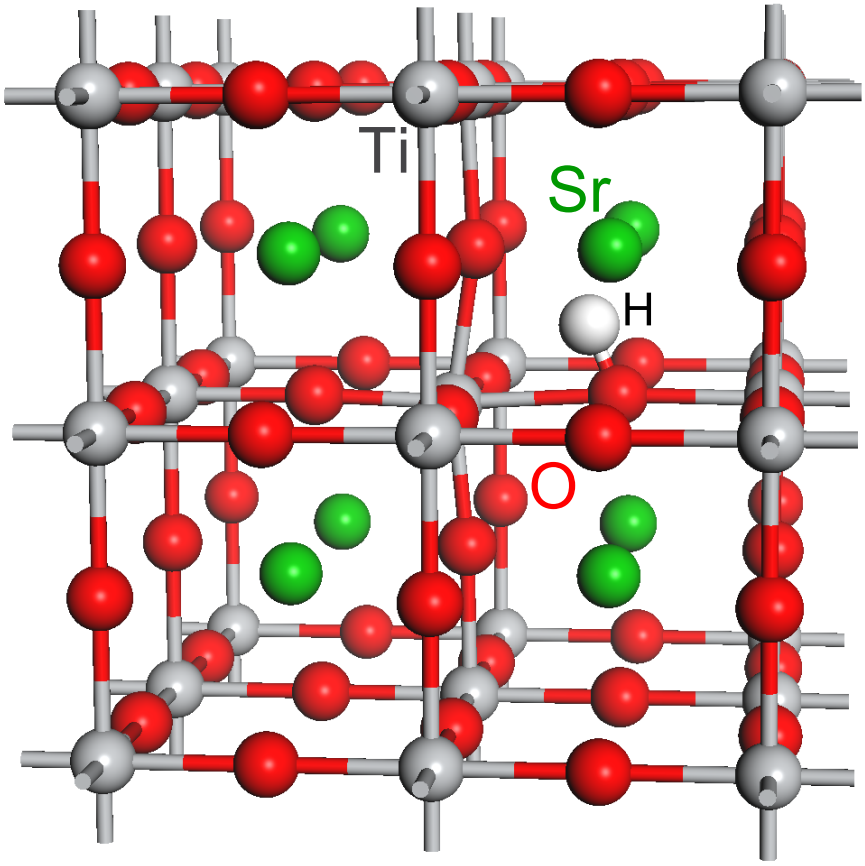

Figure 4.1: Optimized atomic configuration of hydrogen at interstitial site (H_i) in $SrTiO_3$. The supercell used for the calculation is composed of $2 \times 2 \times 2$ cubic phase $SrTiO_3$ unit cells ($Sr_8Ti_8O_{24}H$). The calculations were performed with GGA-PBE.

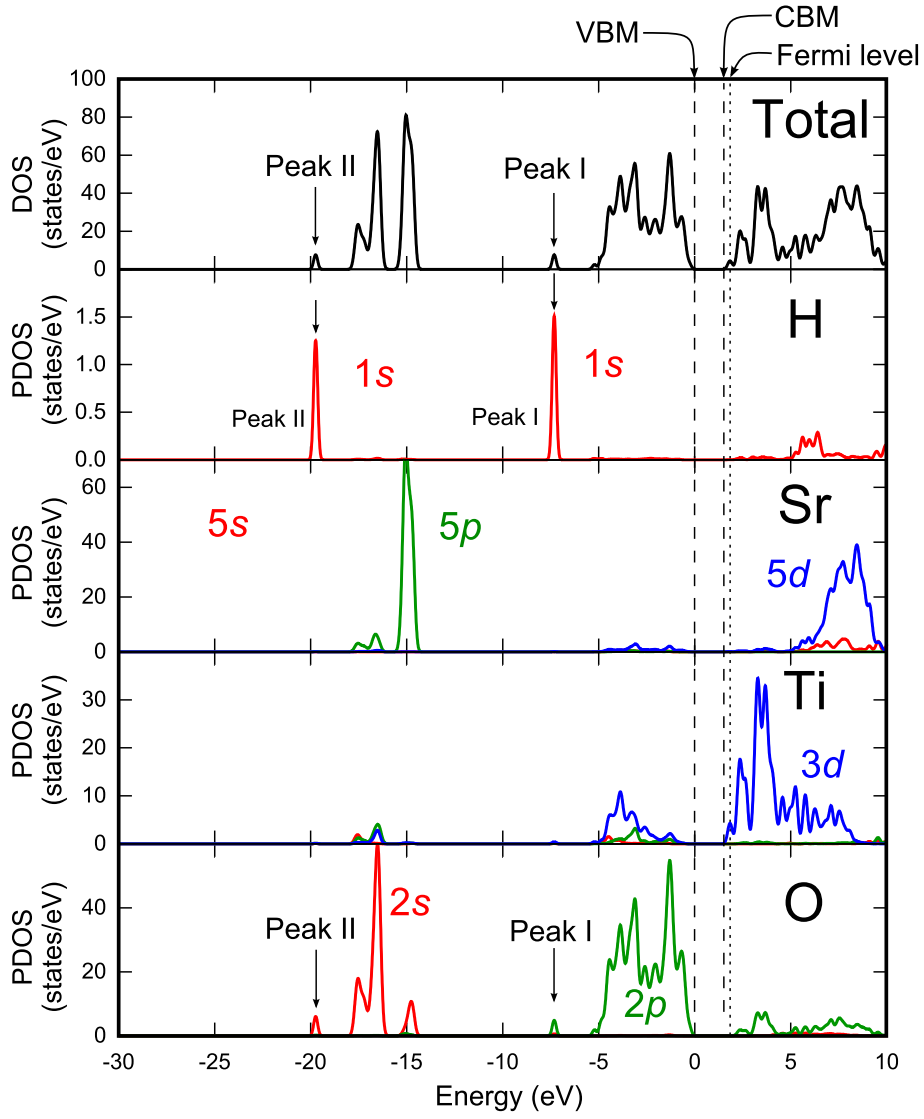

Figure 4.2: DOS and PDOS calculated for $Sr_8Ti_8O_{24}H$ supercell model shown in Fig. 4.1. The calculations are performed with GGA-PBE exchange-correlation functional. In the PDOS of H, two characteristic peaks denoted by peak I and II appear just below the O-2p and O-2s bands.

We compared the electronic structure of the O-H bond in $SrTiO_3$ with water molecule (H_2O) to confirm similarity of the OH hydroxyl group in oxide crystal and in typical molecule. The general explanation for the electronic structure of H_2O molecule is based on sp^3 hybridized orbital of oxygen atom; the sp^3 hybridization is expressed by a linear combination of one O-2s and three O-2p orbitals, and the resultant four orbitals form tetrahedral geometry. The bond angle of sp^3 hybrid orbitals is 109.5°, which are close to the experimental 105° H-O-H bond angle in water molecule. However, the sp^3 hybrid is less convenient to explain the peaks I and II that are just below O-2p and 2s bands, because the idea of sp^3 hybrid assumes the same (or close) eigenvalues for the O-2s and 2p orbitals for their starting point. Therefore, we tried to explain the electronic structure of H_2O molecule in another way based on the hybridization between H-1s and O-2s, 2p. Figure 4.3(a) shows the shift of the eigenvalues of water molecule as a function of O-H distance. At the O-H bond length more than 250 % of initial distance, there are three eigenvalues corresponding to O-2s, 2p and H-1s states of ionized O and H atoms; the O atom attracts 0.33 and the H atom loses 0.16 electrons based on Mulliken population analysis with neutral atomic orbitals. The decrease of the O-H bond length brings about the hybridization between O (2s and 2p) and H (1s) orbitals, and finally the electronic structure of a water forms at 100 % O-H bond length as shown in Fig. 4.3(a). Thus the formation of water molecule can be expressed by an energy diagram shown in Fig. 4.3(b). In the electronic structure of water, the lowest state is composed of O-2s with a weak hybridization with H-1s, and three filled states are formed by the hybridization between O-2p and H-1s states: one non-bonding state and two bonding states as shown in Fig. 4.3(b). The energy diagram of water molecule indicates that the H-1s hybridizes with both O-2s and 2p. In the PDOS of $Sr_8Ti_8O_{24}H$ shown in Fig. 4.2, Peak I and II appear just below O-2s and 2p bands, which is very similar to the State I and II in water molecule. Figure 4.4 shows the orbital shapes of the Peak I and II shown in the PDOS in Fig. 4.2. The orbital shape of the Peak I has a node just on O atom, whereas Peak II has no node. These wavefunctions are very similar to the characters of State I and II in the water molecule shown in Fig. 4.3. Therefore, the O-H bond in $SrTiO_3$ is very similar to the OH hydroxyl group of water molecule in terms of atomic and electronic structure. In $SrTiO_3$, it is especially noted that the H-1s orbital interacts not only with nearest O-2p orbital, but also with next neighboring O-2p orbital as clearly observed in the orbital shape of Peak I in Fig. 4.4. This is a clear sign of hydrogen-bond formation, which is essentially important to understand vibration and diffusion property of the interstitial H in $SrTiO_3$, which are discussed in the following section.

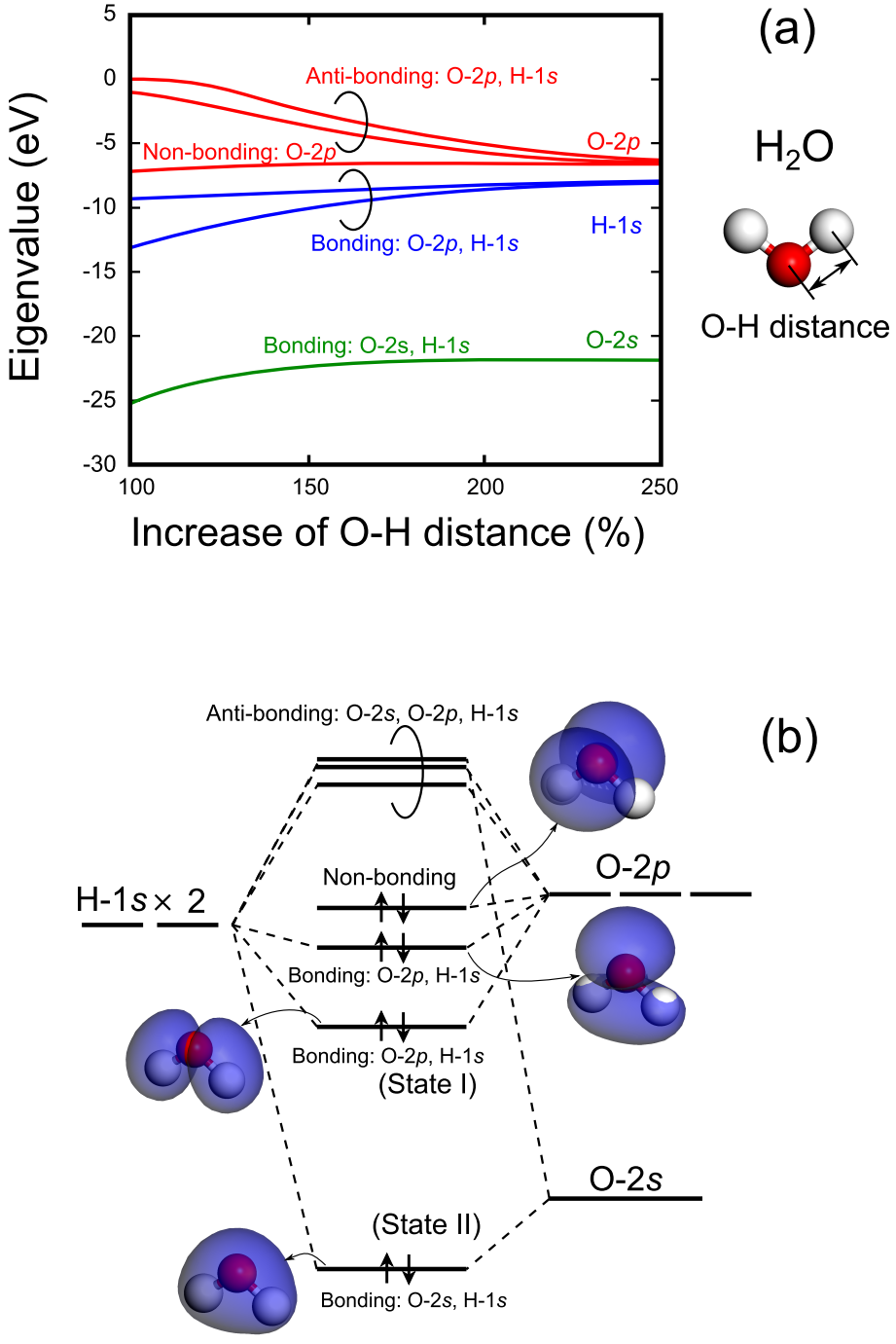

Figure 4.3: (a) Change of eigenvalues of H_2O molecule as a function of O-H distance. The O-H distance is changed from 100 to 250 % of calculated O-H distance (0.977 Å). Calculations are performed with GGA-PBE exchange-correlation functional. (b) The energy diagram of H_2O-molecule formation from O-2s, 2p and H-1s orbitals.

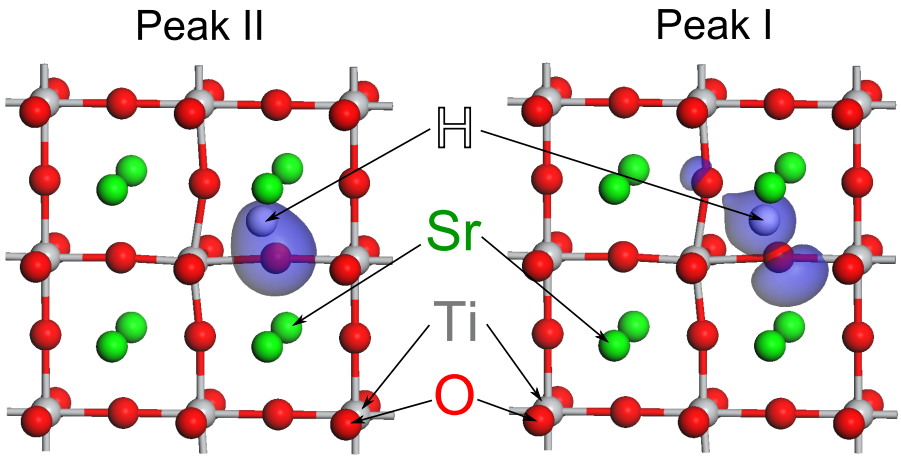

Figure 4.4: The shapes of the orbitals for the deep state due to H_i in $SrTiO_3$ denoted by Peak I and II in Fig. 4.2.

4.2.2 Diffusion process of H_i

The proton diffusion process in perovskite-type oxide is of great interest in their applications, and there have been intensive experimental and theoretical studies for this topic. In liquid water, the diffusion process of a proton occurs based on Grotthuss mechanism [133] that is proton hopping over water molecules connected with hydrogen bond network as shown in left-hand side figure in Fig. 4.5(a). The direction of the proton diffusion is changed by rotation of the O-H bond in H_2O molecule. The Grotthuss mechanism is observed in water, ice and solid acid salts ($CsHSO_4$), etc [134]. The proton diffusion in perovskite-type oxide is based on proton hopping between two oxygen atoms with breaking and formation of both O-H and hydrogen bonds during their diffusion as shown in Fig. 4.5(b). The diffusion is similar to the elementary process Grotthuss conduction; therefore, the proton diffusion in perovskite-type oxides is also refereed as Grotthuss mechanism [130, 134]. The predominant diffusion process in perovskite-type oxides occurs as a sequence of proton transfer (T) between neighboring oxygen, and rotation (R) of hydroxyl group, which is shown in Fig. 4.5 (b). The behavior of the proton migration is determined by migration-barrier height (activation energy) and frequency of the related vibrational modes.

We calculated these fundamental properties related to the proton transfer in perovskite-type $ATiO_3$. Two characteristic vibrational modes are closely related to the proton diffusion process; O-H stretching mode for T, and O-H rotational mode for R. Figure 4.6 shows the stretching vibrational mode of

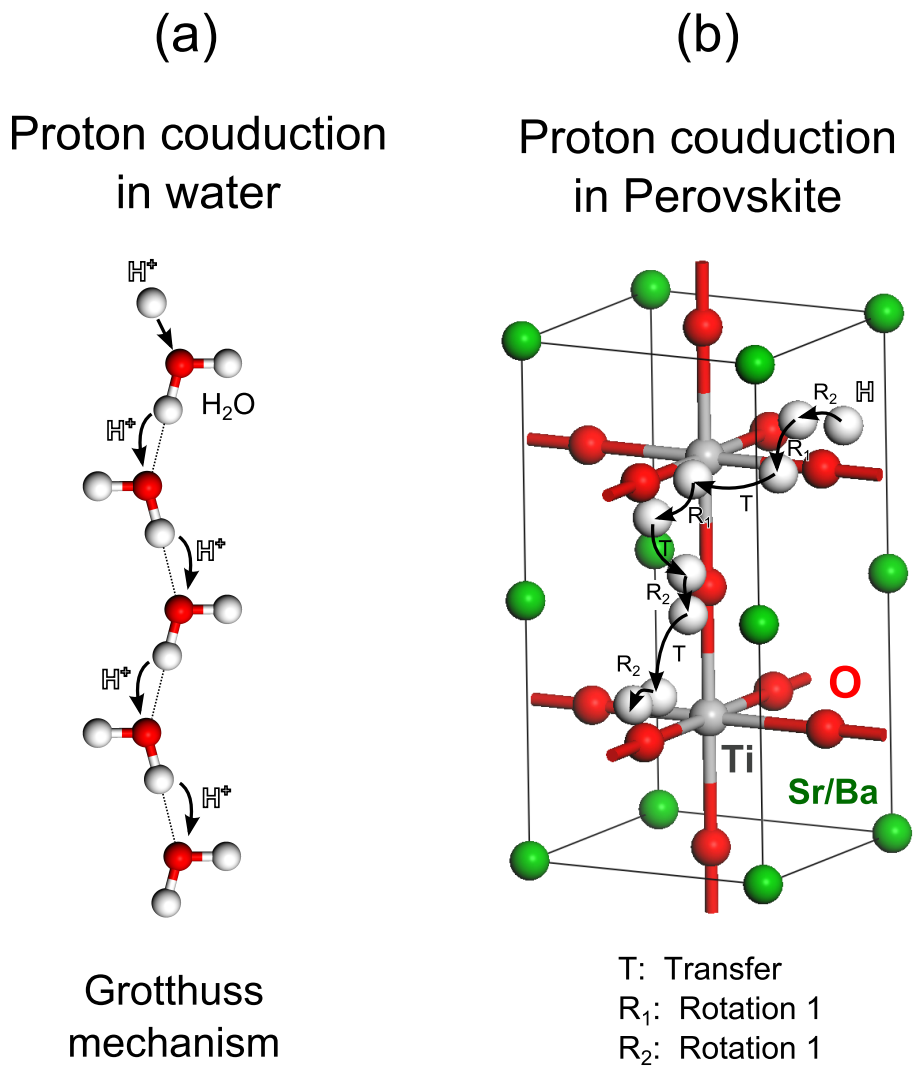

Figure 4.5: (a) Schematic figure of proton diffusion process in water, which is explained by Grotthuss mechanism. (b) Proton diffusion in perovskite-type oxide. The transfer process denoted by "T" is proton hopping between two neighboring oxygen, and "R1" and "R2" show the rotation and wag modes around the oxygen, respectively. Proton conduction in perovskites is also referred to as Grotthuss mechanism.

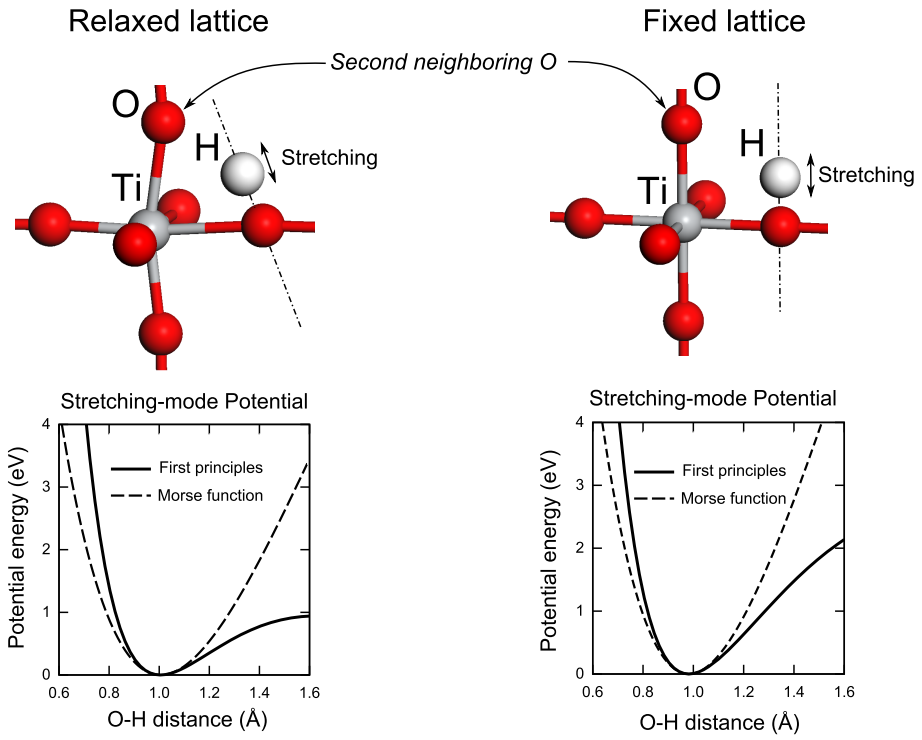

Figure 4.6: Stretching vibrational mode of OH hydroxyl group in $SrTiO_3$ and stretching-mode potential as a function of O-H distance with relaxed and fixed lattice. The calculations are performed with GGA-PBE functional.

the O-H bond and the stretching-mode potential in $SrTiO_3$. The calculations are performed with supercell models composed of $2 \times 2 \times 2$ cubic-phase $SrTiO_3$ unit cells (41 atoms) with relaxed and fixed lattices. In the fixed lattice calculation, the framework of TiO_6 octahedra and the positions of Sr atoms are fixed to the perfect $SrTiO_3$ crystal, and only the H position is allowed to locate the stable position. In the relaxed lattice calculation, atomic positions in the supercell are relaxed to achieve the most stable structure except for the outermost atoms to prevent the unexpected transition to low temperature phase of $SrTiO_3$. Main structural difference between fixed and relaxed lattices is the distance between H and second neighboring oxygen atom O_{2nd} shown by arrows in Fig. 4.6. In the relaxed lattice, the distance of O_{2nd}-H is 1.72 Å, whereas the distance becomes 2.20 Å in the fixed lattice atomic configuration. The short O_{2nd}-H distance after the geometry optimization is due to the formation of the hydrogen bond between H and O_{2nd}. We found that the geometry optimization sensitively changes

the shape of stretching mode potential, as shown in Fig. 4.6. The lattice relaxation induces the lowering of the potential barrier height around O-H distance $\sim$ 1.5 Å, which leads to the lowering of the vibrational frequency in the relaxed lattice. We evaluated the vibrational frequencies for the stretching mode within anharmonic approximation with Morse potential fitting: $U(x) = D\left(e^{-2a(x-x_0)} - 2e^{-a(x-x_0)}\right)$. The anharmonic-vibration frequency with the Morse potential is $\omega = a\sqrt{2D/m}$, where m is the reduced mass of the H atom forming the O-H bond. The results of the calculations are summarized in Table 4.1, where the table includes vibrational frequencies of O-H stretching and rotational motions for $SrTiO_3$ and $BaTiO_3$. The calculated O-H stretching vibrational frequencies with relaxed lattice are lower than the experimental value, while the fixed lattice calculations result in slightly higher frequencies compared to the experiments. Intermediate vibrational frequency between fixed and relaxed lattice is close to the experimental value, which suggests that the proton and host lattice under thermally excited states has an intermediate state between these two fixed and relaxed atomic coordinates in perovskite-type oxides.

The delicate balance between two bonding characters between oxygen and hydrogen; O-H bond (O_{1st}-H) and hydrogen bond (O_{2nd}-H) determines the atomic configuration around H_i and the shape of the stretching mode potential. In the relaxed lattice configuration, the proton transfer along the direction of O-H stretching vector easily forms a new O-H bond with 2nd neighbor oxygen due to the reduced potential barrier height. On the other hand, the proton transfer in fixed lattice does not directly form a new O-H bond yielding the steep shape of the O-H stretching potential. Therefore, not only the vibrational frequency but also the energy-barrier height for the proton transfer is expected to be greatly affected by the host lattice conditions. We further calculated the energy-barrier heights for the proton transfer and rotation processes.

Table 4.1: Vibrational frequencies (ν) of O-H stretching and rotational motion in $SrTiO_3$ and $BaTiO_3$ with fixed and relaxed lattice configurations.

	$\nu(SrTiO_3)$ (cm^{-1})		$\nu(BaTiO_3)$ (cm^{-1})		Ref.
	Relaxed	Fixed	Relaxed	Fixed	(Exp.)
Transfer	3,145	3,657	3,184	3,726	$\sim$3,500 [1]
Rotation	993	1,125	952	1,046	-

[1] Reference [122, 123]

The barrier height can be defined by total energy difference between stable atomic geometries and the geometry of transition states (TS). Several methods have been proposed to determine the energy of TS, such as nudged elastic band (NEB) [135, 136], and LST/QST [137, 138]. We evaluated the barrier heights of proton transfer and rotation processes in $SrTiO_3$ and $BaTiO_3$ by using LST/QST method implemented in CASTEP code [138]. Table 4.2 summarizes the calculated barrier heights with fixed and relaxed lattices. Our results indicate that the energy barriers greatly depend on the lattice relaxation during the proton transfer processes; the barrier heights for the proton transfer with fixed lattice are 0.78 ($SrTiO_3$)-0.90 ($BaTiO_3$) eV, whereas the lattice relaxations greatly reduce the barrier heights: 0.14 ($SrTiO_3$)-0.22($BaTiO_3$) eV. The experimentally determined barrier heights for H in perovskite oxides are 0.4-0.6 eV [11, 130, 139]; for examples, 0.41 eV for Sc-doped $SrTiO_3$ [130] and 0.43 eV for Y-doped $BaZrO_3$ [11] and 0.48 eV for Y-doped $BaCeO_3$ [130] ceramics. Apparently, the relaxed lattice calculations underestimate and the fixed lattice calculations overestimate the experimental values, which has also been confirmed in $BaZrO_3$ [128] [1].

Previous studies for $LaAlO_3$ [131] and $BaZrO_3$ [128] have clarified that the activation energies of H between two oxygen ions are closely related to the O_{1st}-O_{2nd} distances, and the dynamics of the oxygen lattice has a great impact on the proton diffusion by modulating the activation energies [130], which indicate phonon-assisted transfer of interstitial proton in perovskite-type oxides. A direct way to include the lattice dynamics is molecular dynamics (MD) simulation, and previous studies based on nonself-consistent tight-binding density functional approach [130] for H in $SrTiO_3$ gives 0.50 ± 0.22 eV. The activation energy was calculated from the simulated diffusion co-

Table 4.2: Energy-barrier heights (E_b) for transfer and rotation modes of proton in $SrTiO_3$ and $BaTiO_3$ calculated with fixed and relaxed lattice configurations.

	$E_b(SrTiO_3)$ (eV)		E_b ($BaTiO_3$) (eV)		Ref.
	Relaxed	Fixed	Relaxed	Fixed	(Exp.)
Transfer	0.14	0.78	0.22	0.90	0.4-0.6 [1]
Rotation	0.25	0.50	0.31	0.45	-

[1] Reference [11, 130, 139]

[1]Previous theoretical study for $BaZrO_3$ [128] shows 0.21 eV for relaxed- and 1.27 eV for fixed-lattice calculations (exp. 0.4 eV [11]).

efficients with different temperatures. However, due to the small number of proton-transfer events, the error can be very large in these MD simulations [130].

4.2.3 Formation energy of H_i

Both V_O and H_i are considered to be generated under hydrogen annealing process. However, it is very ambiguous which defect species is dominant in these experiments. Therefore, we evaluated the formation energy of the H_i based on Eq.(2.86) in Sec. 2.4.1, and the results are compared with the formation energy of V_O. As explained in Sec. 2.3.1, the band gap value calculated with GGA is greatly underestimated; therefore, we compared the results obtained with GGA-PBE and HSE. Figure 4.7 shows the formation energies of H_i (solid lines) calculated with (b) GGA-PBE and (c) HSE. The dotted lines in the figures are the formation energy of the oxygen vacancy. The stable valence state of H_i is 1+ at any E_F position within the band gap (E_g). At around $E_F \sim 0$, the stable defect species is V_O^{2+}, while H_i^+ becomes the stable defect at around $E_F \sim E_g$. The crossover of the stable defect species from V_O^{2+} to H_i^+ occurs at $E_F = E_1^{HSE} = 1.70$ eV ($E_1^{PBE} = 0.68$ eV). The results indicate that the stable defect species under hydrogen annealing greatly depends on the Fermi level; the stable defect species in the range of $0 < E_F < E_1$ is V_O^{2+}, whereas H_i^+ tale places the main defect species in $E_1 < E_F < E_g$.

4.3 Exchange of Oxygen by Hydrogen

Even though the effects of acceptor dopings on the vibration frequency and activation energy have been extensively studied, the effect of V_O has hardly been studied yet. The effect of V_O on the nature of H in perovskite-type oxides is of great importance because both V_O and H_i are typical defect species generated under hydrogen annealing.

4.3.1 Diffusion of hydrogen into oxygen-vacancy

During the study of the proton migration around the oxygen vacancy, we found that the H_i easily migrates into V_O site in $SrTiO_3$ and $BaTiO_3$ [93, 95]. Interestingly, the migration of H_i into V_O occurs only with free-carrier electrons, and the removal of the electron hinders the migration of H_i into V_O site. Figure 4.8(a) shows the supercell model and two diffusion paths (C4-C1 and C7-C1) examined in our study. The supercell models are composed of

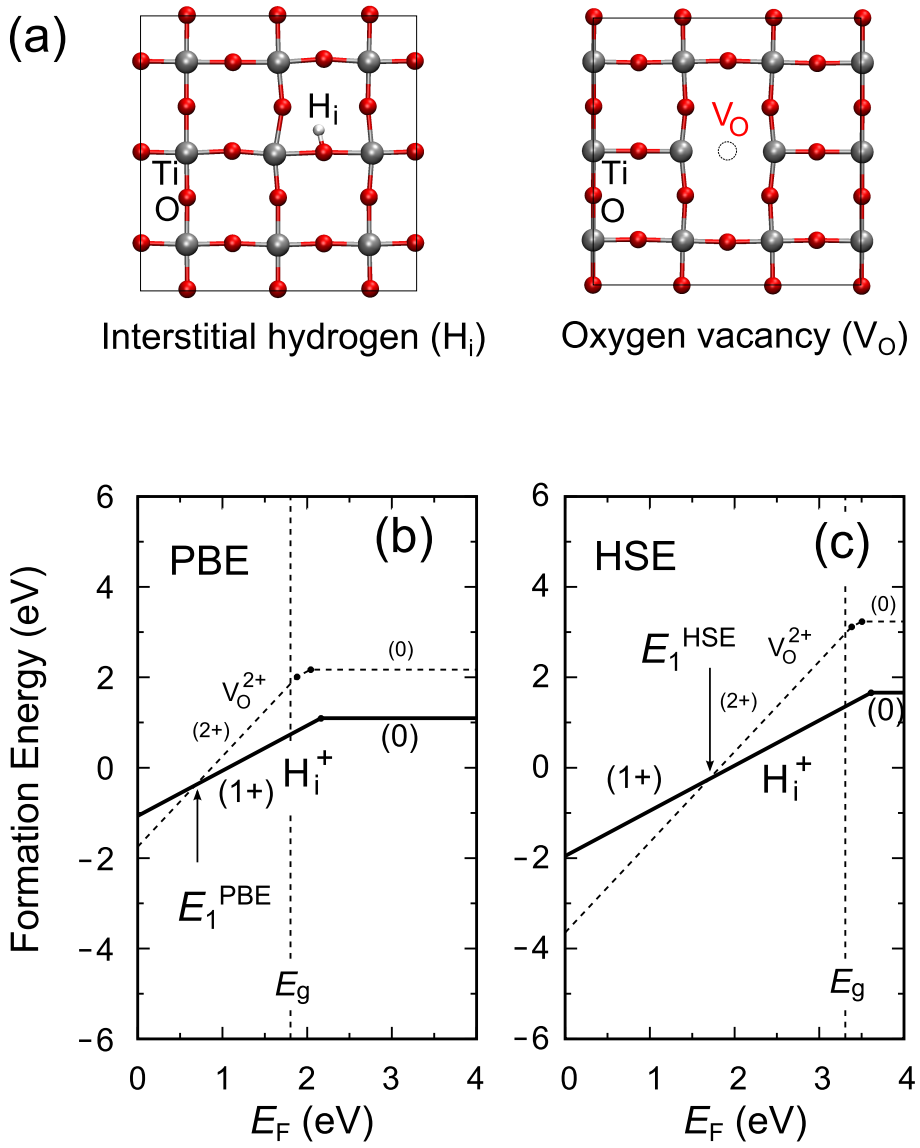

Figure 4.7: (a) Schematic figures of interstitial hydrogen (H_i) and oxygen vacancy (V_O) in $SrTiO_3$. Formation energies of H_i calculated with (b) PBE and (c) HSE are shown by solid lines. The formation energies of oxygen vacancy (V_O) are simultaneously shown by dotted lines in each figure.

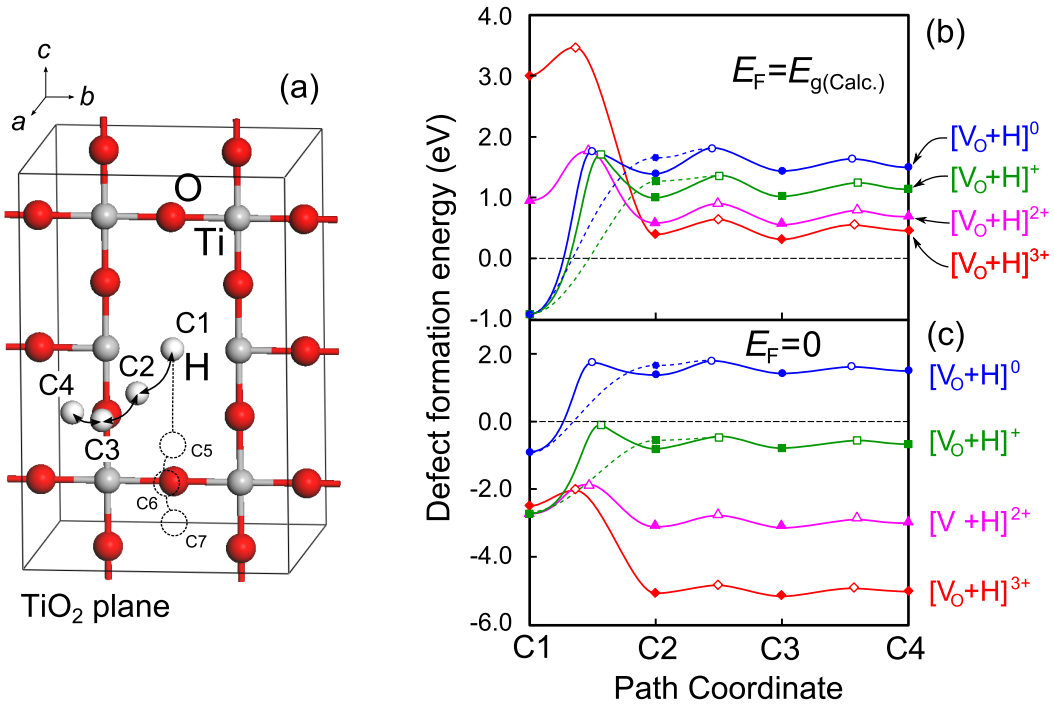

Figure 4.8: (a) Diffusion paths of H from an interstitial site (C4) to a V_{O} site (C1) in $SrTiO_3$, where only a TiO_2 plane is depicted. Defect formation energies of H in $SrTiO_3$ along the diffusion path (C4-C1) with different Fermi energies; (b) $E_{\mathrm{F}} = E_{\mathrm{g}}$ and (c) $E_{\mathrm{F}} = 0$. Note that there are metastable states around C2 position in charge neutral and 1+ charged supercells, and the diffusion barrier heights are greatly reduced via the metastable state as shown in dotted lines in Figs. (b) and (c).

$2 \times 2 \times 3$ unit cells of $SrTiO_3$ ($Sr_{12}Ti_{12}O_{35}H$) and $BaTiO_3$ ($Ba_{12}Ti_{12}O_{35}H$). Diffusion barrier heights for two different diffusion paths (C4-C1 and C7-C1) were evaluated with fully relaxed internal atomic coordinates. In $BaTiO_3$, the migration barrier height from C2 to C1 is very small (~ 0.02 eV) compared to that from C5 to C1 (1.4 eV); therefore, the C1-C4 path is preferable for the H diffusion into V_O site in $BaTiO_3$. In $SrTiO_3$, the diffusion barrier height from C2 to C1 (0.36 eV in charge neutral state) is also smaller than that from C5 to C1 (0.52 eV in charge neutral state), which indicates the C1-C4 path is also preferable for $SrTiO_3$.

Figure 4.8 (b) and (c) show series of defect formation energies of H in the $Sr_{12}Ti_{12}O_{35}H$ supercell along C1-C4 path, where the stable and transition states are plotted with filled and open marks, respectively. We confirmed almost the same behaviors for $Ba_{12}Ti_{12}O_{35}H$ supercell [93]. The defect formation energies in Fig. 4.8 are calculated according to Eq. (2.86), where a half of the total energy of H_2 molecule is used for the chemical potential of hydrogen: $\mu_H = E(H_2)/2$. The difference between Fig. 4.8(b) and (c) is the value of Fermi level (E_F) in Eq. (2.86), where (b) $E_F = E_g$ and (c) $E_F = 0$ are selected for each figure, respectively. From C4 to C2 positions, the H is always positively charged proton (H^+) and oxygen vacancy is always doubly charged (V_O^{2+}) defect species; therefore the 3+ charged supercell denoted by $[V_O{+}H]^{3+}$ is the most stable charged state. In Fig. 4.8(b) with $E_F = E_g$, the stable charge state changes from +3 into +1 between C2 and C1 positions, and the +1 charged state denoted by $[V_O{+}H]^+$ becomes the most stable state around C1 position. The reaction energy of H at the V_O site, which is defined by the total energy difference between the lowest energy at the C2 and C1 positions is about 1.4 eV; therefore H is stably trapped by V_O in $SrTiO_3$ with $E_F = E_g$. On the other hand, in Fig. 4.8(c) with $E_F = 0$, the system becomes unstable by 2.5 eV due to the migration of H into V_O site, which indicates that the H does not move into V_O when the n-type carriers from V_O^{2+} and H^+ are completely compensated. These results are consistent with previous first-principles MD calculations for proton diffusion in acceptor (Sc) and oxygen vacancy (V_O^{2+}) simultaneously doped $SrTiO_3$ performed by Shimojo *et al.* [125], where a proton diffuses around the edge of the V_O and will not move into the vacancy site. In the MD calculations, acceptor dopant (Sc^{3+} replacing the Ti^{4+}) eliminates free carrier electrons, which hinders the migration of H_i into V_O site as shown in Fig. 4.8(c).

A remarkable point in these calculations is the valence state of the hydrogen during the migration process into the V_O site; the $[V_O{+}H]^{3+}$ stability at C2-C4 indicates the stable formation of V_O^{2+} and H_i^+, whereas the $[V_O{+}H]^+$ cannot be explained with the stable charge state of the isolated defects. Eventually, the hydrogen at the oxygen vacancy site is a negatively charged

hydride (H^-), which indicates that the hydrogen changes its character from H^+ to H^- absorbing two free-carrier electrons during the migration process into the V_O site.

4.3.2 Charge density difference

The H^+ and H^- characters of H can be directly confirmed by calculating charge density difference [93]: $\Delta\rho = \rho[\text{host + H}] - \rho[\text{host}] - \rho[\text{H atom}]$, where ρ[host], ρ[H atom] and ρ[host + H] are charge densities of $SrTiO_3$ host crystal, isolated H and host crystal with H incorporation, respectively. We used $4\times4\times4$ $SrTiO_3$ supercell as a host crystal (320 atom) for these analysis. Calculations are performed with GGA-PBE exchange correlation with Γ-point only k-point sampling. The calculated charge density differences $\Delta\rho$ for H_i and H_O are shown in Fig. 4.9(a) and (b), respectively. In Fig. 4.9(a), the charges are strongly perturbed around the intercalated H_i, and increase of charge density of d (t_{2g}) orbital shape on Ti atoms far from H_i is clearly observed. The increased charge density is the character of CBM of $SrTiO_3$, which indicates the released carrier electron from H_i widely spread on the CBM in the whole supercell. On the other hand, in Fig 4.9(b), the charge density far from the incorporated H_O clearly decreases with the same character, which indicates that the number of free carrier electron released from V_O^{2+} is reduced by the incorporation of H_O. The electrons gathered by H_O form spherical charge density whose radius is about 1.2 Å. The radius of the electron cloud is very close to the ionic radii of hydride (1.5 Å), which indicates the formation of hydride (H^-) at V_O site. These results indicate that the hydrogen can act as both donor/acceptor behavior depending on its position in $SrTiO_{3-\delta}$. The hydrogen has been considered to be proton in perovskite-type oxides, but our results clearly indicate that the negatively charged hydride (H^-) is also a stable species in the oxygen deficient $SrTiO_{3-\delta}$ and $BaTiO_{3-\delta}$ [93, 95].

4.3.3 Formation energy of H_O

The formation energies of H calculated with GGA-PBE shown in Fig. 4.8 suggest that H stably occupies V_O site in oxygen deficient $ATiO_{3-\delta}$. The main drawback of GGA-PBE is the underestimation of band gap value, which disturbs accurate response of the formation energy to the extra charges. Therefore, we evaluated the formation energy of H_O in $SrTiO_3$ with hybrid HSE that correctly reproduces the band gap value, and compare the obtained results to the GGA-PBE results. The optimized structures of the H_O in $SrTiO_3$ with PBE and HSE are shown in Fig. 4.10(a) and (b), respectively.

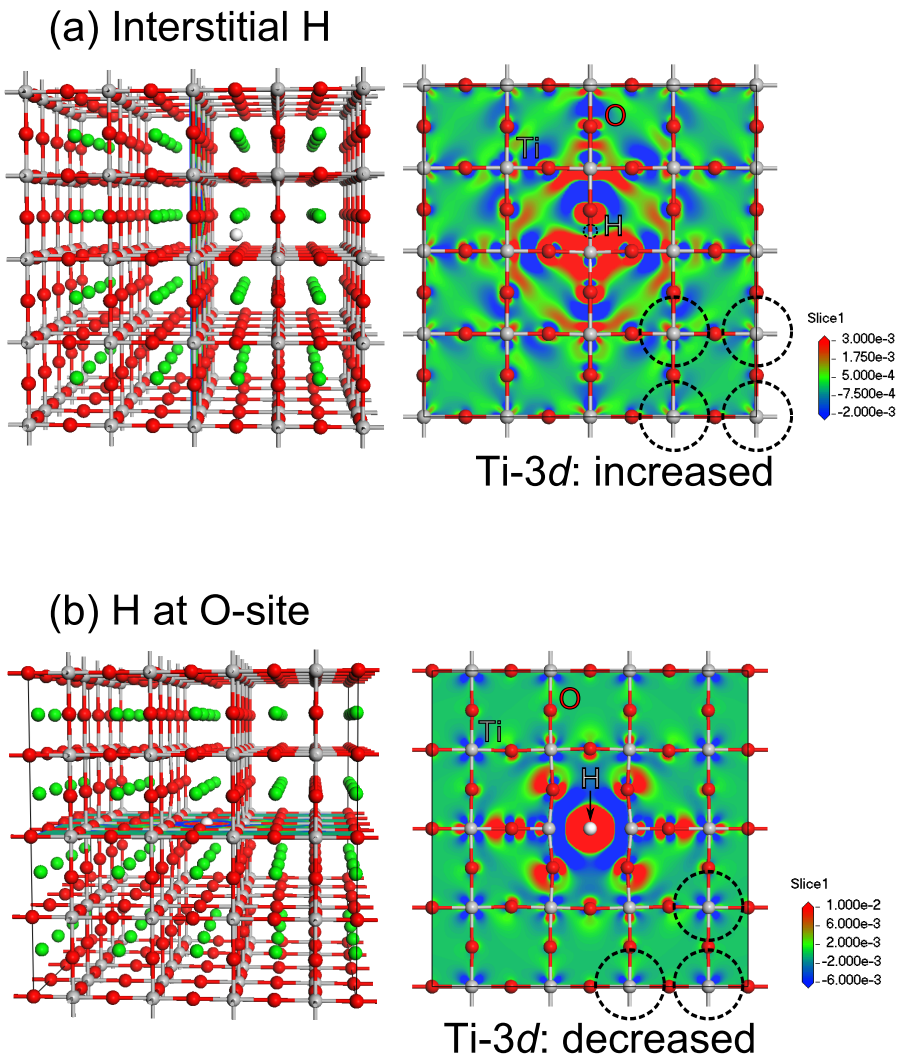

Figure 4.9: Charge-density differences due to H intercalation in $SrTiO_3$. (a) Intercalation of H at interstitial site in perfect $Sr_{64}Ti_{64}O_{192}$ supercell and (b) H intercalation at the center of V_O site in $Sr_{64}Ti_{64}O_{191}$ supercell. The red and blue areas indicate increases and decreases in charge density before after the H incorporation, respectively.

We found that the overall nature of the optimized structures with GGA-PBE and HSE are almost the same; H is stabilized at the center of the V_{O} site in both functionals. Compared to the Ti-V_{O}-Ti distances in V_{O} incorporated $SrTiO_{3-\delta}$ (the distances are 4.20 and 4.21 Å for HSE and PBE, respectively), the distance of Ti-H_{O}-Ti (4.01 and 4.09 Å for HSE and PBE, respectively) becomes smaller due to the formation of H_{O}.

Defect formation energies are evaluated according to Eq. (2.86). Here, we recall the formula:

$$E^f(D^q) = E_t(D^q) - E_t(\mathrm{host}^0) + \sum_i \Delta n_i \mu_i + q(\mu_{\mathrm{VBM}} + E_{\mathrm{F}}), \qquad (4.1)$$

The detailed explanations for the notations are given in section 2.4.1. In the present calculations, the chemical potentials μ_i are selected so as to satisfy the hydrogen annealing conditions; that is, $\mu_{\mathrm{H}} = \mu_{\mathrm{H_2(molecule)}}/2$, $\mu_{\mathrm{O}} = \mu_{\mathrm{H_2O(gas)}} - \mu_{\mathrm{H_2(molecule)}}$. We evaluated the $E^f(\mathrm{H_O})$ in two manners: $E^f(\mathrm{H_O})_{\mathrm{Perfect}}$ and $E^f(\mathrm{H_O})_{V_{\mathrm{O}}}$, where the $E^f(\mathrm{H_O})_{\mathrm{Perfect}}$ is the formation energy of H_{O} in perfect $SrTiO_3$ host crystal ($\Delta n_1 = 1$, $\mu_1 = \mu_{\mathrm{O}}$, $\Delta n_2 = -1$, $\mu_2 = \mu_{\mathrm{H}}$ in Eq. (4.1)), and $E^f(\mathrm{H_O})_{V_{\mathrm{O}}}$ is calculated with V_{O} incorporated $SrTiO_{3-1/27}$ supercell as a host ($\Delta n_1 = 0$, $\Delta n_2 = -1$, $\mu_2 = \mu_{\mathrm{H}}$). The $E^f(\mathrm{H_O})_{V_{\mathrm{O}}}$ represents the annealing experiment for $SrTiO_{3-\delta}$ under H_2 atmosphere. The defect formation energies of H_{O} calculated with PBE and HSE functionals are shown in Fig. 4.10(c) and (d), respectively. Although the band gap value is greatly improved in HSE calculation, the overall nature of the defect formation energies of H_{O} calculated with PBE and HSE are almost the same. In Figs. 4.10(c) and (d), the hydrogen atom is not likely to substitute the oxygen atom in perfect $SrTiO_3$ under the annealing with H_2 atmosphere, because $E^f(\mathrm{H_i})$ shown in Fig. 4.7 is slightly lower than $E^f(\mathrm{H_O})_{\mathrm{Perfect}}$. On the other hand, the formation energy of $E^f(\mathrm{H_O})_{V_{\mathrm{O}}}$ is greatly lower than $E^f(\mathrm{H_i})$ and the value shows negative sign with E_{F} value within entire band-gap range. Therefore, the H atom stably occupies the V_{O} site in the oxygen vacancy site in $SrTiO_{3-\delta}$.

4.3.4 Partial density of states (PDOS) of H_{O}

The results of first principles calculation indicates that the hydrogen at the oxygen-vacancy site is negatively charged hydride (H^-). The H^- character of the hydrogen indicates fully occupied H-1s sate, which should be explained in terms of the electronic structure of H_{O}. Therefore, we calculated the partial density of states (PDOS) of H_{O} in $SrTiO_3$. The PDOS of H_{O} calculated with GGA-PBE and HSE are shown in Fig. 4.11 (a) and (b), respectively. The calculations are performed with $Sr_8Ti_8O_{23}H$ supercell in charge neutral

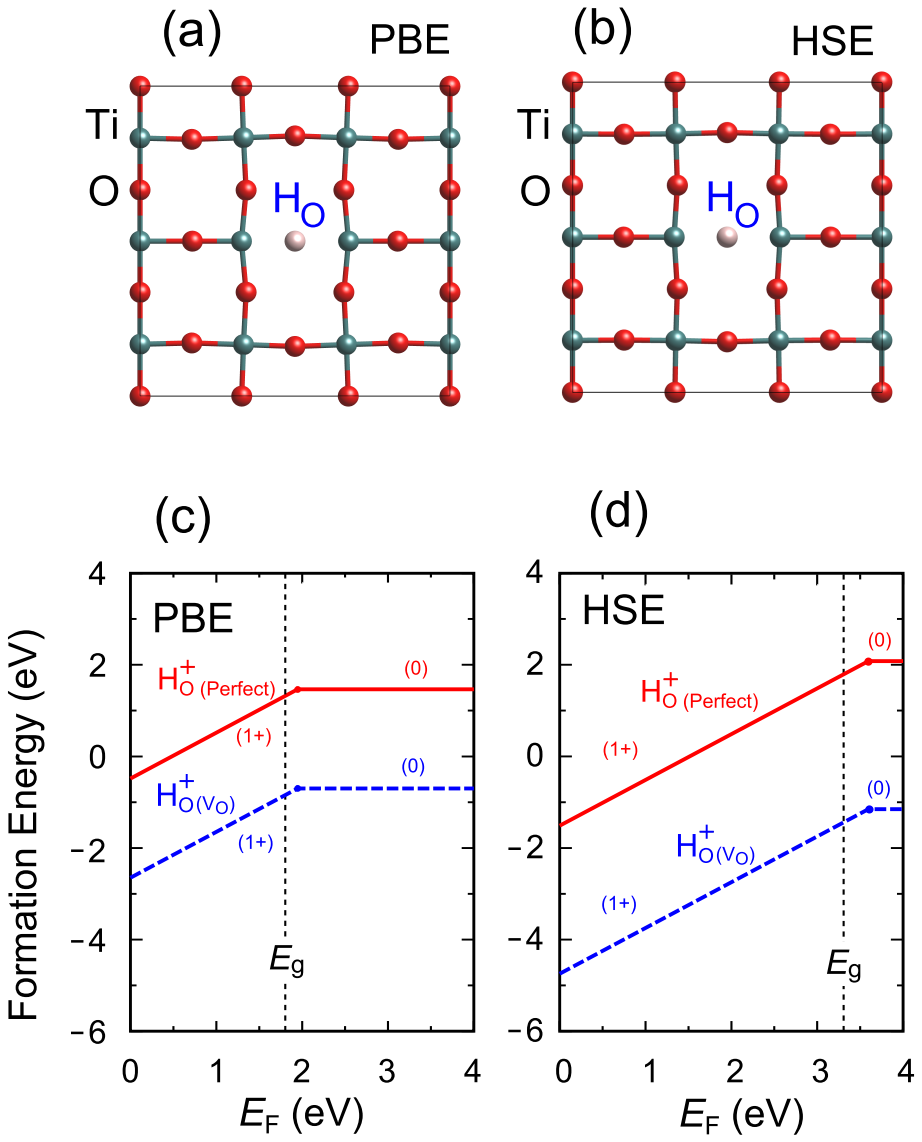

Figure 4.10: Optimized atomic configurations of hydrogen at oxygen site (H_O) calculated with (a) GGA-PBE and (b) HSE functionals. The structures are optimized with charge neutral supercells. Only a TiO_2 layer that includes defect is depicted in each supercell model. The lower figures are defect formation energies $E^f(H_O)$ calculated with (c) GGA-PBE and (d) HSE. $H^+_{O\ (Perfect)}$ is the formation energy in perfect crystal, and $H^+_{O\ (V_O)}$ is the formation energy in host crystal with the oxygen vacancy.

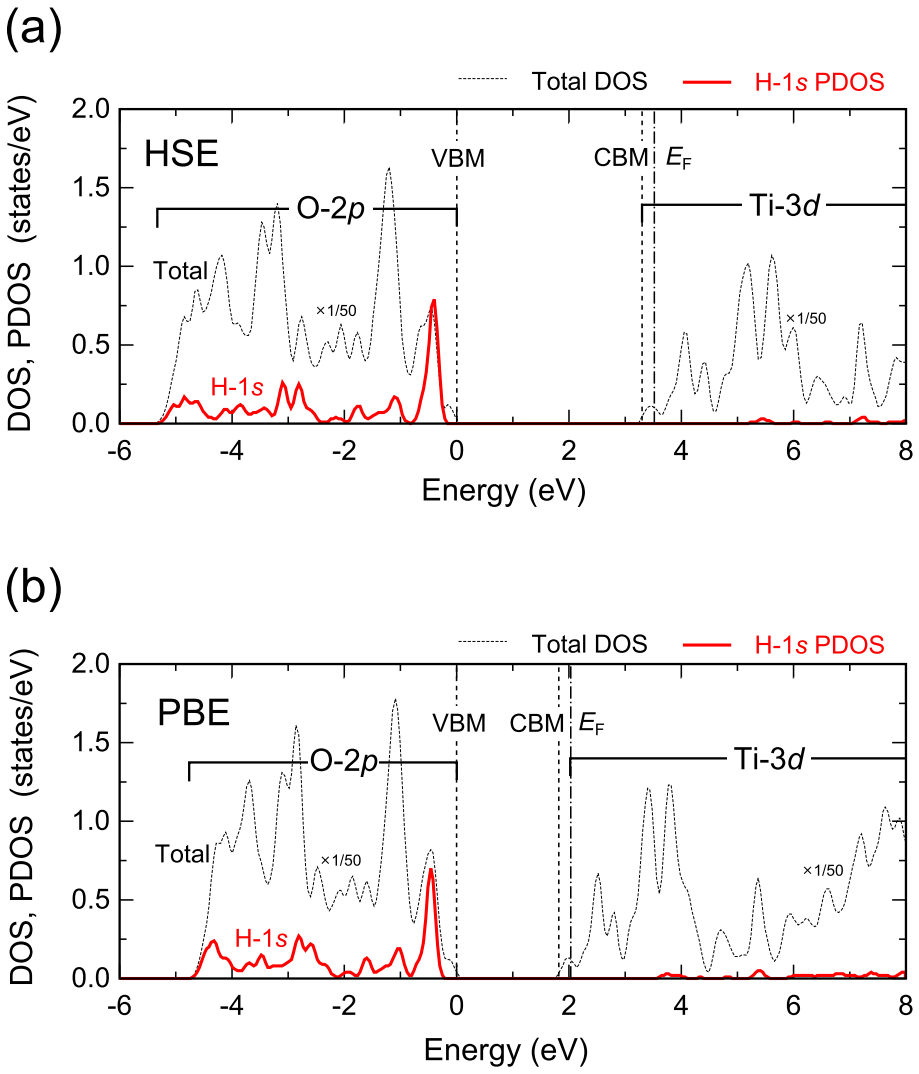

Figure 4.11: Total DOS (dashed line) and partial DOS (PDOS) of H_O (solid line) in $Sr_8Ti_8O_{23}H$ supercell calculated with (a) HSE and (b) GGA-PBE. Calculations are performed with charge neutral state. Supercell size of $2 \times 2 \times 2$ $SrTiO_3$ unit cells, and dense k-point mesh ($3 \times 3 \times 3$) are used for the calculations. The origin of horizontal axis is set at the top of O-2p band (VBM). Vertical axis of the total DOS is scaled down to 1/50.

state. In the PDOS of H_O, there is a sharp peak due to H-1s orbital just below VBM with wide distribution of H-1s character over O-2p band; therefore, the H-1s orbital is fully occupied, which indicate that the H is in a negatively charged H^- state. The H^- character of hydrogen is also confirmed by Bader charge analysis, which shows $n_{H_O} = 1.67$ (HSE), while the value for H_i is $n_{H_i} = 0.37$(HSE). Therefore, the electronic structure of H^- can be simply explained by the fully occupied H-1s orbital whose position is just below the VBM.

4.4 Replacement of O by multiple H

Our calculations indicate that H_O^+ is the source of the apparent 1+ stability of the oxygen vacancy in $SrTiO_3$. On the other hand, previous theoretical calculations and experimental results for ZnO indicate the stability of H_2 molecule at V_O site [70, 75, 76]. Furthermore, the experimentally confirmed metallic-insulator transition of $SrTiO_{3-\delta}$ under H_2 annealing [59, 77] cannot be explained by the replacement of O^{2-} by H^-, and two H^- are needed to completely compensate the carrier electrons from O^{2-}. Therefore, we tried to find possible defect structures composed of the V_O and several hydrogen atoms, and found several (meta-)stable structures as shown in Fig. 4.12(a), (b) and (c). The simplest structure is a H_2 molecule at the V_O site ($(H_2)_O$) shown in Fig. 4.12(a). We also found two additional structures containing two hydrogen atoms at the V_O site: asymmetric $(2H)_O$ and symmetric $(2H)'_O$, which are shown by Figs. 4.12(b) and 4.12(c), respectively. These two $(2H)_O$ and $(2H)'_O$ structures can be obtained by optimizing asymmetrically and symmetrically aligned initial atomic configurations in the supercell models.

The defect levels due to the incorporation of two H atoms at V_O site are confirmed by PDOS calculations. The results obtained with GGA-PBE and HSE are shown in Fig. 4.13. We found that a deep in-gap state appears for $(2H)_O$ and $(2H)'_O$ structures, where all carrier electrons are trapped by the in-gap state and the Fermi level position is just on the defect level. On the other hand, a deep level below O-2p band appears in $(H_2)_O$ structure. The shape of the wave function for the defect levels are calculated to confirm the nature of the defect levels. Figure 4.14 shows band decomposed change density for these defect states shown by ii), v) and vii) in Fig. 4.13.

From the defect levels confirmed by PDOS calculation and the shape of the wave function for the defect states, the formation of the hydrogen related defect species can be summarized with a diagram shown in Fig. 4.15. The energy level related with the $(H_2)_O$ can be regarded as a simple H_2 molecule that has bonding and anti-bonding states as shown in Fig. 4.15(e). There are

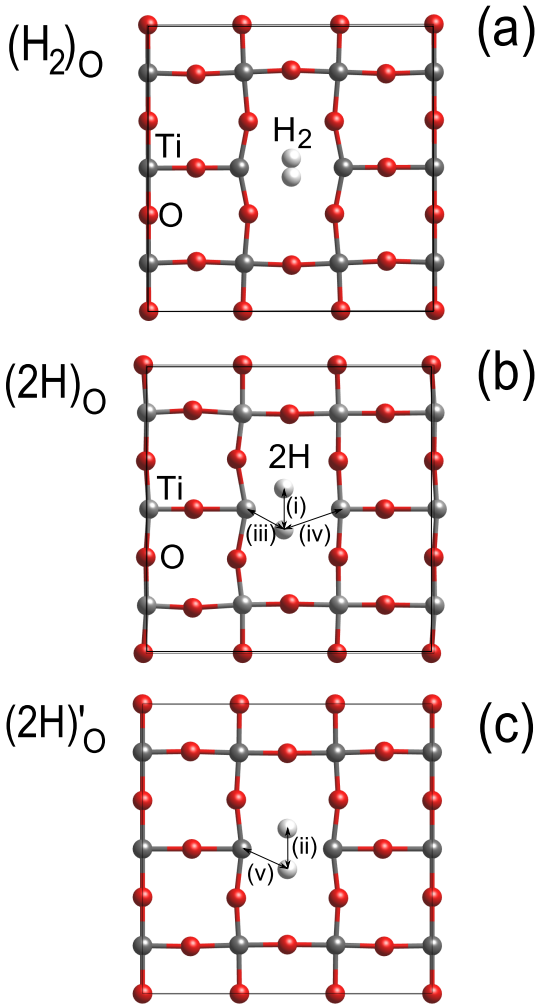

Figure 4.12: Optimized defect structures composed of (a) H_2 molecule-like structure at V_O site, two (b) asymmetrically and (c) symmetrically trapped H atoms at V_O site. All structures are optimized with charge neutral state. The H-H bond lengths shown by (i) and (ii) are 1.67 and 1.64 Å, and the Ti-H bond lengths shown by (iii), (iv) and (v) are 1.75, 2.46, and 2.01 Å, respectively. The calculations are performed with HSE functional.

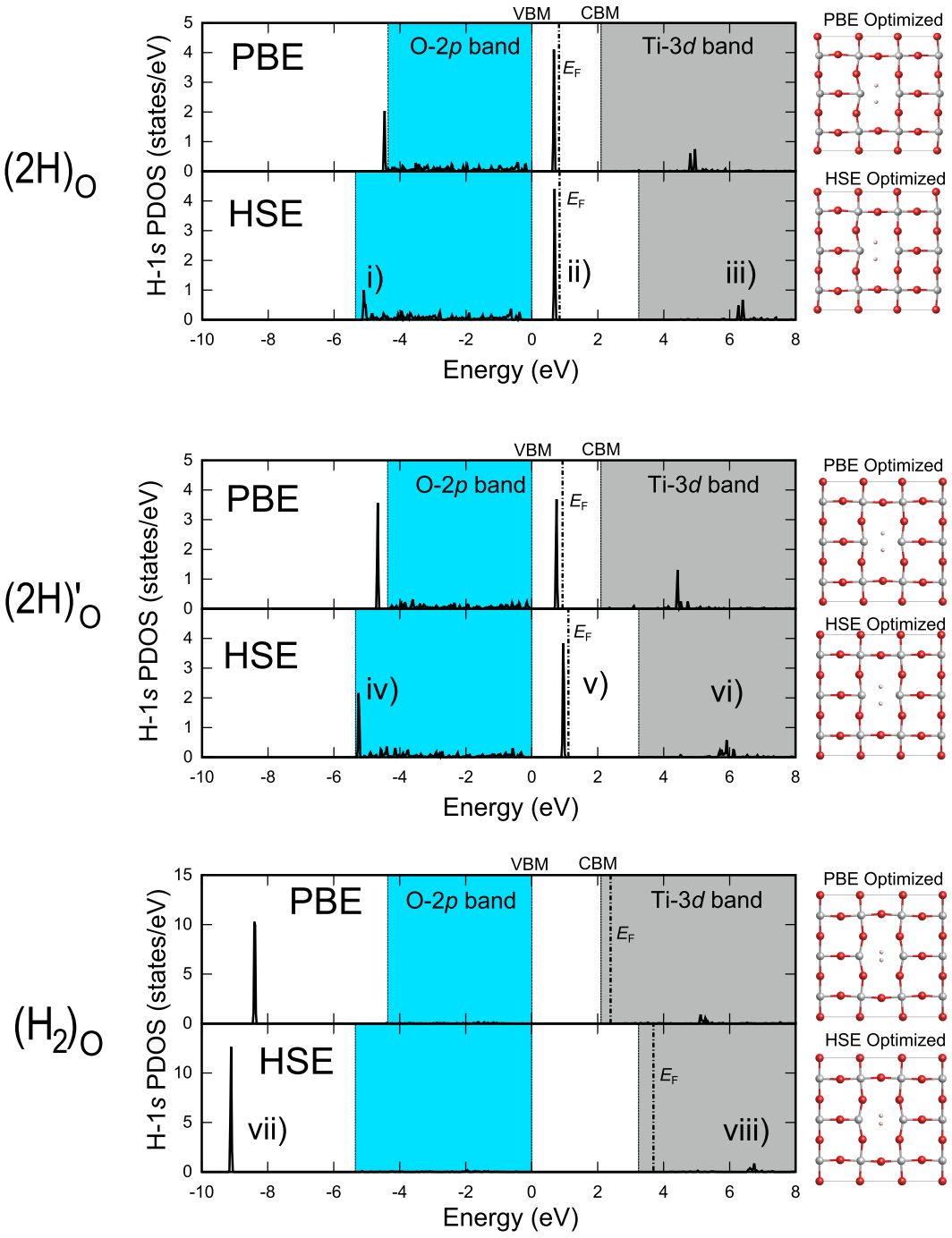

Figure 4.13: Partial density of states (PDOS) of H for $(2H)_O$, $(2H)'_O$ and $(H_2)_O$ shown in Fig. 4.12. A deep in-gap state appears in $(2H)_O$, $(2H)'_O$ and all carrier electrons are trapped at the deep-defect level, whereas there are no in-gap state in $(H_2)_O$.

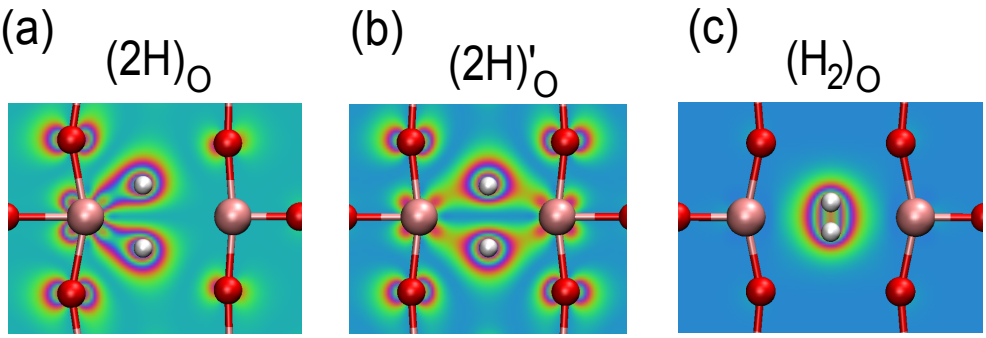

Figure 4.14: Band decomposed charge density for occupied defect states in $(2H)_O$, $(2H)'_O$ and $(H_2)_O$ indicated by ii), v) and vii) in Fig. 4.13. The color in these contour plots are in proportion to the charge density.

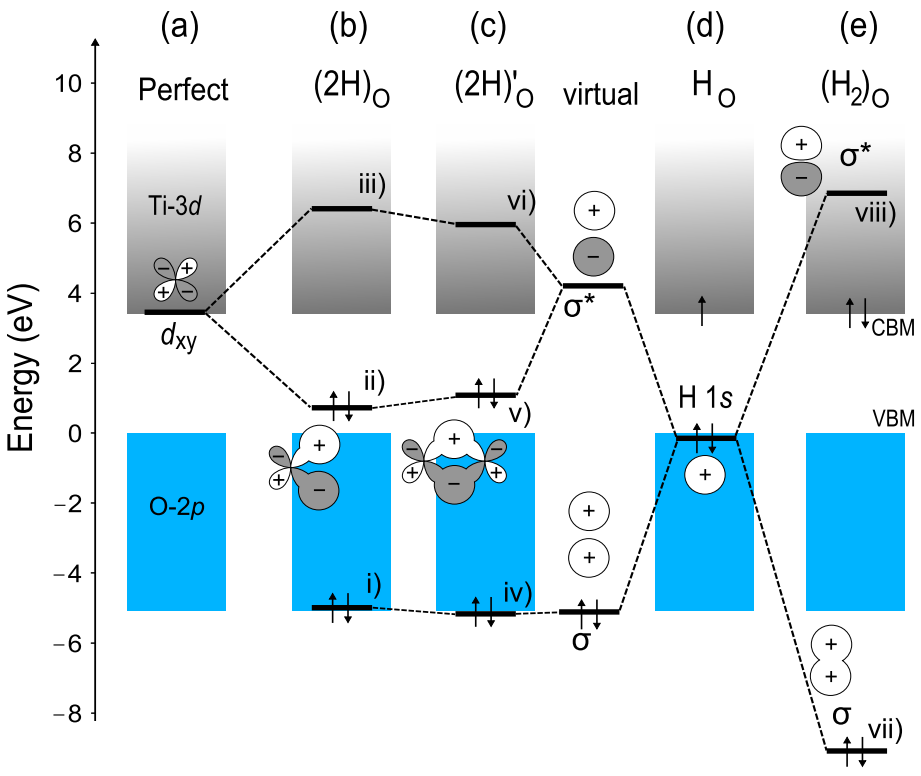

Figure 4.15: Chemical bonding scheme for H that occupies V_O site in $SrTiO_3$. (a) Perfect $SrTiO_3$ crystal. (b) Asymmetrically and (c) symmetrically introduced two H atoms that passivate dangling-bond of Ti-3d orbitals at V_O site. (d) One hydrogen atom that simply replaces an oxygen atom. (e) H_2 molecule-like structure at V_O site.

no in-gap state due to the hydrogen molecule at V_O site, which brings about two carrier electrons located at CBM from the doubly charged V_O^{2+}. On the other hand, the electronic structure of $(2H)_O$ and $(2H)'_O$ are completely different from $(H_2)_O$; a deep in-gap state appears and all carrier electrons are trapped by the defect state due to $(2H)_O$ and $(2H)'_O$. There are no free carrier electrons around the CBM and the system becomes an insulating state as shown in Figs. 4.15(b) and (c). The deep in-gap state related to $(2H)_O$ and $(2H)'_O$ can be regarded as a bonding state of Ti-3*d* orbitals composing CBM of host $SrTiO_3$ crystal (Fig. 4.15(a)) and anti-bonding state of two weakly bonded hydrogen at V_O site (shown by "virtual" in Fig. 4.15). The situation can be regarded as a passivation of Ti-3*d* dangling bonds by H atoms.

The evaluations of the formation energies are important for discussing the reality of these defect complexes; therefore, the formation energies of $E^f((H_2)_O)$, $E^f((2H)_O)$ and $E^f((2H)'_O)$ are evaluated, and these formation energies are compared with the sum of the other hydrogen incorporation: $2 \times E^f(H_i)$ and $E^f(H_i) + E^f(H_O)$. The calculation of the formation energies are based on oxygen vacancy incorporated host $SrTiO_{3-1/27}$ crystal composed of $3 \times 3 \times 3$ $SrTiO_3$ unit cells except for the $E^f(H_i)$ where perfect $SrTiO_3$ crystal is used as a host. The formation energies calculated with HSE are shown in Fig. 4.16 (a), where the sum of the formation energies $E^f(H_i) + E^f(H_O)$ is the stable defect combination over wide E_F range, except for around $E_F = E_g$ where the most stable defect species is $(2H)^0_O$. Furthermore, the value of the formation energy of $(2H)^0_O$ shows a negative sign, which indicates that two H can be stably trapped at the V_O site when the oxygen vacancy containing $SrTiO_{3-\delta}$ are subject to the H_2 atmosphere. The defect formation energies also indicate that the $(2H)^0_O$ defect structure is unstable against the removal of the electron from the supercell, and the $(2H)^0_O$ is easily converted into $(H_2)^{2+}_O$. The $(2H)'^0_O$ defect structure shows almost the same tendency, thus the defect-formation energies of $(2H)_O$ and $(2H)'_O$ converge into that of $(H_2)^{2+}_O$ other than the charge-neutral state. The formation energies of $H^+_O + H^+_i$ and $(2H)^0_O$ has a cross point at $E_F = 3.22$ eV, which is very close to $E_g = 3.31$ eV. In addition to the instability of $(2H)^0_O$ against the Fermi level, the energy difference between $E^f(H_O) + E^f(H_i)$ and $E^f((2H)_O)$ at $E_F = E_g$ is only 0.185 eV. Therefore, the $(2H)_O$ state would easily dissociates into $H_O + H_i$ due to the kinetics of H in a thermally excited state. The weak stability of $(2H)_O$ indicates that very specific experimental conditions are required for V_O to be filled with two H^-. The speculation is consistent with the experimental results for V_O-incorporated $SrTiO_{3-\delta}$ single crystals, where a transparent insulating state is recovered by H_2 annealing, whereas O_2 annealing does not lead to the recovery of the complete transparent state [59].

Note that the stability of $(2H)_O$ never appears in GGA-PBE calculations,

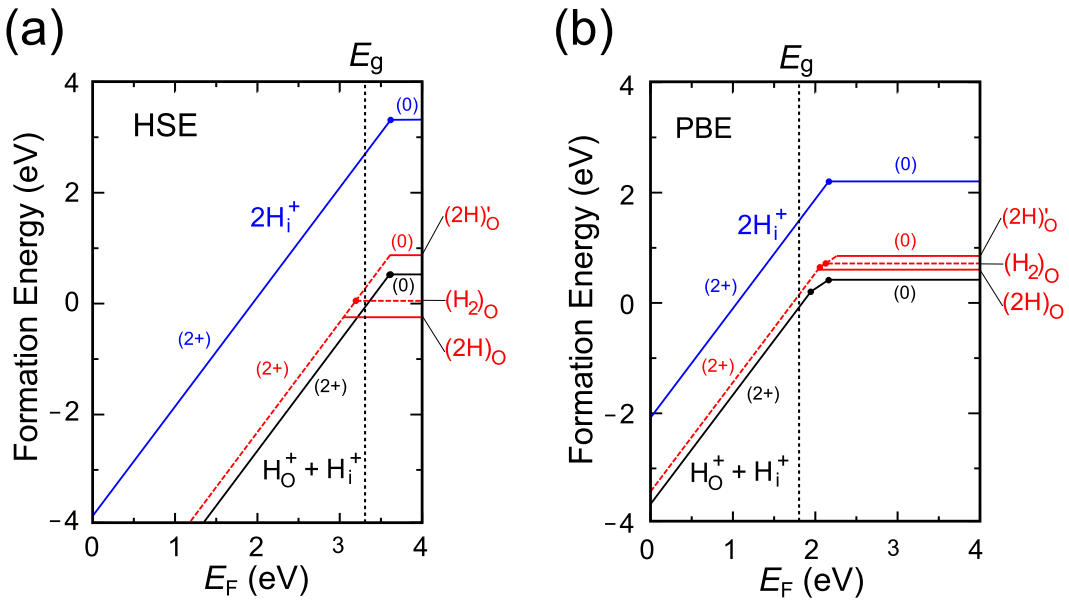

Figure 4.16: Formation energies calculated with (a) HSE and (b) PBE exchange-correlation functionals. Formation energies of $E^f((H_2)_O)$, $E^f((2H)_O)$, $E^f((2H)'_O)$ are compared with $E^f(V_O) + 2E^f(H_i)$ and $E^f(H_O) + E^f(H_i)$. The $(2H)_O$ and $(2H)'_O$ defect structures becomes $(H_2)_O$ when an electron is removed; therefore, there are two branches in the formation energies of $(H_2)_O$.

as shown in 4.16(b). In the PBE calculations, the stable defect species around $E_F = E_g$ is $H_O^+ + H_i^+$, and the formation energy of $(2H)_O$ is always higher than that of $H_O^+ + H_i^+$ irrespective of the position of the Fermi level. The stability of $(2H)_O$ obtained in the HSE calculation would be partially due to a deeper in-gap state compared to the results of the PBE calculation (17% of E_g from VBM for HSE, and 29% for PBE).

These results indicate that the Hydrogen can modify the carrier-electron density in the oxygen-deficient $SrTiO_3$ by forming various defect complexes.

4.5 Vibrational property of H at O site

Vibrational frequencies of hydrogen atoms positioned at the oxygen vacancy site are useful information for the experimental verification. We calculated the infrared absorption (IR) spectrum for H_O and $(2H)_O$ with linear response formalism [140–142]. The infrared spectrum is described based on Hessian matrix (also known as dynamical matrix) and Born effective charges. Hessian matrix is second derivatives of the total energy E over Cartesian coordinate of periodic system, and they are used to determine harmonic vibrational frequencies. The important factor for the infrared spectrum calculation is the Hessian matrix at Γ point: $\mathbf{k} = 0$, where $\mathbf{k}$ is the vector in the first Brillouin zone. The Born effective charge tensor (Z^*) is the partial derivative of the macroscopic polarization with respect to a periodic displacement of all the periodically arranged ions at zero macroscopic electric field, which can be calculated within the linear response formalism proposed by Gonze [140,141]. The intensities of infrared-active modes are given by the Born effective charge tensor and mass-weighted Hessian. Hessian $H_{i,j}$ are calculated as follows:

$$H_{i,j} = \frac{\partial^2 E}{\partial q_i \partial q_j}, \tag{4.2}$$

where q_i is a Cartesian coordinate of a system with N atoms ($1 < i < 3N$). The mass-weighted Hessian is obtained by dividing the Hessian elements by the square roots of the atomic masses:

$$F_{i,j} = \frac{H_{i,j}}{\sqrt{m_i m_j}}. \tag{4.3}$$

The intensities of infrared-active modes are given by the corresponding oscillator strengths defined as follows [142]:

$$I_i = \left(\sum_{j,k} F'_{i,j} Z^*_{j,k} \right)^2, \tag{4.4}$$

where F' are vibrational eigenvectors of normal mode i for mass-weighted Hessian F. According to the harmonic approximation, the square roots of the eigenvalues of F are the vibrational frequencies and the eigenvectors of F are the normal modes. Under periodic boundary condition in solid crystal, there is an infinite number of atoms. However, the infinite Hessian matrix can be Fourier transformed into an infinite set of $3N \times 3N$ matrices due to the periodicity of the Hessian ($H_{i,j} = H_{i+\mathbf{T}_j+\mathbf{T}}$), where $\mathbf{T}$ is the lattice translations vector.

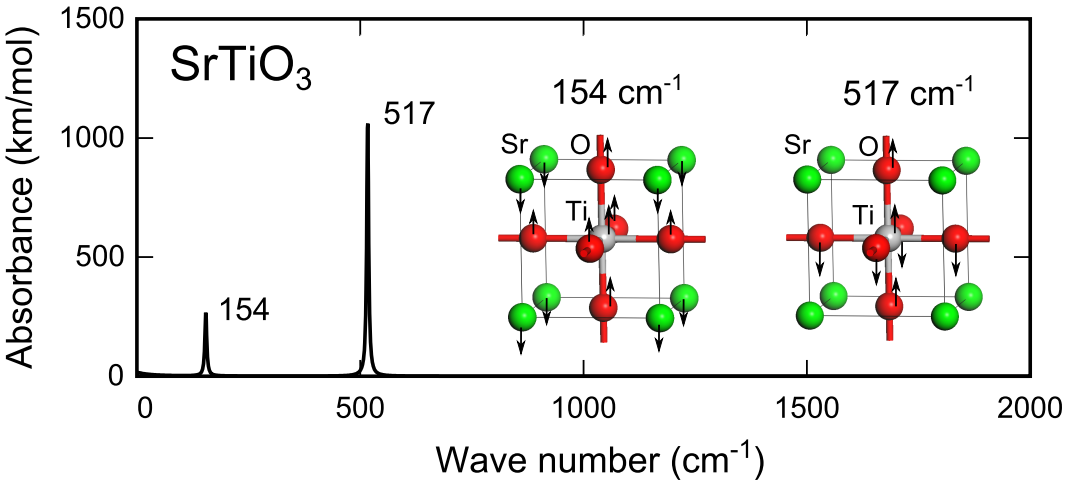

Figure 4.17: Infrared absorption spectrum of $SrTiO_3$ calculated with linear response based on density functional perturbation theory (DFPT). The calculations were performed with GGA-PBE exchange correlation functional. Three vibrational peaks are calculated: 515, 154 and -57 (not shown in the spectrum).

The calculated infrared absorption spectrum for $SrTiO_3$ unit cell (5 atoms) with GGA-PBE are shown in 4.17, where the frequency of two vibrational modes (517 and 154 cm^{-1}) well agree with experimentally confirmed vibrational modes in $SrTiO_3$ single crystal: 546 and 178 cm^{-1}, respectively [143]. The experimentally confirmed lowest-mode frequency (87.7 cm^{-1}) [143], which are closely related to ferroelectric displacement has negative value (-57 cm^{-1}) in the above calculation. Therefore, the ferroelectric displacement (tetragonal phase with $P4mm$ symmetry) observed in ferroelectric $BaTiO_3$ makes the total energy of $SrTiO_3$ slightly lower ($\Delta E = 1.34$ meV for 5 atom unit cell). Unfortunately, these results are not consistent with experimental fact that the $SrTiO_3$ does not show the ferroelectricity.

The ferroelectric deformation is closely related with the volume of the unit cell, and shrinkage/expansion of the volume suppress/enhance the ferroelectric deformation. For example, hydrostatic pressure (2-3 GPa) [144, 145] makes the ferroelectric tetragonal phase of $BaTiO_3$ into paraelectric cubic phase with shrinkage of lattice constant by 0.023 Å [144]. We confirmed that the lowest mode frequency becomes positive (110 cm^{-1}) in local density approximation (LDA) and the ferroelectric displacement does not appears in $SrTiO_3$. The experimental lattice constant of $SrTiO_3$ is 3.904 Å, whereas lattice constant calculated LDA is 3.838 Å and that of GGA is 3.917 Å. The

difference of the lattice constant between LDA and GGA is 0.079 Å, which is sufficiently larger than the experimentally confirmed critical lattice shrinkage (0.023 Å) induced by hydrostatic pressure; therefore, the unexpected emergence of ferroelectricity in $SrTiO_3$ would be due to the volume expansion of GGA-PBE exchange-correlation functional. Nevertheless, we will use GGA-PBE for the calculation of vibrational modes of hydrogen atoms in $SrTiO_3$ hereafter, because GGA can correct the failure of LDA such as overestimate of the binding energies of molecules and solids [146]. Furthermore, a more realistic description of energy barriers in the dissociative adsorption of hydrogen on metal and semiconductor surfaces has been reported as an advantage of GGA [147, 148].

Figure 4.18 (a) shows calculated infrared spectrum of H at O site (H_O). The calculations were performed with a supercell composed of $2 \times 2 \times 2$ $SrTiO_3$ unitcells ($Sr_8Ti_8O_{23}H$). In the calculation of the infrared absorption spectrum, the supercell is single positively charged ($+1e$) to remove the free carrier electron shown in Fig. 4.11. The characteristic peaks of the vibrational modes of H is at 1,259 cm^{-1} and 810 cm^{-1}, whose vibrational modes are simultaneously shown in Fig. 4.18 (a). The frequency region is much lower than that of typical O-H stretching vibrational mode for an interstitial hydrogen H_i ($\sim 3,500$ cm^{-1}), and little attention has been paid for this frequency range. Figure 4.18 (b) indicates the vibrational modes for the most stable atomic configuration of the two hydrogen atoms positioned at the oxygen vacancy site: $(2H)_O$. The supercell used for the calculation is composed of $Sr_8Ti_8O_{23}H_2$. Contrary to the H_O defect species, the $(2H)_O$ traps all of the free carrier electrons and the system becomes an insulating state; hence the charge neutral supercell with $(2H)_O$ is used for the calculation. The typical four vibrational modes related to the movement of hydrogen are illustrated in these figures, and their frequencies are 1,056, 1,157, 1,468 and 1,561 cm^{-1}, respectively. These vibrational modes have also considerably low frequencies than the O-H stretching vibrational mode.

4.6 Summary

In conclusion, we performed first-principles calculations based on GGA-PBE and hybrid HSE functionals to identify the defect complexes generated under H_2 annealing for $ATiO_3$ (A = Sr, Ba). Our results indicate that the hydrogen can change its character from H^+ into H^- during the diffusion from interstitial site into oxygen vacancy cite by absorbing two electrons into H-1s orbital. The formation energy indicates that the H_O^+ is actually possible in H_2 annealing experiments for $SrTiO_3$, which can account for the experimen-

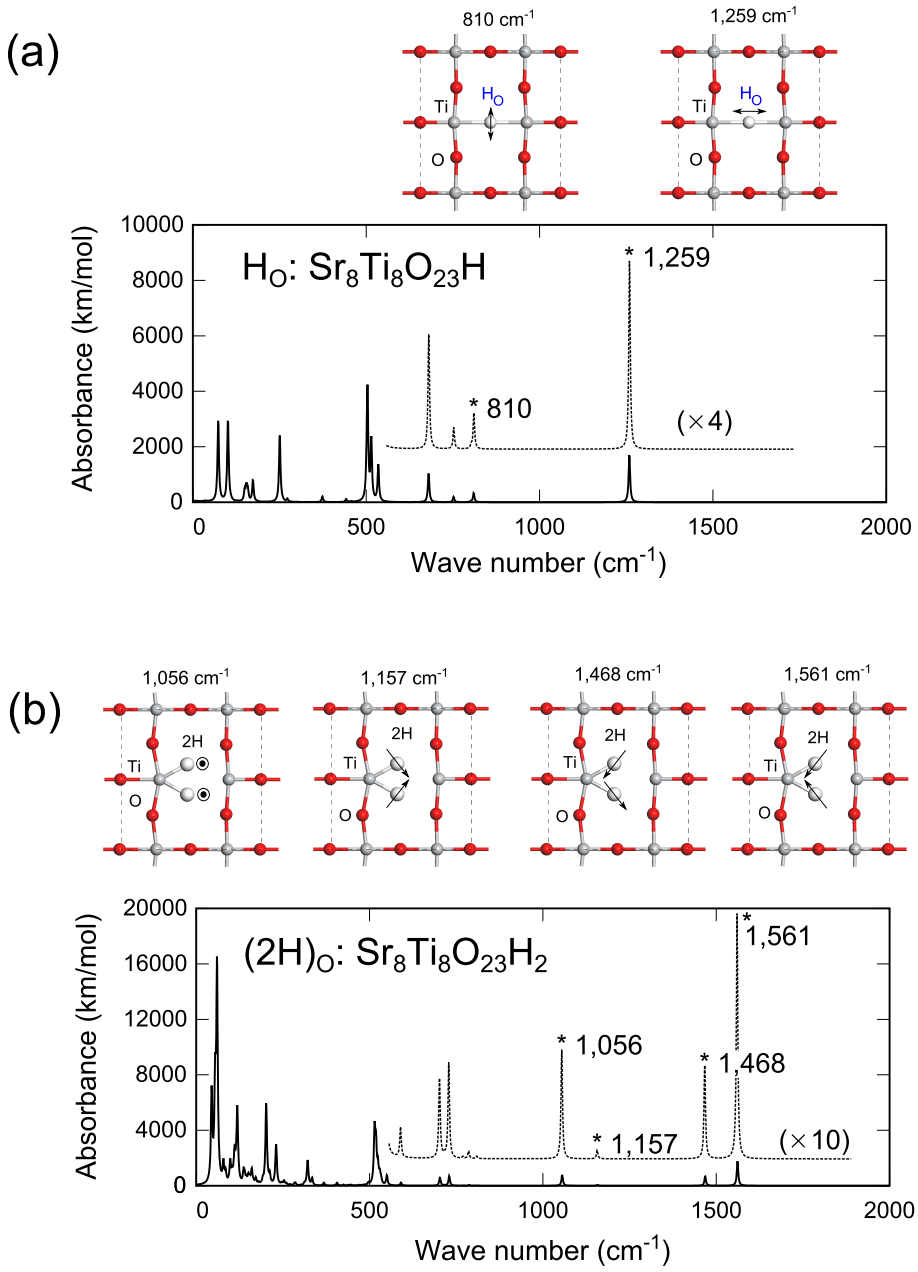

Figure 4.18: Infrared absorption spectrum of (a) H_O with a supercell composed of $Sr_8Ti_8O_{23}H$ and (b) $(2H)_O$ with a supercell composed of $Sr_8Ti_8O_{23}H_2$ calculated with linear response based on density functional perturbation theory (DFPT). The charge states of the supercell used for the calculation of H_O and $(2H)_O$ is $+1e$ charged and charge neutral state, respectively.

tally observed apparent 1+ stabilities of the oxygen vacancy in $SrTiO_3$. It is generally believed that the incorporation of the hydrogen increases the n-type carrier electron in $SrTiO_3$. However, our results indicate that the hydrogen can decrease the carrier electron density by the formation of H_O^+. These results strongly indicates that the experimentally confirmed V_O^+ valence state is due to the stable formation of H_O^+. The speculation is also supported by the experimental results of hydride oxygen exchange in $BaTiO_3$ [149], where they confirmed that the replacement of O^{2-} by H^- is actually possible from the analysis of neutron diffraction and NMR for $BaTiO_3$ samples reduced with alkaline earth hydrides.

Furthermore, we found that H_O^+ weakly captures an additional H^- and forms the $(2H)_O^0$ complex defect species, which completely neutralizes V_O^{2+}. The results indicate that careful H_2 annealing experiments can change the oxygen-deficient n-type conducting $SrTiO_{3-\delta}$ samples into insulating transparent state. The results are consistent with previous experimental results that the V_O incorporated $SrTiO_{3-\delta}$ single crystal recovers transparent insulating state by the H_2 annealing, whereas O_2 annealing cannot recover the complete transparent state [59].

The negatively charged nature of hydrogen has been previously pointed out for ZnO [70, 72] and other semiconductors [73, 74]. Even though the nature of H^- in perovskite-type oxides has hardly been discussed, our results indicate that the replacement of O^{2-} by H^- is a general phenomenon observed in a wide variety of transition metal oxides. The H_2 gas is commonly used as reducing agent for $ATiO_3$, and many previous experiments assume a simple oxygen vacancy (V_O^{2+}) (or interstitial H_i) as a source of carrier electron. An important suggestion from the results is that the n-type conductivity experimentally confirmed for H_2 annealed $SrTiO_3$ is not due to the simple oxygen vacancies, but all of the oxygen vacancies are filled with negatively charged hydride ion (H^-). This is an important suggestion from theoretical calculations because many previous studies of oxygen vacancy in $ATiO_3$ (A = Ba, Sr, Ca) assume simple picture of the oxygen vacancy (or oxygen-vacancy clustering), and the replacement of O by H has not been considered [30–33, 58, 60–64, 66, 67]. Therefore, the effects of the hydrogen occupying the V_O^{2+} site by one (or two) H^- are extremely important, because it requires reconsideration for previous experiments, and contributes to the development of hydrogen-based carrier electron control in transition metal oxides.

Chapter 5

Relation between donor-type defect and ferroelectricity

In this chapter, we concentrated on the ferroelectricity in $BaTiO_3$, and discuss the effect of donor-type impurities on the suppression of the ferroelectric phase based on the results of first principles calculation. We studied the pure effects of electron doping in $BaTiO_3$ with uniform background charge compensation, and found that the free carrier electron intrinsically eliminates the ferroelectric displacement in $BaTiO_3$ [96, 150]. The critical electron concentration for the T-C phase transition is calculated to be $n_{\text{elec.}} = 0.085\ e/(\text{unit cell})(1.36 \times 10^{21}\ \text{cm}^{-3})$ [96]. We further clarified that the lattice deformation around the defect accelerates the disappearance of the ferroelectric phase of $BaTiO_3$ [96, 150]. These results explain the experimentally observed relation between the ferroelectricity and the donor-type dopants in ferroelectric phase of $BaTiO_3$.

5.1 Introduction

Ferroelectricity is a typical property inherent in some perovskite-type oxides, which makes the perovskites particularly useful for various electronic device applications as shown in Table 1.1. However, the ferroelectricity is known to easily disappear via various factors. The influence of the carrier-electron doping on the disappearance of the ferroelectricity has been explained in Chap. 1, therefore we mainly discuss the results of our calculations in this chapter. In section 5.2, we will briefly explain the computational details. In section 5.3, the pure effects of carrier electron on the ferroelectric phase of $BaTiO_3$ are discussed. The pure effect of the carrier-electron doping can be studied only from theoretical approach, because the experimental electron

doping is inevitably followed by lattice deformations around donor-type defects and dopants; therefore, theoretical study of the carrier doping effects is of great importance. We found that component analysis for the total energy of DFT can well explain the disappearance of ferroelectric phase due to the carrier-electron doping. We also show that the approach can be used for the explanation for the origin of the ferroelectricity in $BaTiO_3$. In section 5.4, the effects of lattice deformation induced by lattice defects are explained. Several typical donor-type defect species are included in our study, such as oxygen vacancy (V_O^{2+}), Nb^{5+} at Ti^{4+} site and H_O^+. Especially, the effects of H_O^+ is interesting because we found that the H_O^+ is one of major defect species in $BaTiO_3$ annealed under H_2 gas. Finally, the results are summarized in section 5.5.

5.2 Computational details

The c/a ratio of tetragonal (T) phase $BaTiO_3$ is very accurately reproduced by local density approximation (LDA) (calc. 1.009, exp. 1.010 [1]), whereas generalized gradient approximation (GGA) greatly overestimate the value of c/a (calc. 1.050 [1]). These behaviors are qualitatively explained by the optimized volume with each functional (calc. 61.9 (LDA) and 67.2 (GGA), exp. 64.4 Å^3 [1]); the large volume in GGA induces the lattice instability of $BaTiO_3$, which brings about the large c/a ratio in $BaTiO_3$ [151]. Therefore, we adopted LDA in the present calculations. The calculations are performed with the ultrasoft pseudo-potential (USPP) implemented in CASTEP code [138]. The USPPs are constructed with the atomic reference configurations of $5s^25p^66s^2$ for Ba, $3s^23p^63d^24s^2$ for Ti, $4s^24p^64d^45s^1$ for Nb and $2s^22p^4$ for O. A Plane-wave basis set with a cutoff energy of 500 eV was used in all calculations. The cell parameters were relaxed under isobaric conditions with a convergence tolerance of 10 MPa. Our calculations gave $c/a = 1.010$ and volume $v = 61.40$Å^3 in T phase $BaTiO_3$, which agrees well with previous reports. [1, 152]

5.3 Electron-induced phase transition

Figure 5.1(a) shows the crystal structure of the T-phase $BaTiO_3$ unit cell with $P4mm$ symmetry. We found that the electron doping in the T-phase $BaTiO_3$ changes the positions of the inner atomic coordinates into more high-symmetry states as shown in Fig. 5.1(b). The tetragonality (c/a ratio) decreases with increasing electron doping, and finally reaches $c/a = 1.000$ at

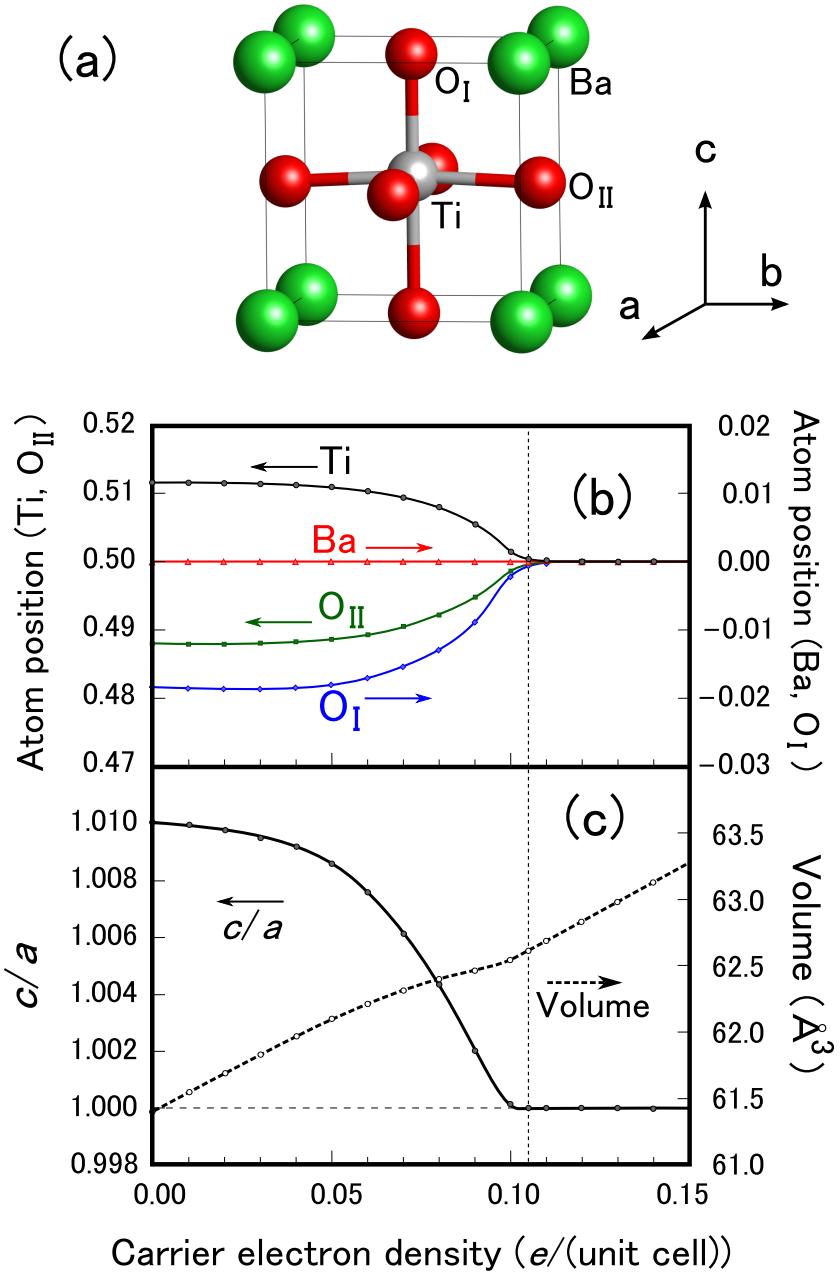

Figure 5.1: (a) Crystal structure of $BaTiO_3$ tetragonal phase. (b) Shifts of c-axis atomic positions of Ba, Ti, O_I, and O_{II} in the $BaTiO_3$ unit cell induced by electron doping. (c) The c/a ratio and unit cell volume of $BaTiO_3$ as a function of carrier-electron doping.

a critical electron concentration of $n_{\mathrm{elec.}} = 0.105$ e/(unit cell) (1.68×10^{21} cm^{-3}) as shown in Fig. 5.1 (c), which indicates that the electron doping induces tetragonal-cubic (T-C) phase transition. In these calculations, overall charge neutrality is maintained by uniform background charges without the effects of lattice disorder induced by donor dopants; hence, the results shown in Figs. 5.1 indicate that the T-C phase transition is an intrinsic effect of carrier-electron doping in $BaTiO_3$. The volume of the electron-doped $BaTiO_3$ increases according to the increase of the electron concentration with a slight anomaly occurring at the electron concentration at which the carrier-induced phase transition occurs, as shown in Fig. 5.1(c). We also calculated the effects of the electron doping for other ferroelectric phases in $BaTiO_3$: orthorhombic (O) and rhombohedral (R) phases and confirmed that a similar cubic phase transitions occur with almost the same critical-electron concentration for T phase, which indicates that the disappearance of the ferroelectric phases is an intrinsic result of electron doping in $BaTiO_3$. It should be noted that the disappearance of the ferroelectric phase due to the carrier electron remarkably depends on the number of k-point sampling grids. The calculations in Fig. 5.1 are performed with $8 \times 8 \times 8$ k-point sampling grids. Even though the c/a ratio is well converged with $8 \times 8 \times 8$ grids in insulating $BaTiO_3$ as shown in Fig. 5.2 (a), the c/a ratio in electron doped system is not sufficiently converged at the number of the grids. We checked the convergence of the critical-electron concentration for the T-C phase transition up to $14 \times 14 \times 14$ k-point grids, and found that the converged value of the critical carrier electron concentration is 0.085 e/(unit cell) (1.36×10^{21} cm^{-3}) as shown in Fig. 5.2 (b).

There would be several explanations for the disappearance of the electron induced paraelectric phase transition of the ferroelectric phase of $BaTiO_3$. R. E. Cohen has pointed out that the hybridization of Ti-3d and O-2p is crucial for the ferroelectricity in $BaTiO_3$, and the ferroelectric instability vanishes if 3d variational freedom is removed [49,90]. Even though the p-d hybridization is reported to be greatly changed by the ferroelectric atomic displacements [153], we confirmed that the difference in the hybridization between T and C phases of $BaTiO_3$ is not so large when the lattice constant and inner-atomic coordinates are simultaneously optimized, as shown in Fig. 5.3(a). We also confirmed that the same feature is preserved under electron doping, and it is therefore very unclear whether the change in the p-d hybridization is responsible for the electron-induced T-C phase transition. The effects of the p-d hybridization on the ferroelectricity has also been discussed based on the difference between $SrTiO_3$ and $BaTiO_3$ [46]. $SrTiO_3$ is a typical paraelectric perovskite-type oxide that differs from $BaTiO_3$ only in the size of the alkaline-earth A-site ion, and the p-d hybridizations in both materials are very similar

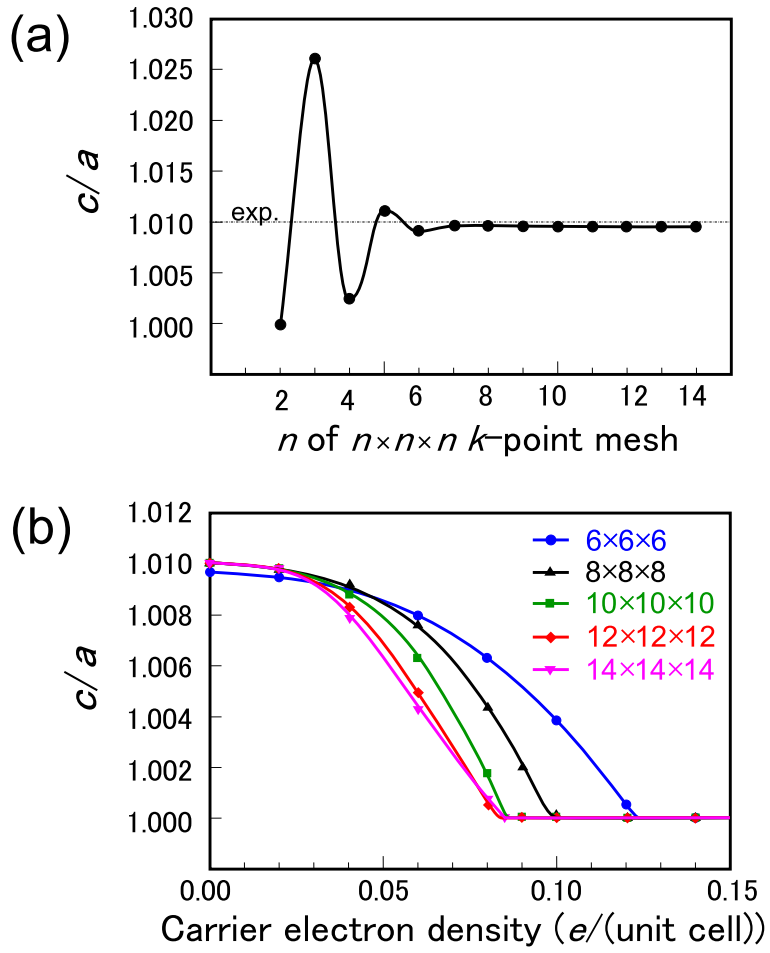

Figure 5.2: (a) k-point dependence of c/a ratio of $BaTiO_3$ tetragonal phase in charge neutral unit cell. (b) The change of c/a ratio induced by electron doping calculated with different k-point sampling meshes.

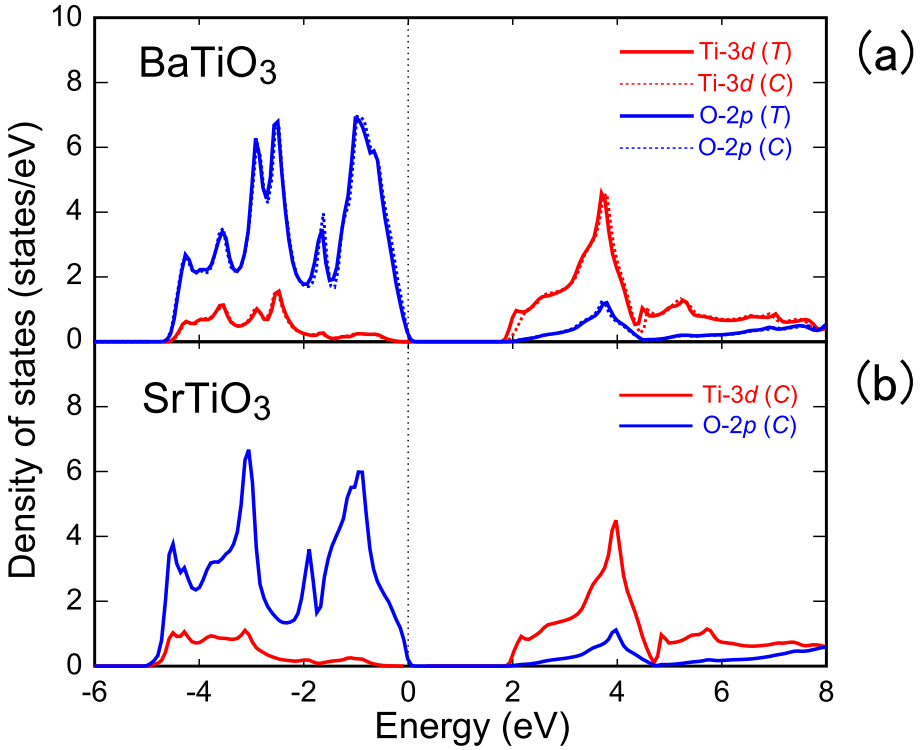

Figure 5.3: Partial density of states (PDOS) of (a) Ti-3d and O-2p in T and C phases of $BaTiO_3$ and (b) C phase $SrTiO_3$ in charge neutral unit cell (5 atoms). The lattice constant and inner-atomic coordinates of crystal structures are optimized. In both figures, O-2p states are the sum of contributions from all three oxygen atoms in the unit cell.

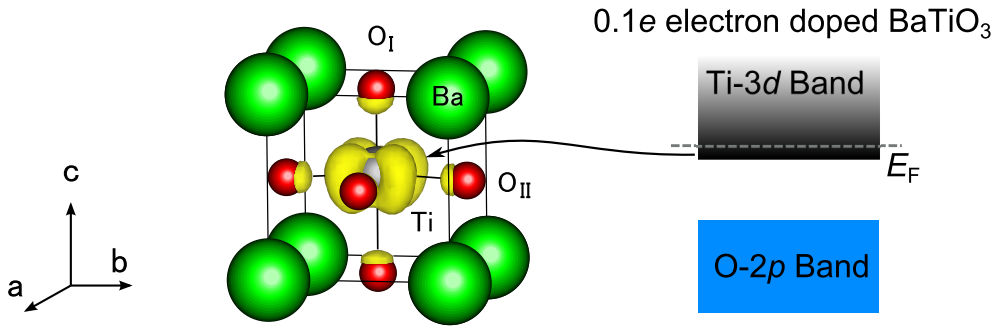

Figure 5.4: Distribution of 0.1 e/(unit cell) carrier electron in $BaTiO_3$ tetragonal crystal structure.

as shown in Figs. 5.3(a) and 5.3(b). Therefore, the discussion based on the p-d hybridization is difficult to be used for the explanation of the electron induced T-C phase transition in $BaTiO_3$ and another explanation would be required.

Analysis based on the ratio of ionic radii that comprise the perovskite lattice is a well-known approach for the explanation of the ferroelectric lattice instability [43, 44, 46], which is conventionally described by the tolerance factor $t_{ATiO_3} = (r_A + r_O)/\sqrt{2}(r_{Ti} + r_O)$ as explained in section 1.2.2. The distribution of doped carrier-electron is a key to understand the change of the ionic radii composing perovskite lattice. As shown in Fig. 5.4, doped carrier electron mainly distributes over Ti-3d orbital with weak hybridization on the O-2p orbital, reflecting the characteristic of the conduction-band bottom of $BaTiO_3$. The distribution indicates that the introduced electrons mainly reduce the valence of the Ti ions, which leads to a selective increase in r_{Ti}. Therefore, one qualitative explanation for the carrier-electron induced T-C phase transition in $BaTiO_3$ is decrease of the t value caused by the increase in r_{Ti}.

The origin of ferroelectricity is frequently discussed in terms of the long- and short-range forces based on the knowledge obtained from non-empirical model calculation [49, 154]. We found that a similar discussion is possible based on the component analysis of DFT total energies, and the analysis well explains the electron induced T-C phase transition. Furthermore, the carrier-electron doped $BaTiO_3$ is an ideal system to investigate the origin of ferroelectric lattice instability, because the difference between the cubic (electron doped) and the tetragonal (undoped) systems is only a slight difference in electron number, which enables us to study very small energy gains caused by the ferroelectric lattice deformation.

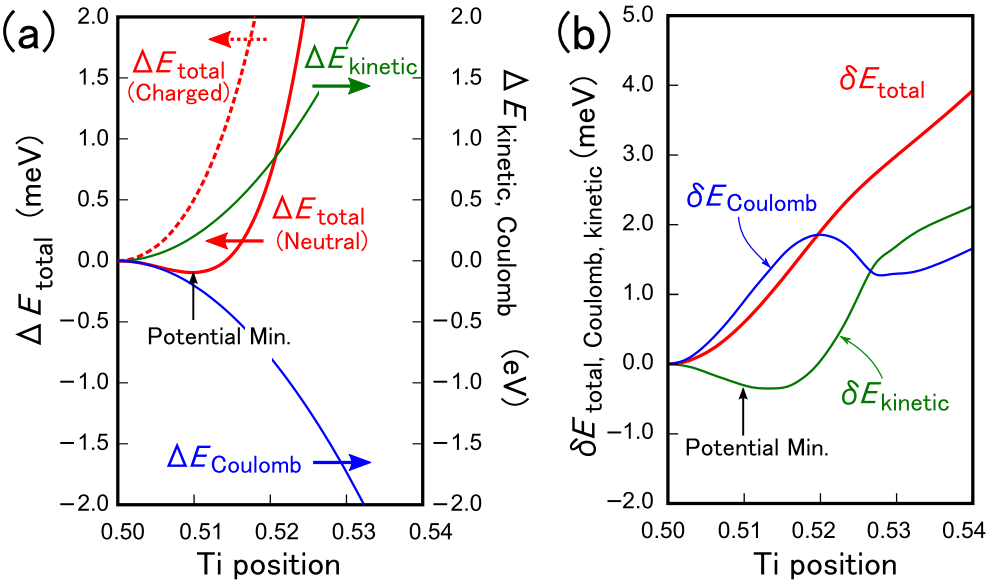

Figure 5.5: (a) $\Delta E_{\text{total (Neutral)}}$ is ferroelectric deformation potential that is total energy differences as a function of soft-mode displacement in charge neutral $BaTiO_3$. $\Delta E_{\text{kinetic}}$ and $\Delta E_{\text{Coulomb}}$ are kinetic and Coulomb energy contributions to $\Delta E_{\text{total (Neutral)}}$, respectively. $\Delta E_{\text{total (Charged)}}$ is the result for $BaTiO_3$ doped at 0.15 e/(unit cell). All values are set to zero at Ti position = 0.50. (b) Contribution of kinetic ($\delta E_{\text{kinetic}}$) and Coulomb ($\delta E_{\text{Coulomb}}$) energy terms to the change in the deformation potential between charged and neutral states (δE_{total})

The DFT total energy E_{total} can be divided into two parts:

$$E_{\text{total}} = E_{\text{kinetic}} + E_{\text{Coulomb}}, \tag{5.1}$$

$$E_{\text{kinetic}} = \sum_{n\mathbf{k}} \langle \phi_{n\mathbf{k}} | -\frac{1}{2}\Delta | \phi_{n\mathbf{k}} \rangle, \tag{5.2}$$

$$E_{\text{Coulomb}} = E_{\text{Hartree}} + E_{\text{xc}} + E_{\text{ext}} + E_{\text{Ewald}}, \tag{5.3}$$

where E_{kinetic} is kinetic energy denoted by Eq. (5.2) and E_{Coulomb} is Coulomb energy composed of Hartree (E_{Hartree}), exchange-correlation (E_{xc}), external (E_{ext}) and Ewald (E_{Ewald}) energies, as shown by Eq. (5.3). The contributions of the kinetic ($\Delta E_{\text{kinetic}}$) and Coulomb ($\Delta E_{\text{Coulomb}}$) energies to the ferroelectric deformation potential ΔE_{total} that is the energy gain due to soft-mode atomic displacement [90] is evaluated, and the results are shown in Fig. 5.5. Fig. 5.5(a) indicates that the local minimum in ΔE_{total} that induces ferroelectric deformation arises from the stronger energy gain in $\Delta E_{\text{Coulomb}}$ com-

pared to that in $\Delta E_{\text{kinetic}}$, which indicates that the Coulomb energy favors the ferroelectric deformation in $BaTiO_3$, as expected from previous model calculations [49, 154]. The potential depth of ΔE_{total} at the local minimum is about two orders of magnitude smaller than the variations in $\Delta E_{\text{Coulomb}}$ or $\Delta E_{\text{kinetic}}$, which indicates that the ferroelectric deformation is based on a very delicate balance between the Coulomb- and the kinetic-energy contributions to the total energy.

The local minimum in ΔE_{total} disappears when electrons are introduced into the lattice, as shown in Fig. 5.5(a) (dashed line); that is, T-C phase transition occurs due to the electron doping. We divide the total energy difference $\delta E_{\text{total}} = \Delta E_{\text{total (charged)}} - \Delta E_{\text{total (neutral)}}$ into Coulomb ($\delta E_{\text{Coulomb}}$) and kinetic ($\delta E_{\text{kinetic}}$) parts and individually evaluate each contribution to δE_{total} to clarify the contribution of the kinetic and Coulomb energies to the disappearance of the local minimum in ΔE_{total}. The results shown in Fig. 5.5(b) indicate that electron doping mainly increases $\delta E_{\text{Coulomb}}$, which implies that screening of the Coulomb energy induced by doped carrier electrons crucially contributes to the disappearance of the ferroelectric lattice instability. The sharp increase in the kinetic energy around Ti position 0.525 would be related to the minimum distance allowed between ions, which is typically called Pauli repulsion. From the results obtained from the first-principles calculation, it is obvious that the ferroelectric phase of $BaTiO_3$ is stabilized by the Coulomb energy contributions, which is consistent with the speculation from classical model simulation (long-range Coulomb energy favors ferroelectric distortion, whereas shot-range repulsions stabilize the cubic phase [49, 154]). The effects of the electron doping in ferroelectric phase $BaTiO_3$ is the weakening of the Coulomb energy contributions by screening the Coulomb forces, which results in the disappearance of the ferroelectric phase in $BaTiO_3$.

5.4 Defect-induced phase transition

We further performed supercell calculations to clarify the role of the lattice disorder induced by donor-type defect and dopant in doping-induced T-C phase transition. Several defect species are considered in our calculations: Nb^{5+}, oxygen vacancy (V_O^{2+}) and hydrogen at oxygen site (H_O^+) as typical donor-type defect species. The range of dopant concentration was varied by changing the supercell size and geometry as shown in Fig. 5.6. The concentration of defect species rages from $n_{\text{defect}} = 0.0185$ to 0.125 per unit cell as explained in Table 5.1. The accuracy of the k-point sampling grids is maintained as same as $8 \times 8 \times 8$ for unit cell, which enables us to compare

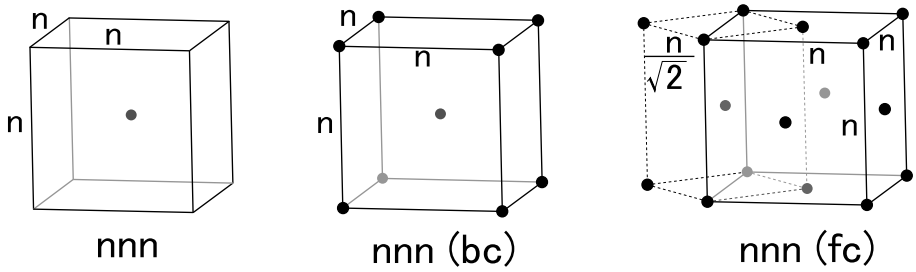

Figure 5.6: Supercell models composed of $n \times n \times n$ $BaTiO_3$ unit cells used in the defect calculations. The notations bc (body center) and fc (face center) denote the defect positions within the supercells. Primitive cells are adopted in the calculations with fc and bc supercells.

the effects of dopant-induced lattice disorder and electron doping on the ferroelectric displacement of $BaTiO_3$ shown in Fig. 5.1. We also confirmed that reduction of the k-point grids down to the accuracy of $6 \times 6 \times 6$ have little influence on the obtained results, which indicates the strong influence of the lattice disorder on the ferroelectric displacements.

The change in the c/a ratio induced by Nb doping at Ti site in $BaTiO_3$ is shown in Fig. 5.7(a). Generally, Nb is considered to be Nb^{5+} occupying Ti^{4+} site, therefore the number of carrier electrons is equal to the concentration of doped Nb^{5+} [80, 82]. We confirmed that the band structure of an Nb-doped supercell calculated with LDA agrees with this commonly accepted viewpoint. In Fig. 5.7(a), the c/a ratio decreases faster than that in the electron-only calculation. The critical-electron concentration for Nb^{5+} doping is $n_{\mathrm{Nb}} \approx 0.05$ e/(unit cell) (8.1×10^{20} cm^{-3}), which is about one half the critical concentration of pure electron only doping. In terms of the lattice deformation, the larger ionic radius of Nb^{5+} compared with that of Ti^{4+} is responsible for the rapid reduction of the c/a ratio, which is confirmed by the smaller local c/a ratio around the Nb^{5+} dopant shown at position A in Fig.

Table 5.1: Defect concentrations with the supercell models shown in Fig. 5.6.

Supercell	Atom number	Concentration (/(unit cell))
222	40	0.1250
444 (fc)	80 (primitive)	0.0625
333	135	0.0370
444 (bc)	160 (primitive)	0.0313
666 (fc)	260 (primitive)	0.0185

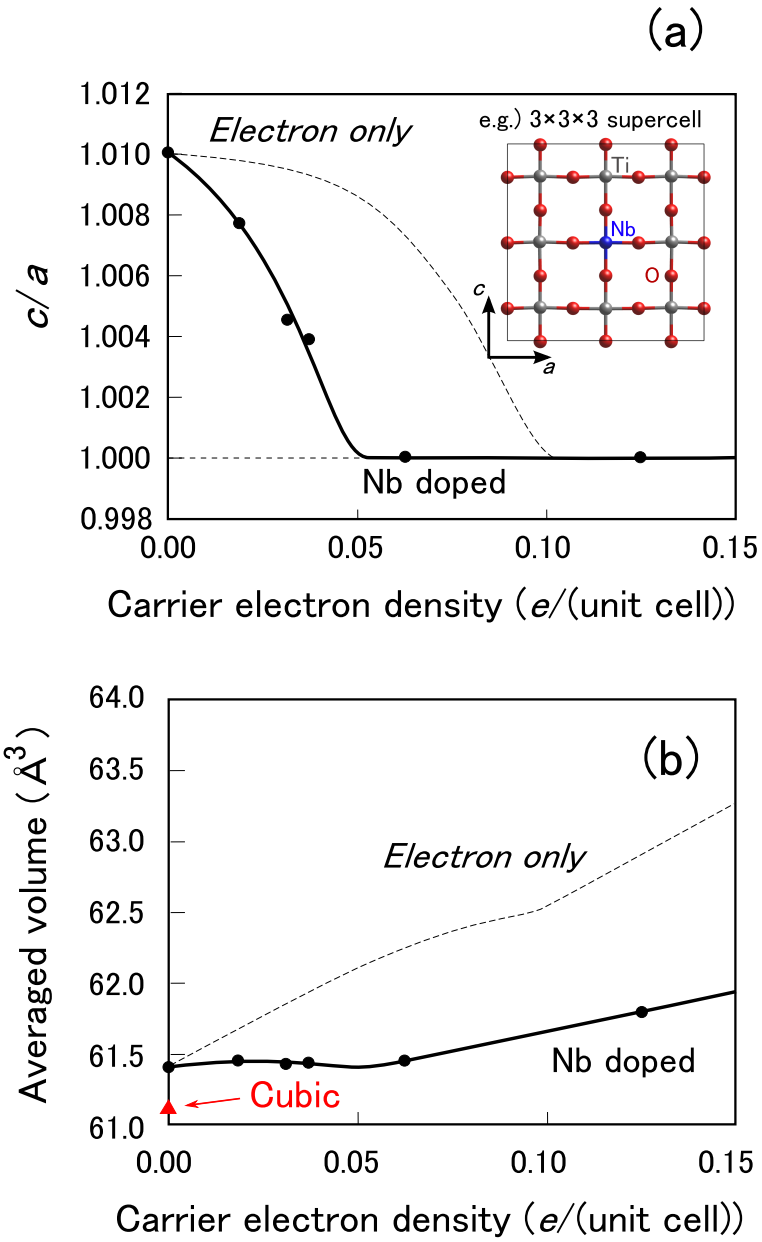

Figure 5.7: (a) The change of c/a ratio induced by Nb^{5+} doping at Ti^{4+} site in $BaTiO_3$. The inset shows the position of doped Nb atom in $3 \times 3 \times 3$ supercell model. (b) The changes in averaged volume induced by Nb doping. The averaged volume is obtained by dividing the supercell volume by the number of unitcells within the supercells.

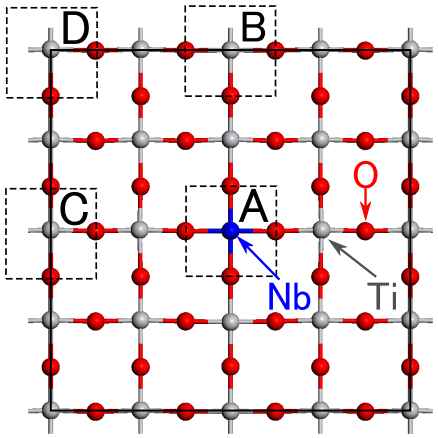

Position	c/a	Volume(Å^3)
A	1.002	61.92
B	1.007	61.29
C	1.003	61.34
D	1.005	61.19

Figure 5.8: c/a ratios and unit cell volumes at local positions A, B, C, and D in the cross-sectional view of the relaxed supercell that contains Nb^{5+}. The supercell size is 444 (bc), which corresponds to a Nb^{5+} concentration of 0.031 per unit cell.

5.8. Figure 5.7(b) shows the changes in the averaged volume obtained by dividing the supercell volume by the number of unit cells within the supercells. An unexpected finding is that the averaged volume of the Nb-doped supercell increases slower than that found in the electron-only calculation, despite the large ionic radius of the incorporated Nb^{5+} dopant. This result can be understood from the change in local unit cell volumes in Fig. 5.8. Even though the local unit cell volume around the Nb^{5+} impurity is sufficiently large (61.92 Å^3 at position A) reflecting the large ionic size of Nb^{5+}, local volumes far from Nb^{5+} (61.19 Å^3 at position D) are even smaller than the calculated volume of the perfect tetragonal $BaTiO_3$ (61.40 Å^3). The behavior of volume change is intrinsic to the phase transition of $BaTiO_3$. The thermal expansion coefficient of $BaTiO_3$ decreases sharply at each phase transition temperature from lower- to higher-symmetry phases [58], which indicates that the volumes of the higher-temperature phases are intrinsically smaller than those of the lower-temperature phases at least near phase transition temperatures. The tendency is also confirmed in in our calculations; the unit cell volume of C phase is smaller than that of T phase, as plotted in Fig. 5.7(b), reflecting the nature of the phase transition in $BaTiO_3$. Therefore, the averaged volumes tend to become smaller when the phase transition to C phase becomes faster as the increase of the electron concentrations. The calculated volume changes of Nb doped supercell agree well with previous experiments with $BaTi_{0.875}Nb_{0.125}O_3$ (BTNO) [82], where the crystal struc-

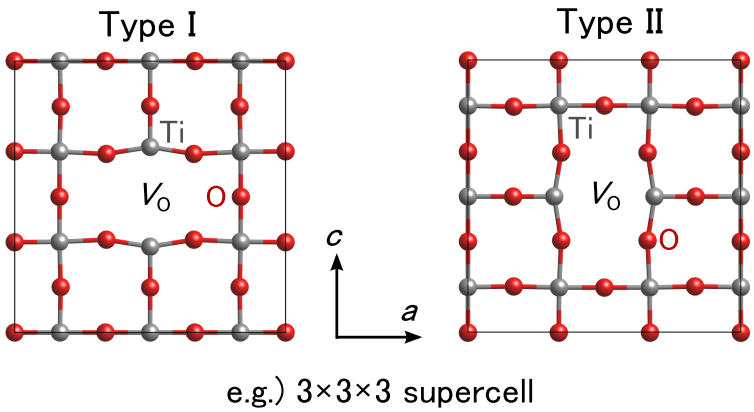

Figure 5.9: Supercell models of $BaTiO_3$ with oxygen vacancy at different symmetry sites denoted with V_O type I and II.

ture is cubic ($Pm3m$) at room temperature with a small expansion of the cell parameter and the cubic phase remains down to 15 K.

As a different types of donor-type defects, we calculated the effects of oxygen vacancies on the T-C phase transition in $BaTiO_3$. There are no in-gap states from oxygen vacancies in LDA (and also in GGA) calculations, which indicates that the vacancies are in a doubly charged state (V_O^{2+}). As explained in Chap. 3, the stable valence state of the oxygen vacancy is consistent with the results of HSE calculations; therefore, we assume here that two electrons are released from a V_O^{2+} vacancy. Due to the $P4mm$ crystal symmetry of the tetragonal phase $BaTiO_3$, there are two different equivalent oxygen positions in the T-phase $BaTiO_3$, which are denoted by O_I and O_{II} in Fig. 5.1(a), respectively. Therefore, two different types of supercell should be included in the same oxygen vacancy concentrations as shown by V_O type I and II shown in Fig. 5.9. The optimized crystal structures are shown in the Fig. 5.9, which indicates that the two adjacent Ti atoms around V_O^{2+} move away from each other. Due to the characteristic shifts of the two Ti cations around V_O as shown in Fig. 5.9, the lattice of the supercell is elongated in the direction of the shift of the two Ti atoms. As a result, the c/a ratio for V_O^{2+} type I does not decrease monotonically, but begins to increase around carrier electron concentrations greater than 0.06 e/(unit cell) as shown in the inset of Fig. 5.10(a). On the other hand, the c/a ratio of V_O^{2+} type II becomes less than 1 around the same carrier concentration, which means that the a axis replaces c axis as the longest axis due to the strong lattice disorder around V_O^{2+}. In terms of the formation energies, we found that the V_O^{2+} type I vacancy is slightly more stable than V_O^{2+} type II vacancy, but the

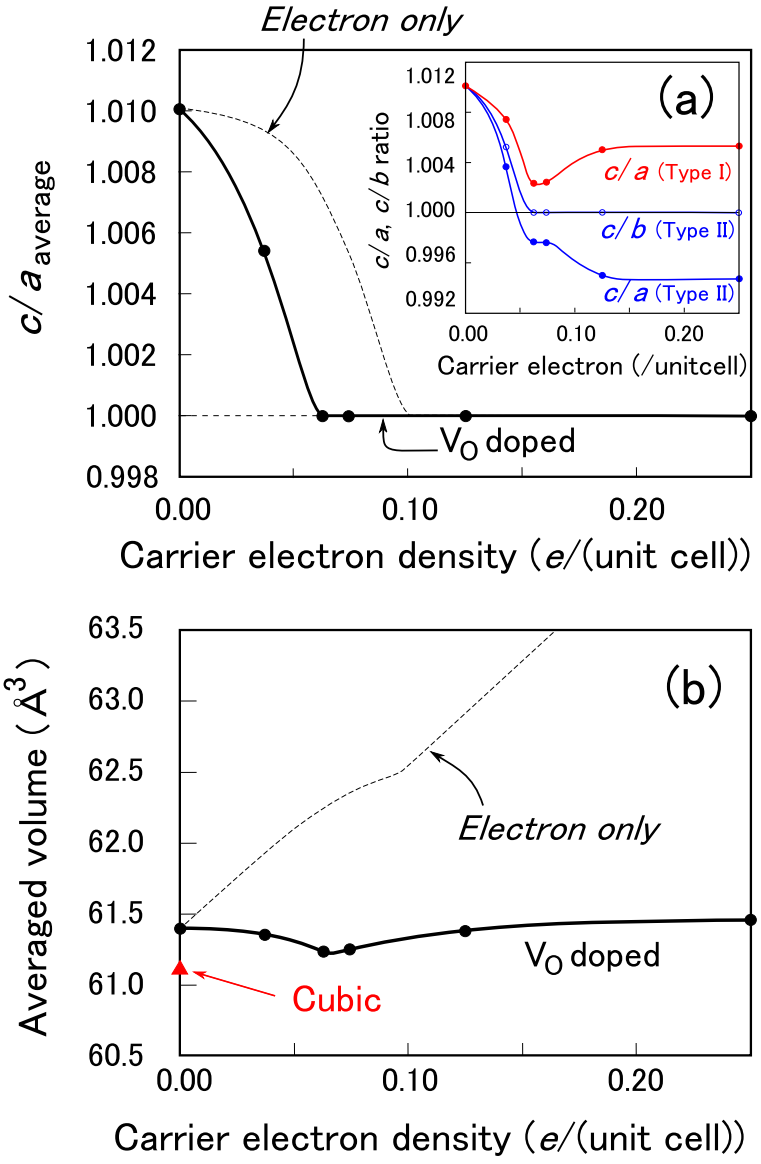

Figure 5.10: (a) The change of c/a ratio induced by V_O^{2+} doping in $BaTiO_3$. The inset shows the effects of V_O^{2+} at different positions (Type I and II). (b) The changes in averaged volume induced by V_O^{2+} doping. The averaged volume is obtained by dividing the supercell volume by the number of unitcells within the supercells.

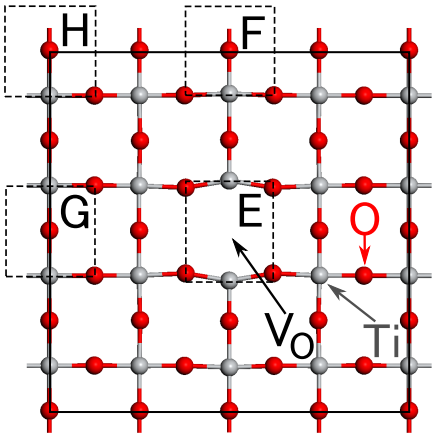

Type I

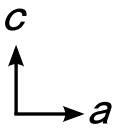

Type II

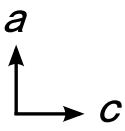

Position	c/a	Volume(Å^3)
E	1.151	63.90
F	0.971	58.36
G	0.999	61.91
H	1.002	61.51

Figure 5.11: c/a ratios and unit cell volumes at different local positions denoted with E, F,G and H in the relaxed structure of 444 (bc) supercell with V_O^{2+} type I vacancy.

difference of the total energies between these two oxygen vacancies is about two orders of magnitude smaller than the calculated formation energies of the oxygen vacancy (6.3−5.3 eV, depending on the supercell size of 39−259 atoms). Consequently, we can assume the uniform distribution of V_O^{2+} type I and II vacancies in T phase $BaTiO_3$. We adopted a simple average of the c/a ratio to approximate the uniform distribution of two types of oxygen vacancies: $c/a_{\text{average}} = (c/a_{\text{type I}} + c/a_{\text{type II}} + c/b_{\text{type II}})/3$. The change in the average tetragonality c/a_{average} is shown in Fig. 5.10(a), which indicates that the critical-electron concentration where the tetragonal distortion disappears is 0.06 e/(unit cell) (9.8 $\times 10^{20}$ cm^{-3}). On the other hand, the average unit cell volume remains almost constant independent of the V_O^{2+} concentration, as shown in Fig. 5.10(b). Although the local unit cell volume around V_O^{2+} increases significantly as shown at position E in Fig. 5.11, decreases in volume at other areas far from the vacancy counteract the increase of the total supercell volume, which results in almost no increase in the oxygen incorporated supercell volumes. A sharp decrease in volume at the critical-charge density is a sign of T-C phase transition, because the volume of C phase is intrinsically smaller than the T phase.

In Chap. 4, we explained the importance of the hydride ion (H^-) that occupies oxygen site in $BaTiO_3$, which results in the formation of H_O^+. Even though the H_O^+ has hardly been discussed in previous studies, our results clearly show that this is one of major defect species in reduced $BaTiO_3$ fabricated under H_2 gas annealing. Therefore, we calculated the effects of H_O^+

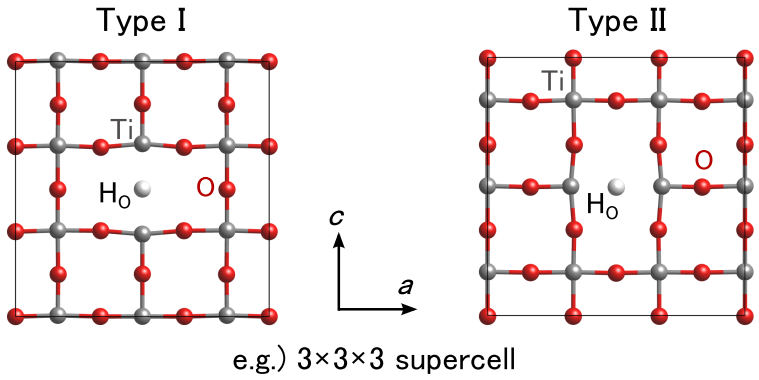

Figure 5.12: Supercell models of $BaTiO_3$ with H_O at different symmetry sites denoted with H_O type I and II.

on the ferroelectric tetragonal phase of $BaTiO_3$. Since the possible crystallographic site of H_O in $BaTiO_3$ tetragonal phase is identical to that of oxygen vacancy, there are two equivalent positions of H_O similar to that of the oxygen vacancy. Figure 5.12 shows the supercell models with H_O type I and II. Compared to the lattice deformation induced by V_O, the deformation induced by H_O is slightly smaller, which indicates that the H_O corrects the lattice deformation induced by V_O. The inset in Fig. 5.13(a) shows the changes in tetragonality induced by H_O^+ type I and II. As explained for the V_O, the lattice of the supercell is elongated in the direction of Ti-H-Ti atom arrangement; therefore, the change of the c/a ratio is very similar to that of V_O shown in the inset of Fig. 5.10(a). The main difference between the V_O^{2+} and H_O^+ is the stable valence state of the defect species. In addition, the smaller lattice deformation around H_O compared to V_O permits the existence of the ferroelectric phase in $BaTiO_3$ under high concentration of H_O. As a consequence, much higher concentration of H_O (0.05 /(unit cell)) is allowed in the ferroelectric phase of $BaTiO_3$ compared to V_O (0.03/(unit cell)) as shown in Fig. 5.13. On the other hand, the critical carrier electron density induced by H_O is 0.05 e/(unit cell) (8.2×10^{20} cm^{-3}), which is very close to the critical density induced by Nb^{5+} at Ti^{4+} site and V_O^{2+}.

The Nb^{5+}, V_O^{2+} and H_O^+ doped supercell calculations show that the dopant-induced lattice disorder reduces the critical-electron concentration where the T phase vanishes in $BaTiO_3$. Although the critical-electron concentrations in $BaTiO_3$ induced by donor-dopants are very similar [0.05-0.06 e/(unit cell)], the concentration of V_O^{2+} for the phase transition (0.03 e/(unit cell)) is much smaller than that of Nb^{5+} and H_O^+ (0.05 e/(unit cell)). The oxygen vacancy strongly perturbs the $BaTiO_3$ lattice, as shown in Fig. 5.11, which causes

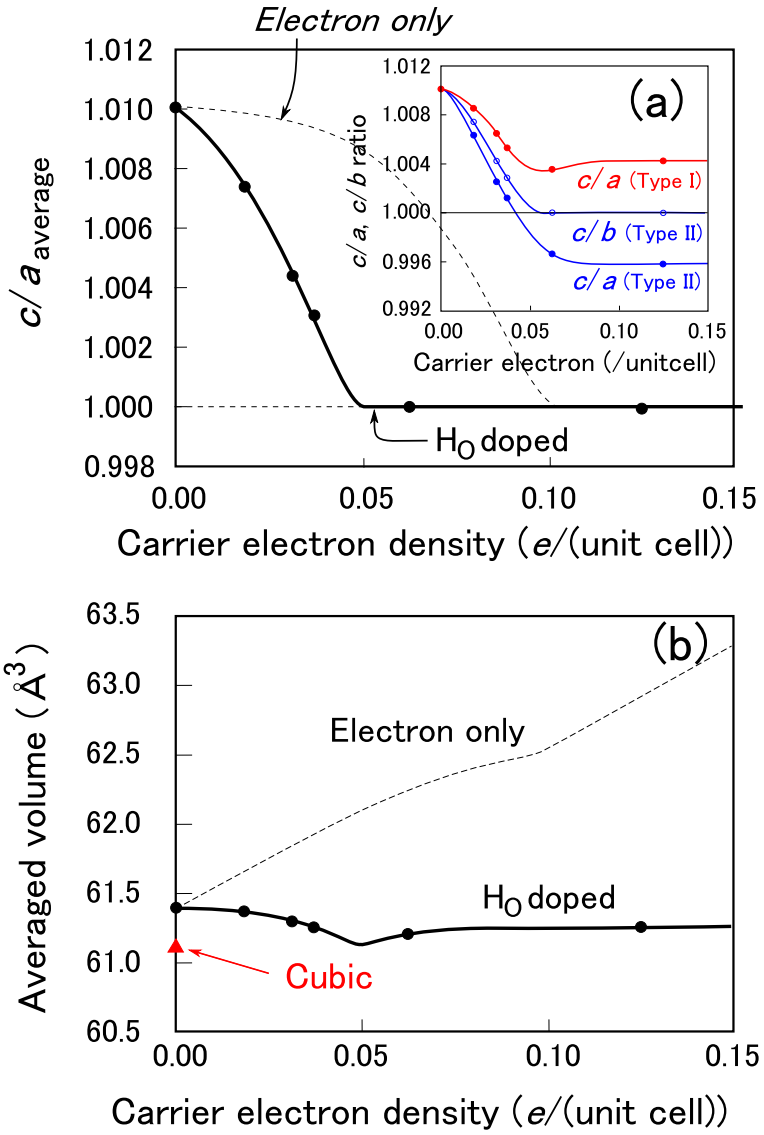

Figure 5.13: (a) The change of c/a ratio induced by H_O^+ doping in $BaTiO_3$. The inset shows the effects of H_O^+ at different positions (Type I and II). (b) The changes in averaged volume induced by H_O^+ doping. The averaged volume is obtained by dividing the supercell volume by the number of unitcells within the supercells.

phase transition at a lower concentration compared to other dopants.

The calculated critical-electron density for the $V_{\rm O}^{2+}$ supercell is 0.06 e/(unit cell) (9.8 $\times 10^{20}$ cm^{-3}), which is about a half the experimental value for reduced $BaTiO_{3-\delta}$ (1.9 $\times 10^{21}$ cm^{-3}) [78]. Even if we suppose the possibility that the experimental carrier-electron doping is achieved by $H_{\rm O}^{+}$, the difference is too large to be explained by the $H_{\rm O}^{+}$. We should carefully reconsider the difference between the theoretical and experimental results. In Ref. [78], the experimental critical density was evaluated from changes in phase transition temperature caused by $V_{\rm O}^{2+}$ (or $H_{\rm O}^{+}$). In these experiments, the critical-electron density should be the electron concentration where all ferroelectric phases disappear. However, there is a serious problem in actual experiments that the critical-electron density is difficult to be achieved due to the irreversible transformation into hexagonal polymorph caused by $V_{\rm O}$ in heavily reduced $BaTiO_{3-\delta}$ [78]. Therefore, the electron density reported in Ref. [78] is evaluated from a linear extrapolation of the C-T transition temperature around very low electron concentrations (1.0-3.5 $\times 10^{20}$ cm^{-3}). However, there is no guarantee that the phase transition temperature decreases in proportion to electron concentration within such a wide range of electron doping. The disappearance of the ferroelectric distortion shown in Fig. 5.1 is definitely not proportional to electron concentration, which suggests that more higher-order fitting is required to evaluate the critical-electron density. Therefore, the experimental critical density should be much smaller than the reported value.

5.5 Summary

The effect of electron doping on the disappearance of the ferroelectric phase, namely the low- to high-symmetry phase transition in $BaTiO_3$ was studied with first-principles calculation. From the calculation with electron doping with uniform-background charge, the disappearance of the ferroelectric phase is shown to be an intrinsic nature of electron doping in $BaTiO_3$. The critical-electron concentration for the T-C phase transition with pure-electron doping is calculated to be $n_{\rm elec.} = 0.085\ e$/(unit cell)$(1.36 \times 10^{21}$ cm$^{-3})$. The component analysis for the total energy shows that the screening of the Coulomb energy by carrier electrons is a main factor behind the disappearance of the ferroelectric lattice instability. Furthermore, we performed calculations to clarify the effects of lattice deformation due to typical donor dopants Nb^{5+}, $V_{\rm O}^{2+}$ and $H_{\rm O}^{+}$ with supercell models containing these defect structures. The series of calculations clarified that that dopant-induced lattice disorder accelerates the disappearance of the ferroelectric distortion in $BaTiO_3$ and the

critical-electron concentration becomes about one half the critical concentration of the pure electron doping. Interestingly, the calculated critical electron densities with Nb^{5+}, V_O^{2+} and H_O^+ defect structures is 0.05-0.06 e/(unit cell) ($8.2 - 9.8 \times 10^{20}$ cm^{-3}), which is about one half the experimental value [78]. This result suggests that more detailed research is necessary, including an experimental procedure to determine the critical electron density.

Chapter 6

Concluding remarks

6.1 Summary of the thesis

In this thesis, we have investigated the nature of defects and impurities in perovskite-type $A\mathrm{TiO}_3$ (A = Sr, Ba) oxides based on the first-principles calculation. The aim of our study is the clarification of various experimental results observed in reduced $A\mathrm{TiO}_3$ with hydrogen gas (H_2). The essential problem in the theoretical calculation is the difficulty of the accurate evaluation of shallow donor states in wide-gap insulators, which is a very hard task for current first-principles calculation based on density functional theory (DFT). We introduced several improved exchange-correlation (XC) functionals: DFT+U, pseudo SIC, and hybrid functional to overcome the problems in local density approximation (LDA). In Chap. 2, theoretical framework of these improved XC functionals are explained followed by a derivation of Kohn-Sham equations. One of serious drawbacks of LDA is the underestimation of band gap, and the mechanism of the improvement of the gap value due to these improved XC functionals are discussed.

For the evaluation of defects in perovskite-type oxides, our first subject is the selection of appropriate XC functional suitable for these calculations. We took up an isolated oxygen vacancy (V_O) in $\mathrm{SrTiO}_{3-\delta}$ as a typical shallow-donor defect, and performed a series of calculations with various XC functionals (Chap. 3). As a result, we found that the defect state of V_O depends not only on the XC functional but also on the atomic configuration around the V_O, which suggests the importance of the geometry optimization around the vacancy. Considering the requirements for the defect-state calculations, we concluded that the hybrid functional especially HSE would be a reasonable choice for the calculations of defect and impurity in perovskite-type oxides. The HSE calculation indicates that V_O^{2+} is the stable valence state in SrTiO_3.

However, the result is inconsistent with the experimentally confirmed V_{O}^{+} stability in $A\mathrm{TiO}_3$. Thereby, we concluded that the experimentally confirmed V_{O}^{+} stability cannot be explained by a simple isolated V_{O} model in SrTiO_3 and another atomistic models are required.

We also investigated the effects of hydrogen (H) impurities on the electronic structure of perovskite-type oxides (Chap. 4). The H atom has been considered as proton (H^{+}) in this material group. Contrary to the previous general knowledge, we found that the H atom changes its character from H^{+} to H^{-} (negatively charged hydride) depending on the environment around H in $A\mathrm{TiO}_3$. The H^{-} in $A\mathrm{TiO}_3$ stably occupies V_{O}^{2+} site, which leads to the stable formation of $\mathrm{H}_{\mathrm{O}}^{+}$ defect species. Our results clearly suggest that the formation of $\mathrm{H}_{\mathrm{O}}^{+}$ is the cause of the apparent V_{O}^{+} stability in $A\mathrm{TiO}_3$ under hydrogen annealing condition. Our results also suggest that an additional H^{-} can be weakly trapped by $\mathrm{H}_{\mathrm{O}}^{+}$, which leads to the passivation for the Ti-3d dangling bonds. As a results, all carrier electrons from V_{O}^{2+} are trapped by a very deep bonding level composed of H-1s and Ti-3d, and the donor-like property of the oxygen vacancy is completely disappeared. Our results clearly show that the wide variety of H incorporations in oxygen deficient $A\mathrm{TiO}_{3-\delta}$ can greatly modify the carrier electron density. The H_2 gas is commonly used as a reducing agent for $A\mathrm{TiO}_3$, and many previous experiments assume a simple oxygen vacancy (V_{O}^{2+}) or interstitial hydrogen ($\mathrm{H}_{\mathrm{i}}^{+}$) as a source of carrier electron. Therefore, the hydrogen occupying the V_{O}^{2+} site as hydride (H^{-}) are extremely important, because it requires reconsideration for previous experiments, and contributes to the development of defect control in solid state materials.

We further clarified the effects of donor-type defects on the ferroelectricity in perovskite-type BaTiO_3 (Chap. 5). As a first step, we divided the effects of donor-defect incorporation into two aspects: pure electron doping and lattice deformation due to the defect, and evaluated each contribution to the disappearance of the ferroelectricity. We found that pure electron doping intrinsically suppress the ferroelectric phase of BaTiO_3 with critical carrier-electron density of $n_{\mathrm{elec.}} = 0.085\ e/(\text{unit cell})(1.36 \times 10^{21}\ \mathrm{cm}^{-3})$. From the component analysis of the total energy, we clarified that Coulomb energy favors the ferroelectric deformation, whereas kinetic energy favors non-ferroelectric lattices, and that the screening of the Coulomb force by the doped free electron is of essential importance for the disappearance of the ferroelectric phase in BaTiO_3. We explained that the component analysis can also explains the origin of the ferroelectricity. We further clarified that the lattice deformation due to the defects ($\mathrm{H}_{\mathrm{O}}^{+}$, V_{O}^{2+} and Nb^{5+}) accelerate the disappearance of the ferroelectricity and the critical carrier-electron concentration becomes almost a half value of that in pure electron doping.

6.2 Future work

In this thesis work, we studied the relation between macroscopic phenomena (conductivity, color, spontaneous polarization, etc.) and defect species generated under H_2 annealing for perovskite-type oxides. The defect species studied are mainly related with oxygen vacancy and hydrogen, and several unrevealed phenomena are clarified through the work. However, there are several experimental results that are still unclear, such as an annealing experiment for Nb doped $SrTiO_3$ single crystal, where the decrease of conductivity was observed by the hydrogen doping [71]. The experimental result obviously indicates that the hydrogen does not act as a donor-type impurity (H_i^+) in Nb doped $SrTiO_3$ and there would be another defect complex model that is different from the ones we discussed in this thesis. The clarification of the role of hydrogen in these complicated experimental results is an interesting subject as a future work of the thesis.

Appendix A

Appendix

A.1 USP formalism of pseudo SIC

We implemented the pseudo SIC method in a first-principle calculation code: *Tokyo ab initio programming package* (TAPP) that is an ultrasoft pseudo potential programing package. The formalism of the pseudo SIC explained in Chap. 2 is based on norm-conserving pseudo potential (NCP). However, we implemented with NCP and also with ultrasoft pseudo potential (USPP), and actual calculations are performed with the USPP implementation. In the appendix, we will explain the implementation of the pseudo SIC with the framework of the USPP.

The SIC-KS equations are written as follows:

$$[\hat{H}_{\mathrm{LDA}} - \hat{V}_{\mathrm{SIC}}] \, |\psi_{n,\mathbf{k}}\rangle = \varepsilon_{n,\mathbf{k}} \, |\psi_{n,\mathbf{k}}\rangle \, , \tag{A.1}$$

where, $\hat{V}_{\mathrm{SIC}}$ is the SIC operator. In NCP, it is expressed by:

$$\hat{V}_{\mathrm{SIC}} = \frac{1}{2} \sum_i \frac{|V_{\mathrm{HXC}}[n_i]\phi_i\rangle \, p_i \, \langle V_{\mathrm{HXC}}[n_i]\phi_i|}{\langle \phi_i | V_{\mathrm{HXC}} | \phi_i \rangle}, \tag{A.2}$$

where ϕ_i is wave function of isolated atom and $V_{\mathrm{HXC}}[n_i](r)$ is HXC potential calculated only from the density of isolated atom, and p_i is the occupation. In NCP, the p_i defined by:

$$p_i = \sum_{n,\mathbf{k}} f_{n,\mathbf{k}} \, \langle \psi_{n,\mathbf{k}} | \phi_i \rangle \, \langle \phi_i | \psi_{n,\mathbf{k}} \rangle \, , \tag{A.3}$$

whereas in USP, the p_i should be: [1]

$$p_i = \sum_{n,\mathbf{k}} f_{n,\mathbf{k}} \langle \psi_{n,\mathbf{k}} | \hat{S} | \phi_i \rangle \langle \phi_i | \hat{S} | \psi_{n,\mathbf{k}} \rangle \,, \tag{A.4}$$

where $\hat{S}$ is the overlap matrix defined by:

$$\hat{S} = 1 + \sum_{\tau,i,j} |\beta_i^\tau\rangle \, Q_{ij}^\tau \, \langle \beta_{ij}^\tau | \,. \tag{A.5}$$

The variation of SI energy E_{SIC} against Ψ^* is:

$$\begin{aligned} \frac{\delta E_{\mathrm{SIC}}[n_i]}{\delta \Psi_i^*} &= \frac{\delta E_{\mathrm{SIC}}[n_i]}{\delta n_i} \frac{\delta n_i}{\delta \Psi_i^*} \\ &= \frac{\delta E_{\mathrm{SIC}}[n_i]}{\delta n_i} (1 + \sum_{\tau,i,j} |\beta_i^\tau\rangle \, Q_{ij}^\tau \, \langle \beta_{ij}^\tau |) \, |\Psi_i\rangle \,, \end{aligned} \tag{A.6}$$

where the first term is (formally) describes SIC potential, and the second term is additional USP operator which are described by:

$$\hat{V}_{\mathrm{SIC}}^{\mathrm{US}} = \sum_i \frac{1}{2} p_i \sum_{\alpha\alpha'} |\beta_\alpha\rangle \left(\int d\mathbf{r} V_{\mathrm{HXC}}[n_i(\mathbf{r}); 1] Q_{\alpha\alpha'}(\mathbf{r}) \right) \langle \beta_{\alpha'} | \,. \tag{A.7}$$

The pseudo SIC KS equations are:

$$\begin{aligned} \hat{H}_{\mathrm{SIC,USP}} \, |\psi_{n\mathbf{k}}\rangle &= \left[-\frac{1}{2}\nabla^2 + \hat{V}_{\mathrm{loc}} + \hat{V}_{\mathrm{NL}} - \left(\hat{V}_{\mathrm{SIC}} + \hat{V}_{\mathrm{SIC}}^{\mathrm{US}} \right) \right] |\psi_{n\mathbf{k}}\rangle \\ &= \varepsilon_{n\mathbf{k}} \hat{S} \, |\psi_{n\mathbf{k}}\rangle \,. \end{aligned} \tag{A.8}$$

The form of the (approximated) total energy is:

$$\begin{aligned} E_{\mathrm{SIC}}[n,m] &= \sum_{i,\sigma} f_{n,\mathbf{k}}^\sigma \varepsilon_{n\mathbf{k}} \sigma - \sum_\sigma \int d\mathbf{r} n^\sigma(\mathbf{r}) V_{\mathrm{HXC}}^\sigma[n(\mathbf{r}), m(\mathbf{r})] \\ &+ E_{\mathrm{HXC}}[n,m] + E_{\mathrm{ion}} \\ &+ \sum_{n,\mathbf{k},\sigma} f_{n,\mathbf{k}}^\sigma \langle \psi_{n,\mathbf{k}}^\sigma | \hat{V}_{\mathrm{SIC}^\sigma} + \hat{V}_{\mathrm{SIC}}^{\sigma,\mathrm{US}} | \psi_{\mathrm{n,k}}^\sigma \rangle - \sum_{i,\sigma} E_{\mathrm{HXC}}[n_i^\sigma]. \end{aligned} \tag{A.9}$$

[1] The definition of the occupation in Eq. (A.4) is different from original paper by A. Filippetti, *et al.*, where they defined $p_i = \sum_{n\mathbf{k}} f_{n\mathbf{k}} \langle \Psi_{n\mathbf{k}} | \phi_i \rangle \langle \phi_i | \Psi_{n\mathbf{k}} \rangle \, S_{\mathrm{atom}}$, where S_{atom} is the expectation value of the overlap matrix calculated with atomic wave function: $S_{\mathrm{atom}} = 1 + \sum_{\alpha\alpha'} \langle \phi_i | \beta_\alpha \rangle \, Q_{\alpha\alpha'} \, \langle \beta_{\alpha'} | \phi_i \rangle$.

A.2 USP formalism of LDA+U

In our work, the LDA+U calculations are performed with USPP. Here, we briefly explain the basic formulation of LDA+U under USPP formalism.

The total energy functionals is:

$$E_{LDA+U} = E_{LDA} + E_U, \tag{A.10}$$

where E_U is the rotational invariant on-site correction:

$$\begin{aligned} E_U[\{n^{\tau'\sigma}_{mm'}\}] &= \frac{U_{eff}}{2}\sum_{\tau'}\sum_{m\sigma}\left\{n^{\tau'\sigma}_{mm} - \sum_{m'} n^{\tau'\sigma}_{mm'}n^{\tau'\sigma}_{m'm}\right\} \\ &= \frac{U_{eff}}{2}\sum_{\tau'\sigma} Tr[\mathbf{n}^{\tau'\sigma}\left(1-\mathbf{n}^{\tau'\sigma}\right)]. \end{aligned} \tag{A.11}$$

$\mathbf{n}^{\tau'\sigma}$ is occupation matrix (on-site density matrix) defined as

$$n^{\tau'\sigma}_{mm'} = \sum_{n,\mathbf{k}} f_{n,\mathbf{k}}\langle\psi^{\sigma}_{n,\mathbf{k}}|\hat{S}'|\Phi^{\tau'}_{m}\rangle\langle\Phi^{\tau'}_{m'}|\hat{S}'|\psi^{\sigma}_{n,\mathbf{k}}\rangle, \tag{A.12}$$

where $\hat{S}'$ is overlap operator defined for localized (atomic) orbitals $\Phi^{\tau'}_m$, and we can select $\hat{S}' = \hat{S}$ when we recalculate the $\Phi^{\tau'}_m$ using Vanderbilt USP with overlap operator $\hat{S}$. $\psi_{n,\mathbf{k}}$ are the pseudo-wave functions and $f_{n,\mathbf{k}}$ are the occupation numbers.

Derivative of E_U by $\psi^{\sigma*}_{n,\mathbf{k}}$ is

$$\begin{aligned} \frac{\partial E_U}{\partial\psi^{\sigma*}_{n,\mathbf{k}}} &= \frac{U_{eff}}{2}\frac{\partial}{\psi^{\sigma*}_{n,\mathbf{k}}}\sum_{\tau'}\sum_{m\sigma}\left\{n^{\tau'\sigma}_{mm} - \sum_{m'} n^{\tau'\sigma}_{mm'}n^{\tau'\sigma}_{m'm}\right\} \\ &= \frac{U_{eff}}{2}\sum_{\tau' m}\left\{\frac{\partial n^{\tau'\sigma}_{mm}}{\psi^{\sigma*}_{n,\mathbf{k}}} - \frac{\partial}{\psi^{\sigma*}_{n,\mathbf{k}}}\sum_{m'} n^{\tau'\sigma}_{mm'}n^{\tau'\sigma}_{m'm}\right\}. \end{aligned} \tag{A.13}$$

First and second term in Eq.(A.13) becomes

$$\begin{aligned} \sum_{\tau',m}\frac{\partial n^{\tau'\sigma}_{mm}}{\psi^{\sigma*}_{n,\mathbf{k}}} &= \sum_{\tau',m}\frac{\partial}{\psi^{\sigma*}_{n,\mathbf{k}}}\sum_{n,\mathbf{k}} f_{n,\mathbf{k}}\langle\psi^{\sigma}_{n,\mathbf{k}}|\hat{S}|\Phi^{\tau'}_{m}\rangle\langle\Phi^{\tau'}_{m}|\hat{S}|\psi^{\sigma}_{n,\mathbf{k}}\rangle \\ &= \sum_{\tau',m}\hat{S}|\Phi^{\tau'}_{m}\rangle\langle\Phi^{\tau'}_{m}|\hat{S}|\psi^{\sigma}_{n,\mathbf{k}}\rangle, \end{aligned} \tag{A.14}$$

$$\sum_{\tau',m}\frac{\partial}{\partial\psi^{\sigma*}_{n,\mathbf{k}}}\sum_{m'}n^{\tau'\sigma}_{mm'}n^{\tau'\sigma}_{m'm} = \sum_{\tau',m}\sum_{m'}\left(\frac{\partial n^{\tau'\sigma}_{mm'}}{\partial\psi^{\sigma*}_{n,\mathbf{k}}}n^{\tau'\sigma}_{m'm}+n^{\tau'\sigma}_{mm'}\frac{\partial n^{\tau'\sigma}_{m'm}}{\partial\psi^{\sigma*}_{n,\mathbf{k}}}\right)$$
$$= 2\sum_{\tau',m}\sum_{m'}n^{\tau'\sigma}_{mm'}\frac{\partial n^{\tau'\sigma}_{m'm}}{\partial\psi^{\sigma*}_{n,\mathbf{k}}}$$
$$= 2\sum_{\tau',m}\sum_{m'}\hat{S}|\Phi^{\tau'}_{m'}\rangle n^{\tau'\sigma}_{mm'}\langle\Phi^{\tau'}_{m}|\hat{S}|\psi^{\sigma}_{n,\mathbf{k}}\rangle. \quad \text{(A.15)}$$

Hence, the potential $\hat{V}^{\sigma}_{U}$ acting on KS equations is

$$\hat{V}^{\sigma}_{U}=\frac{U_{eff}}{2}\sum_{\tau'}\left(\sum_{m}\hat{S}|\Phi^{\tau'}_{m}\rangle\langle\Phi^{\tau'}_{m}|\hat{S}-2\sum_{mm'}\hat{S}|\Phi^{\tau'}_{m'}\rangle n^{\tau'\sigma}_{mm'}\langle\Phi^{\tau'}_{m}|\hat{S}\right). \quad \text{(A.16)}$$

where, the overlap operator $\hat{S}$ is:

$$\hat{S} = 1+\sum_{\tau',ij}|\beta^{\tau'}_{i}\rangle Q^{\tau'}_{ij}\langle\beta^{\tau'}_{j}|. \quad \text{(A.17)}$$

Bibliography

[1] R. Wahl, D. Vogtenhuber, and G. Kresse, Phys. Rev. B **78**, 104116 (2008).

[2] M. Ohno and K. Takagi, Appl. Phys. Lett. **64**, 1620 (1994).

[3] K. Bhattacharya and G. Ravichandran, Acta Materialia **51**, 5941 (2003).

[4] H.-K. Guo, G. Fu, X.-G. Tang, J.-X. Zhang, and Z.-X. Chen, J. Phys. Condens. Matter **10**, L297 (1998).

[5] a. Bartasyte, V. Plausinaitiene, A. Abrutis, T. Murauskas, P. Boulet, S. Margueron, J. Gleize, S. Robert, V. Kubilius, and Z. Saltyte, Appl. Phys. Lett. **101**, 122902 (2012).

[6] H. Kishi, Y. Mizuno, and H. Chazono, Jpn. J. Appl. Phys. **42**, 1 (2003).

[7] D. Dimos and C. Mueller, Annu. Rev. Mat. Sci. , 397 (1998).

[8] R. Byer, IEEE Journal of Selected Topics in Quantum Electronics **6**, 911 (2000).

[9] Y. Fainman, J. Ma, and S. Lee, Mater. Sci. Reports **9**, 53 (1993).

[10] F. Jona, G. Shirane, and R. Pepinsky, Phys. Rev. **9** (1955).

[11] K. Kreuer, Annu. Rev. Mater. Res. **33**, 333 (2003).

[12] N. Q. Minh, J. Am. Ceram. Soc. **76**, 563 (1993).

[13] H. Iwahara, J. Electrochem. Soc. **135**, 529 (1988).

[14] H. Iwahara, H. Uchida, and J. Kondo, J. Appl. Electrochem. **13**, 365 (1983).

[15] H. J. Bouwmeester, Catalysis Today **82**, 141 (2003).

[16] K. Huang, J. Electrochem. Soc. **144**, 3620 (1997).

[17] J. Mizusaki, J. Electrochem. Soc. **136**, 2082 (1989).

[18] R. Mukundan, P. K. Davies, and W. L. Worrell, J. Electrochem. Soc. **148**, A82 (2001).

[19] J. M. D. Teresa, M. R. Ibarra, P. A. Algarabel, C. Ritter, C. Marquina, J. Blasco, J. García, A. del Moral, and Z. Arnold, Nature **386**, 256 (1997).

[20] S. Jin, T. Tiefel, and M. McCormack, Science **264**, 413 (1994).

[21] Y. Takada, J. Phys. Soc. Jpn. **49**, 1267 (1980).

[22] J. Bednorz and K. Müller, Rev. Mod. Phys. **60**, 585 (1988).

[23] T. Fukui, S. Ohara, and S. Kawatsu, J. Power Sources **71**, 164 (1998).

[24] J. Ihringer, J. K. Maichle, W. Prandl, A. W. Hewat, and T. Wroblewski, Zeitschrift für Physik B Condensed Matter **82**, 171 (1991).

[25] L. Li, Mater. Sci. Eng.: R: Reports **29**, 153 (2000).

[26] C. S. Koonce, M. L. Cohen, J. F. Schooley, W. R. Hosler, and E. R. Pfeiffer, Phys. Rev. **163**, 380 (1967).

[27] L. Forni and I. Rossetti, App. Cataly. B: Environment. **38**, 29 (2002).

[28] R. Spinicci, A. Tofanari, A. Delmastro, D. Mazza, and S. Ronchetti, Mater. Chem. Phys. **76**, 20 (2002).

[29] A. Okazaki and M. Kawaminami, Mater. Res. Bull. **8**, 545 (1973).

[30] W. Luo, W. Duan, S. Louie, and M. Cohen, Phys. Rev. B **70**, 1 (2004).

[31] R. Moos, W. Menesklou, and K. Härdtl, Appl. Phys. A **61**, 389 (1995).

[32] W. Gong, H. Yun, Y. Ning, J. Greedan, W. Datars, and C. Stager, J. Sol. State Chem. **90**, 320 (1991).

[33] K. Szot, W. Speier, R. Carius, U. Zastrow, and W. Beyer, Phys. Rev. Lett. **88**, 075508 (2002).

[34] A. Walsh, C. R. A. Catlow, A. G. H. Smith, A. A. Sokol, and S. M. Woodley, Phys. Rev. B **83**, 220301 (2011).

[35] D. Kan, T. Terashima, R. Kanda, A. Masuno, K. Tanaka, S. Chu, H. Kan, A. Ishizumi, Y. Kanemitsu, Y. Shimakawa, and M. Takano, Nature Mater. **4**, 816 (2005).

[36] J. Buban, H. Iddir, and S. Öğüt, Phys. Rev. B **69**, 180102 (2004).

[37] N. Sai and D. Vanderbilt, Phys. Rev. B **62**, 13942 (2000).

[38] K. Uchida, S. Tsuneyuki, and T. Schimizu, Phys. Rev. B **68**, 174107 (2003).

[39] E. Sawaguchi, A. Kikuchi, and Y. Kodera, J. Phys. Soc. Jpn. **17**, 1666 (1962).

[40] W. Zhong and D. Vanderbilt, Phys. Rev. B **53**, 5047 (1996), 9509005.

[41] Y. Iwazaki, *Daiichigenri keisan* (Jyouhoukikou, 2012), chap. 3, pp. 211–217.

[42] V. M. Goldschmidt, Naturwissenschafsen **14**, 477 (1926).

[43] M. Ghita, M. Fornari, D. Singh, and S. Halilov, Phys. Rev. B **72**, 054114 (2005).

[44] D. J. Singh, M. Ghita, M. Fornari, and S. V. Halilov, Ferroelectrics **338**, 73 (2006).

[45] K. Singh, S. Acharya, and D. V. Atkare, Ferroelectrics **315**, 91 (2005).

[46] Y. Xie, H.-t. Yu, G.-x. Zhang, and H.-g. Fu, J. Phys. Condens. Matter **20**, 215215 (2008).

[47] L. Feng, L. Jiang, M. Zhu, H. Liu, X. Zhou, and C. Li, J. Phys. Chem. Solids **69**, 967 (2008).

[48] W. Zhong and D. Vanderbilt, Phys. Rev. Lett. **74**, 2587 (1995).

[49] R. E. Cohen, Nature **358**, 136 (1992).

[50] N. Tsuda, K. Nasu, A. Fujimori, and K. Shiratori, *Bussei Kagaku Sensyo, Denki Dendousei Sankabutsu (Electroconductive Oxide)* (Shokabo, 1983).

[51] J. B. Goodenough, Progress in Solid State Chemistry **5**, 145 (1971).

[52] L. Mattheiss, Phys. Rev. **181**, 987 (1969).

[53] R. Meyer, R. Liedtke, and R. Waser, Appl. Phys. Lett. **86**, 112904 (2005).

[54] T. Kolodiazhnyi, Phys. Rev. B **78**, 045107 (2008).

[55] C. Park and D. Chadi, Phys. Rev. B **57**, 961 (1998).

[56] D. I. Woodward, I. M. Reaney, G. Y. Yang, E. C. Dickey, and C. a. Randall, Appl. Phys. Lett. **84**, 4650 (2004).

[57] K. Nishida, H. Kishi, M. Osada, H. Funakubo, M. Nishide, H. Takeuchi, T. Katoda, and T. Yamamoto, Jpn. J. Appl. Phys. **48**, 09KF11 (2009).

[58] K. Härdtl and R. Wernicke, Solid State Commun. **10**, 153 (1972).

[59] B. Jalan, R. Engel-Herbert, T. E. Mates, and S. Stemmer, Appl. Phys. Lett. **93**, 052907 (2008).

[60] D. Muller, N. Nakagawa, and A. Ohtomo, Nature **430**, 657 (2004).

[61] N. Shanthi and D. Sarma, Phys. Rev. B **57**, 2153 (1998).

[62] D. Ricci, G. Bano, G. Pacchioni, and F. Illas, Phys. Rev. B **68**, 1 (2003).

[63] D. Cuong, B. Lee, K. Choi, H.-S. Ahn, S. Han, and J. Lee, Phys. Rev. Lett. **98**, 1 (2007).

[64] M. Choi, F. Oba, and I. Tanaka, Appl. Phys. Lett. **98**, 172901 (2011).

[65] W. Baer, J. Phys. Chem. Solids **28**, 677 (1967).

[66] Z. Hou and K. Terakura, J. Phys. Soc. Jpn. **79**, 1 (2010).

[67] J. Carrasco, F. Illas, N. Lopez, E. Kotomin, Y. Zhukovskii, R. Evarestov, Y. Mastrikov, S. Piskunov, and J. Maier, Phys. Rev. B **73**, 064106 (2006).

[68] a. Janotti, J. B. Varley, P. Rinke, N. Umezawa, G. Kresse, and C. G. Van de Walle, Phys. Rev. B **81**, 085212 (2010).

[69] F. Oba, A. Togo, and I. Tanaka, Phys. Rev. B **77**, 245202 (2008).

[70] M.-H. Du and K. Biswas, Phys. Rev. Lett. **106**, 115502 (2011).

[71] J. Y. Dai, W. P. Chen, G. K. H. Pang, P. F. Lee, H. K. Lam, W. B. Wu, H. L. W. Chan, and C. L. Choy, Appl. Phys. Lett. **82**, 3296 (2003).

[72] H. Takenaka and D. Singh, Phys. Rev. B **75**, 241102 (2007).

[73] A. K. Singh, A. Janotti, M. Scheffler, and C. G. Van de Walle, Phys. Rev. Lett. **101**, 1 (2008).

[74] M.-H. Du and D. Singh, Phys. Rev. B **79**, 205201 (2009).

[75] E. Lavrov, F. Herklotz, and J. Weber, Phys. Rev. Lett. **102**, 185502 (2009).

[76] G. A. Shi, M. Saboktakin, M. Stavola, and S. J. Pearton, Appl. Phys. Lett. **85**, 5601 (2004).

[77] S. Mochizuki, F. Fujishiro, K. Ishiwata, and K. Shibata, Physica B: Condens. Matt. **376-377**, 816 (2006).

[78] T. Kolodiazhnyi, M. Tachibana, H. Kawaji, J. Hwang, and E. Takayama-Muromachi, Phys. Rev. Lett. **104**, 147602 (2010).

[79] J. Hwang, T. Kolodiazhnyi, J. Yang, and M. Couillard, Phys. Rev. B **82**, 214109 (2010).

[80] J. Marucco, M. Ocio, A. Forget, and D. Colson, J. Alloys and Compounds **262-263**, 454 (1997).

[81] V. Fritsch, J. Hemberger, M. Brando, A. Engelmayer, S. Horn, M. Klemm, G. Knebel, F. Lichtenberg, P. Mandal, F. Mayr, M. Nicklas, and A. Loidl, Phys. Rev. B **64**, 045113 (2001).

[82] K. Page, T. Kolodiazhnyi, T. Proffen, A. Cheetham, and R. Seshadri, Phys. Rev. Lett. **101**, 205502 (2008).

[83] O. Diéguez, S. Tinte, A. Antons, C. Bungaro, J. B. Neaton, K. M. Rabe, and D. Vanderbilt, Phys. Rev. B **69**, 212101 (2004).

[84] J. Íñiguez and D. Vanderbilt, Phys. Rev. Lett. **89**, 115503 (2002).

[85] K. J. Choi, M. Biegalski, Y. L. Li, A. Sharan, J. Schubert, R. Uecker, P. Reiche, Y. B. Chen, X. Q. Pan, V. Gopalan, L.-Q. Chen, D. G. Schlom, and C. B. Eom, Science (New York, N.Y.) **306**, 1005 (2004).

[86] J. Junquera and P. Ghosez, Nature **422**, 506 (2003).

[87] V. Petkov, V. Buscaglia, M. T. Buscaglia, Z. Zhao, and Y. Ren, Phys. Rev. B **78**, 054107 (2008).

[88] W. Y. Shih, W.-H. Shih, and I. A. Aksay, Phys. Rev. B **50**, 15575 (1994).

[89] T.-C. Huang, M.-T. Wang, H.-S. Sheu, and W.-F. Hsieh, J. Phys. Condens. Matter **19**, 476212 (2007).

[90] R. Cohen, J. Phys. Chem. Solids **61**, 139 (2000).

[91] *Daiichigenri keisan* (Jyouhoukikou, 2012), chap. 5, pp. 141–148.

[92] Y. Iwazaki, K. Morito, T. Suzuki, H. Kishi, and S. Tsuneyuki, Ferroelectrics **355**, 108 (2007).

[93] Y. Iwazaki, T. Suzuki, and S. Tsuneyuki, J. Appl. Phys. **108**, 083705 (2010).

[94] Y. Iwazaki, Ceramics Japan: Bulletin of the Ceramic Society of Japan **46**, 500 (2011).

[95] Y. Iwazaki, Y. Gohda, and S. Tsuneyuki, APL Materials **2**, 012103 (2014).

[96] Y. Iwazaki, T. Suzuki, Y. Mizuno, and S. Tsuneyuki, Phys. Rev. B **86**, 214103 (2012).

[97] P. Hohenberg and W. Kohn, Phys. Rev. **136**, B864 (1964).

[98] R. M. Martin, *Electronic Structure* (CAMBRIDGE UNIVERSITY PRESS, 2004).

[99] W. Kohn and L. J. Sham, Phys. Rev. **140**, A1133 (1965).

[100] J. Perdew and A. Zunger, Phys. Rev. B **23**, 5048 (1981).

[101] J. P. Perdew, K. Burke, and M. Ernzerhof, Phys. Rev. Lett. **77**, 3865 (1996).

[102] D. Vanderbilt, Phys. Rev. B **41**, 7892 (1990).

[103] G. Kresse, Phys. Rev. B **59**, 1758 (1999).

[104] J. Perdew and M. Levy, Phys. Rev. Lett. **51**, 1884 (1983).

[105] D. Vogel, P. Krüger, and J. Pollmann, Phys. Rev. B **54**, 5495 (1996).

[106] A. Filippetti and N. Spaldin, Phys. Rev. B **67**, 125109 (2003).

[107] C. Pemmaraju, T. Archer, D. Sánchez-Portal, and S. Sanvito, Phys. Rev. B **75**, 045101 (2007).

[108] V. I. Anisimov, J. Zaanen, and O. K. Andersen, Phys. Rev. B **44**, 943 (1991).

[109] A. I. Liechtenstein, V. I. Anisimov, and J. Zaanen, Phys. Rev. B **52**, R5467 (1995).

[110] S. L. Dudarev, S. Y. Savrasov, C. J. Humphreys, and A. P. Sutton, Phys. Rev. B **57**, 1505 (1998).

[111] M. Cococcioni and S. de Gironcoli, Phys. Rev. B **71**, 035105 (2005).

[112] J. P. Perdew, M. Ernzerhof, and K. Burke, J. Chem. Phys. **105**, 9982 (1996).

[113] J. Heyd, G. E. Scuseria, and M. Ernzerhof, J. Chem. Phys. **118**, 8207 (2003).

[114] J. Paier, M. Marsman, K. Hummer, G. Kresse, I. C. Gerber, and J. G. A] gya] , J. Chem. Phys. **125**, 249901 (2006).

[115] S. Lany and A. Zunger, Phys. Rev. B **80**, 085202 (2009).

[116] A. Janotti, D. Segev, and C. Van de Walle, Phys. Rev. B **74**, 045202 (2006).

[117] H. Sawada, Y. Morikawa, K. Terakura, and N. Hamada, Phys. Rev. B **56**, 12154 (1997).

[118] W. Pickett, S. Erwin, and E. Ethridge, Phys. Rev. B **58**, 1201 (1998).

[119] M. Stengel and N. Spaldin, Phys. Rev. B **77**, 155106 (2008).

[120] C. Persson, Y.-J. Zhao, S. Lany, and A. Zunger, Phys. Rev. B **72**, 035211 (2005).

[121] C. G. Van de Walle, J. Appl. Phys. **95**, 3851 (2004).

[122] G.-C. Yi, B. a. Block, and B. W. Wessels, Appl. Phys. Lett. **71**, 327 (1997).

[123] D. Hennings and S. Schreinemacher, J. European Ceram. Soc. **9**, 41 (1992).

[124] M. Karlsson, M. r. Björketun, P. Sundell, A. Matic, G. Wahnström, D. Engberg, L. Börjesson, I. Ahmed, S. Eriksson, and P. Berastegui, Phys. Rev. B **72**, 094303 (2005).

[125] F. Shimojo and K. Hoshino, Solid State Ionics **145**, 421 (2001).

[126] M. C. Tarun and M. D. McCluskey, J. Appl. Phys. **109**, 063706 (2011).

[127] J. T-Thienprasert, I. Fongkaew, D. J. Singh, M.-H. Du, and S. Limpijumnong, Phys. Rev. B **85**, 125205 (2012).

[128] P. Sundell, M. r. Björketun, and G. Wahnström, Phys. Rev. B **76**, 094301 (2007).

[129] M. r. Björketun, P. Sundell, and G. Wahnström, Phys. Rev. B **76**, 054307 (2007).

[130] W. Münch, Solid State Ionics **136-137**, 183 (2000).

[131] M. Cherry, Solid State Ionics **77**, 207 (1995).

[132] F. W. Lytle, J. Appl. Phys. **35**, 2212 (1964).

[133] N. Agmon, Chem. Phys. Lett. **244**, 456 (1995).

[134] K.-d. Kreuer, Chem. Mater. **8**, 610 (1996).

[135] G. Henkelman, B. P. Uberuaga, and H. Jo] sson, J. Chem. Phys. **113**, 9901 (2000).

[136] G. Henkelman and H. Jo] sson, J. Chem. Phys. **113**, 9978 (2000).

[137] N. Govind, M. Petersen, G. Fitzgerald, D. King-Smith, and J. Andzelm, Comput. Mater. Sci. **28**, 250 (2003).

[138] M. D. Segall, P. J. D. Lindan, M. J. Probert, C. J. Pickard, P. J. Hasnip, S. J. Clark, and M. C. Payne, J. Phys. Condens. Matter **14**, 2717 (2002).

[139] K. Kreuer, Solid State Ionics **136-137**, 149 (2000).

[140] S. Baroni, S. de Gironcoli, and A. Dal Corso, Rev. Mod. Phys. **73**, 515 (2001).

[141] X. Gonze, Phys. Rev. B **55**, 10337 (1997).

[142] P. Giannozzi and S. Baroni, J. Chem. Phys. **100**, 8537 (1994).

[143] W. Spitzer, R. Miller, D. Kleinman, and L. Howarth, Phys. Rev. **126**, 1710 (1962).

[144] T. Ishidate, S. Abe, H. Takahashi, and N. Môri, Phys. Rev. Lett. **78**, 2397 (1997).

[145] M. Malinowski, K. ⌈kaszewicz, and S. Å sbrink, J. Appl. Crystallography **19**, 7 (1986).

[146] W. Kohn, A. D. Becke, and R. G. Parr, J. Phys. Chem. **100**, 12974 (1996).

[147] B. r. Hammer, M. Scheffler, K. Jacobsen, and J. Nø rskov, Phys. Rev. Lett. **73**, 1400 (1994).

[148] E. Penev, P. Kratzer, and M. Scheffler, J. Chem. Phys. **110**, 3986 (1999).

[149] Y. Kobayashi, O. J. Hernandez, T. Sakaguchi, T. Yajima, T. Roisnel, Y. Tsujimoto, M. Morita, Y. Noda, Y. Mogami, A. Kitada, M. Ohkura, S. Hosokawa, Z. Li, K. Hayashi, Y. Kusano, J. E. Kim, N. Tsuji, A. Fujiwara, Y. Matsushita, K. Yoshimura, K. Takegoshi, M. Inoue, M. Takano, and H. Kageyama, Nature mater. **11**, 507 (2012).

[150] Y. Iwazaki, T. Sakashita, T. Suzuki, Y. Mizuno, and S. Tsuneyuki, Key Engineering Materials **485**, 19 (2011).

[151] H. Moriwake, Y. Koyama, K. Matsunaga, T. Hirayama, and I. Tanaka, Journal of Physics: Condensed Matter **20**, 345207 (2008).

[152] W. Al-Saidi and A. Rappe, Phys. Rev. B (2010).

[153] A. Filippetti and N. Hill, Phys. Rev. B **65**, 195120 (2002).

[154] L. Boyer, M. Mehl, J. Flocken, and J. Hardy, Jpn. J. Appl. Phys. **24**, 204 (1985).